TESIS DE DOCTORADO

STUDY AND CONTROL OF THERMAL TRANSPORT IN COMPLEX FLUIDS

Carlos López Bueno

ESCUELA DE DOCTORADO INTERNACIONAL DE LA UNIVERSIDAD DE SANTIAGO DE COMPOSTELA

PROGRAMA DE DOCTORADO EN CIENCIA DE MATERIALES

SANTIAGO DE COMPOSTELA

AÑO 2021

USC
UNIVERSIDADE
DE SANTIAGO
DE COMPOSTELA

DECLARACIÓN DEL AUTOR/A DE LA TESIS

D./Dña. **Carlos López Bueno**

Título de la tesis: **Study and Control of Thermal Transport in Complex Fluids**

Presento mi tesis, siguiendo el procedimiento adecuado al Reglamento y declaro que:

1) La tesis abarca los resultados de la elaboración de mi trabajo.
2) De ser el caso, en la tesis se hace referencia a las colaboraciones que tuvo este trabajo.
3) Confirmo que la tesis no incurre en ningún tipo de plagio de otros autores ni de trabajos presentados por mí para la obtención de otros títulos.
4) La tesis es la versión definitiva presentada para su defensa y coincide la versión impresa con la presentada en formato electrónico.

Y me comprometo a presentar el Compromiso Documental de Supervisión en el caso que el original no esté depositado en la Escuela.

En **Santiago de Compostela**, **26 de julio de 2021**.

Firma electrónica

USC
UNIVERSIDADE
DE SANTIAGO
DE COMPOSTELA

AUTORIZACIÓN DEL DIRECTOR / TUTOR DE LA TESIS

Study and Control of Thermal Transport in Complex Fluids

D. José Francisco Rivadulla Fernández

INFORMA/N:

Que la presente tesis, se corresponde con el trabajo realizado por D. Carlos López Bueno, bajo mi dirección/tutorización, y autorizo su presentación, considerando que reúne los requisitos exigidos en el Reglamento de Estudios de Doctorado de la USC, y que como director de esta no incurre en las causas de abstención establecidas en la Ley 40/2015.

De acuerdo con lo indicado en el Reglamento de Estudios de Doctorado, declara también que la presente tesis doctoral es idónea para ser defendida en base a la modalidad de Monográfica con reproducción de publicaciones en los que la participación del doctorando/a fue decisiva para su elaboración y las publicaciones se ajustan al Plan de Investigación.

En Santiago de Compostela, 26 de Julio de 2021

USC
UNIVERSIDADE
DE SANTIAGO
DE COMPOSTELA

Acknowledgements

Coa presentación desta tese remata un dos períodos máis apaixonantes a nivel persoal e profesional da miña vida. A persoa que son hoxe en día é totalmente diferente a aquela que comezou esta andadura fará uns catro anos. Atrás quedaron aquelas tardes nas que chegaba desesperado porque algo non me saía á primeira, dando lugar a unha persoa cunha paciencia que, aínda que pouca, nunca imaxinei que puidese acadar. Hoxe son unha persoa moito máis reflexiva e crítica do que era no pasado e iso é debido, en gran parte, a esta tese. Esta transformación non sería posible sen dúas persoas, sen dúbida as máis importantes deste proceso.

En primeiro lugar, ao meu director de tese Fran, que apostou por min dende un primeiro momento, a pesar de ser un físico medio tolo que apareceu un día polo seu despacho. A túa actitude, escoitando e valorando en todo momento as nosas opinións, e a túa preocupación porque non só obtivésemos resultados, senón que aprendésemos, son dous dos aspectos que máis me impresionaron dende o primeiro día. Espero ter sido merecedor de toda esa confianza e lograr cumprir, cando menos, algunha das expectativas que depositaches en min. Desta etapa levo un amigo máis que un xefe, espero que sexa recíproco.

En segundo lugar, e non por iso menos importante, quero agradecer á miña admirada Vero. Tal é a túa influencia nesta tese que considero que deberías ser considerada coautora ou codirectora da mesma, unha mágoa que non sexa posible. Non é sinxelo atopar palabras que describan todo o que fixeches por min nestes anos, o máis laborioso sen dúbida, aturarme. A túa paixón polo traballo ben feito, a túa paciencia

e a túa comprensión resultaron fundamentais para todos os éxitos que acadei nestes anos.

Tamén quero agradecer a todos aqueles compañeiros de laboratorio destes anos, en particular a Alex, Lucía, David, Eric, Elías, Rafa e Víctor, de todos vós aprendín moito. Gustaríame facer mención especial aos máis novatos Noa e Manu, a vosa motivación lembroume o bonita que é a ciencia. Agardo tervos servido de axuda nos vosos inicios. Gustaríame destacar tamén o papel do profesor Alfredo Amigo, que me axudou en numerosas ocasións no meu traballo. As discusións contigo foron realmente interesantes.

I would also like to thank Prof. Sander Woutersen, who was the responsible of my research stay in Amsterdam. Your interest in my work and your patience are admirable. I also want to extend this acknowledgment to Marius, who helped me in everything, both inside and outside the lab.

Por outra parte, gustaríame agradecer a todos aqueles organismos que me apoiaron económicamente durante esta etapa, en particular á Xunta de Galicia, por apoiarme no marco do seu programa de axudas predoutorais, e ao Ministerio de Ciencia, Innovación e Universidades de España, por financiar as miñas investigacións.

A todos aqueles familiares e amigos que me apoiastes dende pequeno e, por que non dicilo, me convidastes a festas e verbenas. A meu irmán e a meu pai por ensinarme a axudar sempre aos demais. A Dani por, entre outras moitas cousas, asegurar que me mantivese nunha boa forma física. Aos meus novos pais Suso e Merchi por ensinarme tantas cousas nestes anos. Aos máis pequenos Marta e Lucas por amosarme o voso interese e curiosidade pola vida. Aos meus amigos de sempre Curros e Fran; e aos máis recentes, Jan, Irene, Manu e Eva, por estar sempre que o precisei. A todos vós, gracias.

Seguramente me esqueza de moita xente nestas liñas, pero que ninguén pense que esquezo a miña nai. Para ti quero reservar estas últimas liñas, para agradecerche todo o que fixeches por min dende que nacín, por transmitirme todos os valores que hoxe culminan nesta tese, por ensinarme todo o que sei, por todo isto e máis, gracias. Pola túa importancia na miña vida, quero dedicarche esta tese.

Aim of the Thesis

The understanding of the dynamic structure of liquids is fundamental, as they are the basis for the vast majority of chemical reactions, many fundamental for life. However, the large complexity of these systems has frustrated the development of a theoretical framework, impeding the understanding of a wide variety of phenomenology. For example, the large anomalies present in liquid water are far to be understood, even it is present daily in our life.

Despite the computational power is increasing rapidly, allowing the *ab initio* calculations of very complex materials and predicting the appearance of interesting novel properties, the research in the fundamentals of liquids progresses slowly. The formation of large supramolecular structures induced by the strong intermolecular interactions are usually short-lived, as the continuous movement of the molecules destroys this ordering. Consequently, the dynamic structure of liquids can only be accessed through high resolution time-resolved techniques, or with complex computational calculations, which are highly time-consuming.

In this regard, the study of heat transport in liquids is underexploited, in spite of the large sensitivity to molecular order demonstrated in the solid state. In liquids, the energy is transmitted through vibrational coupling between the molecules, which is a very fast mechanism and allow, in principle, the characterization of the short-lived structures present in liquids.

The main aim of this thesis is the use of the heat transport to probe the molecular dynamics of liquids. Our general objective is to analyze if the measurement of the thermal conductivity in liquids is sensitive to

changes in the molecular arrangement. This novel approach to the study of liquids has never be explored, to the best of our knowledge. To do that, we perform a systematic analysis of the heat transport, comparing the results with spectroscopic and other thermodynamic properties, as well as to the vast research of the literature. This thesis can be divided in two separated projects.

First, the large number of anomalous properties of water has attracted our attention. The presence of strong H-bonds leads to the formation of a long-range tetrahedral structure, similar than ice. The introduction of different solutes affects this cooperative network, leading to unexpected results. The understanding of the effect of dissolving different solutes in water is particularly interesting, as the living media (cells) are very crowded systems, where a large number of both organic and inorganic molecules are present. Thus, the study of the energy transfer in these systems may give important information about several biological processes, like molecular recognition.

On the other hand, it is known that thermal conductivity is highly sensitive to changes on the molecular ordering. Consequently, it is expected a large difference of this magnitude across liquid-to-solid phase transitions. In this thesis we will analyze the different kinds of phase transitions in different Ionic Liquids. The possibility of tuning the intermolecular interaction at will opens a new avenue for the understanding of ionic solids, which may have important technological applications in the design of new materials.

Moreover, the possibility of switching between high and low thermal conductivity states has attracted the interest of several research groups. The control of heat transport allows their use as thermal regulators, with important applications like energy storage. The use of liquid-to-solid phase transitions is one of the most promising strategies, as large switching ratios can be achieved. In this regard, we propose the use of Ionic Liquids, as they are versatile materials whose operation temperatures can be selected for each particular application.

The external control of these systems, by applying an electric current or light, supposes an important improvement of these devices. In

this field, azobenzene based compounds are very promising, as they can be liquefied by the illumination with an external UV field.

We expect that the discussions presented in the following chapters help to shed light into the complex phenomenology of liquids. Finally, we hope that the work presented in this thesis stimulates the use of heat transport as a tool for the study of the molecular dynamics, from both experimental and theoretical points of view.

USC
UNIVERSIDADE
DE SANTIAGO
DE COMPOSTELA

Contents

USC
UNIVERSIDADE
DE SANTIAGO
DE COMPOSTELA

1. Introduction

The study of the physical properties of liquids has attracted the interest of some of the most important scientists of the last centuries, like Faraday [1], the Nobel laureate L. Landau [2] or J. Ziman [3]. However, a general theory for the transport properties of liquids has not been developed yet, despite liquids are fundamental for life. The complexity of this challenge resides in the absence of a small parameter (i.e. the interaction strength in gases or the displacement from the equilibrium position in solids), which forbids treating the interatomic interaction potential as a series expansion of this parameter, as well as the lack of long range translational symmetry. Liquids have interactions sufficiently strong to can not be considered as non-interacting systems (gases), and large structural fluctuations, impeding the treatment with a reduced number of molecules. Consequently, thermodynamic properties of liquids remained absent of the statistical physics textbooks [4–7].

In this thesis, we propose the study of heat transport in liquids as a novel approach to the study of the dynamic structure of liquids. We focus our attention on the thermal conductivity, which is highly sensitive to changes in the dynamic nature of the whole system, as we will demonstrate in the following sections. It is worth noting that this is the unique transport coefficient which can be studied continuously for the different states of matter (liquid, solid and gaseous) across their phase transitions.

Importantly, the majority of most relevant chemical reactions, either from a technological point of view, or from a life perspective, occur in the liquid (water) state, and involve a transfer of energy between the

molecules across the solvent, or with the solvent. Thus, heat diffusivity of these systems is a fundamental parameter to determine the velocity and the products of a certain chemical reaction [8]. On the other hand, beyond the chemical reaction perspective, the control of thermal conductivity in liquids may have important technological applications in the field of energy storage and thermal regulation, or biomedical hyperthermia devices [9–14].

Previous to the discussion of the thermal conductivity in the different liquid environments studied in this thesis, I will review, briefly, the mechanism of heat transport in liquids, putting special attention to its relation with the microscopic molecular environment.

1.1 Mechanisms of heat transfer

Heat can be transported in liquids, mainly, by two different mechanisms: conduction and convection. Radiation is a mechanism of energy transfer between two different systems, and can not be defined in a single material. Thus, it will not be treated in this discussion.

In solids, atoms vibrate around their equilibrium positions, and the heat is propagated through the whole system by collective vibrational modes of a wide frequency range, the so-called phonons [15]. This mechanism is also present in liquids, although the rapid movement of molecules restricts the vibrational modes, that propagate only to the very high frequency ones [4–7, 15–17].

However, liquid and gas molecules flow, and undergo large displacements which introduce another possibility of heat transport: convection (see Figure 1.1). Increasing the temperature of part of the system decreases its density, excluding some special cases, like water at certain temperatures. This leads to a density gradient across the system, which drives the hot molecules to the upper part of the system [18].

To determine the relative contribution of each mechanism to the heat transport we can use the Rayleigh number (Ra). This is a dimensionless magnitude expressing the ratio between convective and thermal diffusion rates [18]:

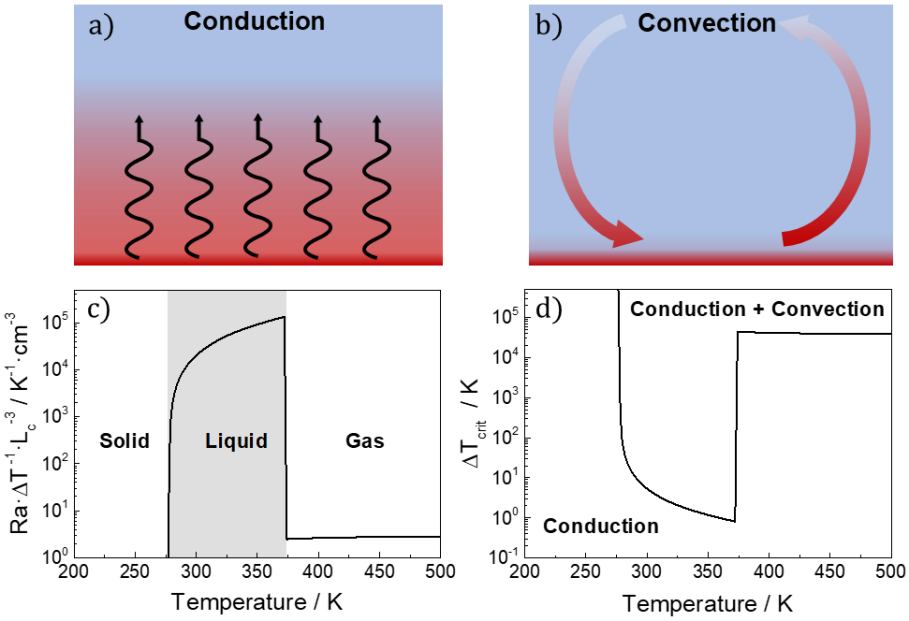

Figure 1.1: Sketch of the two mechanisms of heat transfer present in liquids (a-b), and relative importance of each mechanism (c). The value of $\mathrm{Ra}\cdot\Delta\mathrm{T}^{-1}\cdot\mathrm{L_c}^{-3}$ was estimated using the data of water reported in ref. [18]. d) Threshold temperature for the transition between a system dominated by conduction and the presence of a significant convection flow. Note that $\Delta\mathrm{T_{crit}}$ depends on the geometry of the system ($\Delta\mathrm{T_{crit}} \propto \mathrm{L_c}^{-3}$). As an example, we have assumed a horizontal square hot plate of side 1 cm ($\mathrm{L_c} = 0.25$ cm).

$$\mathrm{Ra} = \frac{\rho\cdot\mathrm{g}\cdot\beta\cdot\Delta\mathrm{T}\cdot\mathrm{L_c}^3}{\eta\cdot\alpha} \tag{1.1}$$

where ρ is the density, g the acceleration of gravity, β the thermal expansion coefficient, η the viscosity, α the thermal diffusivity, $\Delta\mathrm{T}$ the temperature difference and $\mathrm{L_c}$ is a characteristic length, which depends on the geometry. If Ra is larger than a certain value, which depends on the dimensions and shape of the system, natural convection begins to contribute to heat transfer.

In Figure 1.1.c) we show an estimation of the relative contribution of convention/conduction to heat transport in pure water, normalized by ΔT and $\mathrm{L_c}$. The plot shows the importance of convection in liquids, in comparison with solids and gases; moreover, assuming a certain geometry we can estimate the threshold temperature difference [18], which defines the limit of pure conduction heat transfer:

$$\Delta \mathrm{T_{crit}} = \frac{1708 \cdot \eta \cdot \alpha}{\rho \cdot \mathrm{g} \cdot \beta \cdot \mathrm{L_c^3}} \tag{1.2}$$

In Figure 1.1.d we plot an estimation for $\Delta \mathrm{T_{crit}}$ at different temperatures (and phases). While only a difference of 5 K induces a convective flow in liquid water at 300 K, more than 10000 K are necessary in water vapor, in this geometry. This demonstrates the importance of both mechanisms in liquids, particularly for big systems, as ΔT_{crit} decreases by increasing L_c.

However, it is worth noting that heat conduction depends strongly on the molecular arrangement, as well as on the type and strength of the interactions. For instance, crystalline solids transport energy much faster than amorphous solids, or liquids. This dependence is not such large in convection heat flow, which is dominated by the geometry of the whole system. Thus, the analysis of heat conduction provides a promising connection between macroscopic and microscopic worlds.

1.2 Conductive heat transport

The presence of a temperature gradient ($\vec{\nabla} T$) generates a flux of heat ($\vec{J_Q}$) in the opposite direction, which is proportional to $\vec{\nabla} T$, according to the Fourier law:

$$\vec{J_Q} = \frac{dQ}{A \cdot dt} \hat{J}_Q = -\kappa \cdot \vec{\nabla} T \tag{1.3}$$

where the proportional factor κ is the thermal conductivity, which determines the rate of energy transfer.

In order to determine the functional form of κ, lets imagine two identical systems but with a small temperature difference (internal energy). The connection of both systems through a permeable wall (see Figure 1.2), leads to a net transfer of energy; for small thermal gradients the net mass transfer can be neglected so that the concentration remains constant across the system.

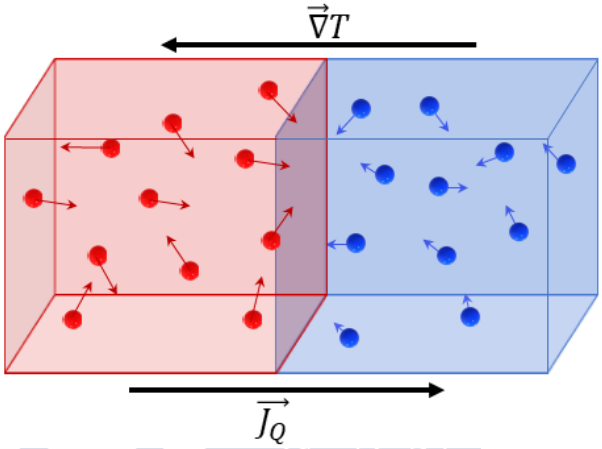

Figure 1.2: Sketch of the heat diffusion process. High temperatures (red) are associated to higher internal energies, so the interchange of one molecule from the left to one from the right leads to a net energy flux, without net mass transfer.

After a certain period of time dt, where each particle travels a distance dx perpendicular to the wall, the number of particles that passes through a section of area A depends on their average velocity $< v_x >$, and on the particle density (N/V). Thus, the energy flux in both directions can be expressed as [19]:

$$\vec{J}_Q(\text{hot} \rightarrow \text{cold}) = \frac{N}{V} < v_x > \varepsilon_{hot}\, \hat{x} = \frac{1}{V} < v_x > E_{hot}\, \hat{x} \qquad (1.4a)$$

$$\vec{J}_Q(\text{hot} \leftarrow \text{cold}) = -\frac{N}{V} < v_x > \varepsilon_{cold}\, \hat{x} = -\frac{1}{V} < v_x > E_{cold}\, \hat{x} \qquad (1.4b)$$

where ε is the energy of each particle and E the total energy ($E = N\varepsilon$).

As we restricted our analysis to the case where the energy (temperature) difference between both systems is not too large, we can perform an expansion around the mean energy (E_0):

$$E_{hot} = E_0 + \frac{dE}{dx}dx \tag{1.5a}$$

$$E_{cold} = E_0 + \frac{dE}{dx}(-dx) \tag{1.5b}$$

Thus, the net energy flux can be expressed as follows:

$$\begin{aligned}\vec{J}_Q = \vec{J}_Q(\text{h} \rightarrow \text{c}) + \vec{J}_Q(\text{h} \leftarrow \text{c}) = 2 < v_x > \frac{1}{V}\frac{dE}{dx}dx\ \hat{x} = \\ = -\frac{1}{2} < v > \frac{1}{V}\frac{dE}{dT}dx\vec{\nabla}T\end{aligned} \tag{1.6}$$

where we use that the average speed of the molecules $< v >$ is four times the one-dimensional speed [19, 20].

In this derivation, we did not consider collisions between the different particles. Thus, we can approximate dx as the mean distance, perpendicular to the wall, traveled by the particles between collisions $< x^2 >^{1/2}$, which is related to the three dimensional mean free path Λ $\left(< x^2 >^{1/2} = \frac{2}{3}\Lambda\right)$. Taking into account that $C_v = V^{-1}(dE/dT)$ is the isochoric heat capacity per unit volume, equation 1.6 can be rewritten as:

$$\vec{J}_Q = -\frac{1}{3} < v > C_v\Lambda\vec{\nabla}T \tag{1.7}$$

By comparison with equation 1.2, we obtain an expression for the thermal conductivity:

$$\kappa = \frac{1}{3}C_v < v > \Lambda \tag{1.8}$$

This derivation is valid for all kind of systems, not only fluids. Thus, the measurement of the thermal conductivity gives, at the same

time, information about the energy of the heat carrying particles C (molecules, electrons or phonons), their velocity and the distance traveled between two scattering events.

In ideal gases, molecules are moving at a certain velocity, independently of each other. This defines their internal energy and, consequently, their temperature. Thus, the transmission of energy is produced through momentum transfer in collisions between pairs of molecules, changing their respective velocities in a similar way than billiard balls [21].

This mechanism for energy transfer is not available in the solid state, as the atoms of the system are placed in fixed positions. However, the interatomic interactions are large, and there exist collective vibrational states of all atoms of the solid (equivalent to the normal vibrational modes of a molecule) which are transmitted through the whole system. In analogy with photons and their wave-particle duality, these lattice waves can be viewed as particles (phonons), whose energy is $E = \hbar\omega$.

These collective vibrations represent the lowest energy vibrational excitations of the solid, much lower in energy than individual uncorrelated movement of each atom, and therefore phonons are responsible of the large thermal conductivity of solids (see Figure 1.3). Note that the mobility of electrons in metallic systems introduces an additional mechanism of energy transfer, increasing further the thermal conductivity.

In liquids, the transmission of energy occurs through collisions and, at the same time, through vibrational intermolecular coupling, as in solids. Although the concept of phonons is strictly not applicable to liquids, as the dynamic structure of liquids varies in the same time scale, heat is transferred in a similar way, by changing the atomic connectivity through local configurational excitations (LCE), as suggested by Egami et al. [22–24]. These modes are propagated through intermolecular coupling, which is the most relevant source of heat transfer. However, the lack of long range order impedes the transmission of the vibrational modes across long distances, reducing κ with respect to solids [15], although it is larger than for gases (see Figure 1.3).

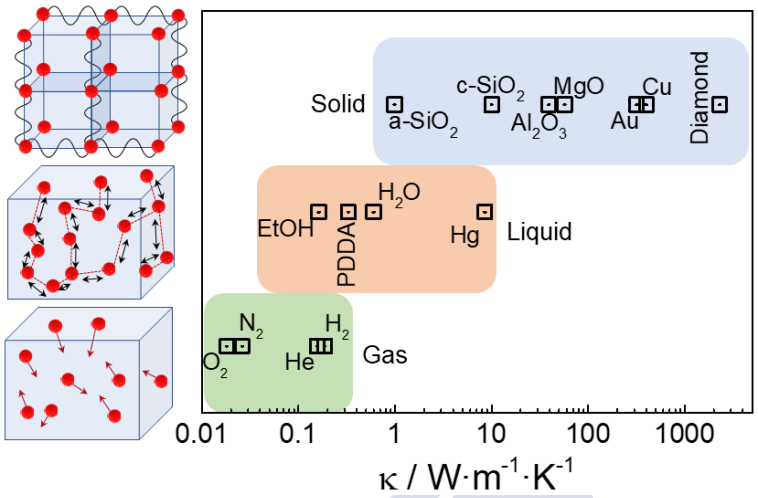

Figure 1.3: Thermal conductivity of different materials at room temperature. Data reproduced from references [18,25–29]. a-SiO_2 and c-SiO_2 refer to amorphous and crystalline quartz, respectively. The pictures at the left represent the mechanism of heat transfer in each system: molecular collisions in gases, vibrational coupling in liquids and lattice waves in crystalline solids.

In order to get a clearer insight on how heat is transferred across liquids, we can compare the characteristic times for molecular and heat diffusion. For instance, the velocity of the molecules within the liquid can be related to the self-diffusion coefficient D, through the Einstein-Smoluchowski equation:

$$\tau = \frac{d^2}{6D} \tag{1.9}$$

where τ is the time required to travel an average distance d.

On the other hand, the velocity of propagation of the LCE can be obtained from the speed of sound ($v_s = d/t_{LCE}$). Thus, an approximate relationship between both characteristic times can be calculated:

$$\frac{\tau}{t_{LCE}} = \frac{v_s}{6D} d \tag{1.10}$$

which increases with d. Considering that in liquids $v_s \sim 10^3$ m·s^{-1} and $D \sim 10^{-9}$ m^2·s^{-1}, we obtain that both times are comparable only at distances smaller than $\sim 10^{-12}$ m. For instance, $\tau \sim 50 \cdot t_{LCE}$ for one intermolecular distance (~ 3 Å), showing that molecular vibrational coupling is the major contribution to heat propagation. This result is in accordance with the larger thermal diffusivity of liquids ($\alpha \sim 10^{-7}$ m^2·s^{-1}) compared with the molecular diffusivity ($D \sim 10^{-9}$ m^2·s^{-1}).

This simple analysis shows that the thermal conduction in liquids can be treated in a similar theoretical framework than solids. In the following, we perform a detailed derivation of the heat capacity, using a similar strategy than K. Trachenko and D. Bolmatov [4–7, 17], and considering the restrictions suggested by Frenkel [30].

1.2.1 Heat capacity

In the derivation of equation 1.2, we have assumed that the heat is carried by particles with different energies. This derivation is valid for all type of heat transfer excitations, as we can use the wave-particle duality. The temperature dependence of the energy of each particle is the heat capacity:

$$c = \frac{d\varepsilon}{dT} = \frac{1}{N}\frac{dE}{dT} \tag{1.11}$$

The energy contribution of each particle to the total energy of the system E depends on its frequency and on the density of states, which is given by the Bose-Einstein distribution [2, 15]:

$$E = \sum_{i,p} \frac{\hbar\omega_i}{\exp\left(\frac{\hbar\omega_i}{k_B T}\right) - 1} \tag{1.12}$$

where p denotes the three vibrational modes, one longitudinal and two transversal. Thus, the heat capacity of the system can be calculated as follows:

$$C = \sum_{i,p} \frac{\hbar^2 \omega_i^2}{k_B T^2} \frac{\exp\left(\frac{\hbar\omega_i}{k_B T}\right)}{\left[\exp\left(\frac{\hbar\omega_i}{k_B T}\right) - 1\right]^2} \tag{1.13}$$

The sum can be replaced by an integral, by introducing the Debye density of states $g(\omega) = 3N\omega^2\omega_D^{-3}$, where ω_D is the Debye frequency, which determines the maximum frequency of the system:

$$C = \sum_{p} \int_0^{\omega_D} \frac{3N\omega^2}{\omega_D^3} \frac{\hbar^2\omega^2}{k_B T^2} \frac{\exp\left(\frac{\hbar\omega}{k_B T}\right)}{\left[\exp\left(\frac{\hbar\omega}{k_B T}\right) - 1\right]^2} d\omega \tag{1.14}$$

which can be rewritten as a function of the Debye temperature, defined as $\Theta_D = \hbar\omega_D/k_B$:

$$C = \sum_{p} 3Nk_B \left(\frac{T}{\Theta_D}\right)^3 \underbrace{\int_0^{\Theta_D/T} \frac{x^4 e^x}{\left(e^x - 1\right)^2} dx}_{I(0,\Theta_D/T)} \tag{1.15}$$

where $x = \hbar\omega/k_B T$ and $I(a,b)$ is the integral evaluated between a and b.

In solids, there is not any difference between the energy of longitudinal and transversal modes. In liquids, the lack of translational symmetry is considered to forbid the propagation of transverse waves. However, Frenkel demonstrated that liquids can support transverse waves with periods shorter than $\tau_F = 2\pi/\omega_F$, the average lifetime of the molecules between two diffusive steps [7, 30]. Thus, the lower limit of the integral for the two transversal modes is $\Theta_F/T = \hbar\omega_F/k_B T$:

$$\begin{aligned} C_t &= 3Nk_B \left(\frac{T}{\Theta_D}\right)^3 \int_{\Theta_F/T}^{\Theta_D/T} \frac{x^4 e^x}{\left(e^x - 1\right)^2} dx = \\ &= 3Nk_B \left(\frac{T}{\Theta_D}\right)^3 \left[I\left(0, \frac{\Theta_D}{T}\right) - I\left(0, \frac{\Theta_F}{T}\right)\right] \end{aligned} \tag{1.16}$$

In this approximation, the heat capacity associated to the heat carrying excitations (LCE) ($C = C_l + 2C_t$) is:

$$C_{LCE} = 3Nk_B \left(\frac{T}{\Theta_D}\right)^3 \left[3I\left(0, \frac{\Theta_D}{T}\right) - 2I\left(0, \frac{\Theta_F}{T}\right)\right] \tag{1.17}$$

This equation represents a solid-like approximation to the heat capacity of liquids, as rotational and translational modes are not considered. The contribution of these modes to C depends on the temperature and on the intermolecular interactions, which increases with temperature and decreases with the strength of intermolecular forces.

In order to determine the vibrational heat capacity, it is necessary to calculate both Θ_D and Θ_F. The first one can be calculated from its relation with the sound velocity [26, 31]:

$$\Theta_D = \frac{h v_s}{k_B} \left(\frac{4\pi}{3n} V_{mol}\right)^{-1/3} \tag{1.18}$$

where $V_{mol} = M \cdot N_{Av}^{-1} \cdot \rho^{-1}$ is the average volume occupied by each molecule and n its number of atoms.

On the other hand, the Θ_F can be calculated using the Einstein-Smoluchowski equation:

$$\Theta_F = \frac{h\nu_F}{k_B} = \frac{h}{k_B \tau_F} = \frac{h}{k_B} \frac{6D}{r^2} \underbrace{=}_{r^3 = \frac{3}{4\pi} V_{mol}} \frac{6Dh}{k_B} \left(\frac{3}{4\pi} V_{mol}\right)^{-2/3} \tag{1.19}$$

In Figure 1.4, we plot the integrand of I, multiplied by the previous factors, which represents the contribution of each vibrational mode to the total heat capacity. As expected, the spectral heat capacity increases with the frequency of the vibration, as these excitations carry higher energies. As an example, we have calculated the heat capacity of water, obtaining a value of $\sim 3R$ per mol. This is in agreement with an harmonic oscillator model, as kinetic and potential energies contribute $(3/2)RT$ to the total energy of the system.

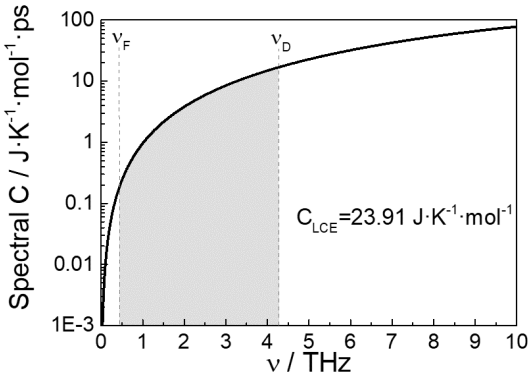

Figure 1.4: Spectral heat capacity of water at T=300 K. The vibrational heat capacity results from the integration between ν_F and ν_D for the two transversal modes, and from 0 to ν_D for the longitudinal mode.

This result also shows that the suppression of low frequency modes does not result in a large reduction of C, as these vibrational modes do not contribute much to the total heat capacity. Therefore, the energy of heat carrying excitations is mostly determined by the Debye temperature.

1.3 Thermal conductivity and microscopic environment

As we discussed previously, the major mechanism of energy transfer in liquids is the anharmonic coupling of molecular vibrations, at a speed equal to the sound velocity. However, the large disordering of liquids hinders the propagation of these vibrations across long distances and, consequently, Λ will be reduced to only a few intermolecular distances (δ). Thus, Λ does not depend on the frequency of the vibrations, similar to glasses [15], and equation 1.2 can be rewritten as:

$$\kappa_{liq} = \frac{1}{3} \cdot v_s \cdot (a \cdot \delta) \cdot C_v \tag{1.20}$$

where a is the proportionality constant between Λ and δ ($\Lambda = a\delta$). Importantly, a must depend on the degree of connectivity between neighboring molecules; so the measurement of κ should provide important information about the supramolecular arrangement.

In Table 1.1 we show the values of Λ calculated using this equation, expressed as a function of the intermolecular distance. For acetone, this value is $\Lambda \approx 1.12\delta$, which is in accordance with the low κ of molecular liquids. However, the presence of strong H-bonds in ethanol and water leads to an underestimation of Λ, as it is known that the presence of H-bonds leads to the formation of locally-ordered structures.

Name	C_v (tot.) $\mathrm{J\cdot mol^{-1}\cdot K^{-1}}$	Λ	C_v (LCE) $\mathrm{J\cdot mol^{-1}\cdot K^{-1}}$	Λ
Water	74.8	1.53δ	23.91	4.9δ
Ethanol	112.2	0.85δ	24.6	3.4δ
Acetone	90	1.12δ	24.6	4.1δ

Table 1.1: Values of Λ calculated from the total heat capacity and only the vibrational component.

Strong H-bonds and short range ordering lead to an unusual fast transmission of the intermolecular vibrations, one order of magnitude faster than in van der Waals molecular liquids [32,33]. Thus, in the time scale of energy transmission in H-bonded liquids, the rotation of the molecules are negligible and, consequently, it should not be introduced in equation 1.20. Therefore, these systems can be treated as solids at these time scales, and consequently, only the vibrational heat capacity should be taken into account.

Considering this hypothesis results in a value of $\Lambda = 4.9\delta$ for water, in perfect agreement with an average coordination number of 4.7 obtained from molecular dynamics simulations [34]. Therefore, we think that the validity of the solid-like approximation at the time scales relevant for heat transfer depends on the ratio between rotational and vibrational times.

An analysis of equation 1.20 may lead to the counterintuitive result that the thermal conductivity increases with the intermolecular distance. However, we should introduce the molar heat capacity C instead of C_v, as the number of heat carrying excitations depends on the amount of molecules. The ratio between both magnitudes can be expressed as a function of the intermolecular distance, as follows:

$$C_v = \frac{C}{V_m} = C\left[N_{av}\cdot\frac{4}{3}\pi\left(\frac{\delta}{2}\right)^3\right]^{-1} = \frac{6\cdot C}{N_{av}\pi\delta^3} \tag{1.21}$$

Introducing this relation into equation 1.20 leads to the following expression:

$$\kappa = \frac{2}{N_{av}\pi}v_s C\left(\frac{a}{\delta^2}\right) \tag{1.22}$$

which shows that the thermal conductivity decreases with the squared intermolecular distance.

Similarly, the sound velocity can be also related to microscopic properties of the liquid, in this case through the adiabatic compressibility K, which is a probe of the strength of the intermolecular interactions:

$$v_s = \left(\frac{1}{\rho K}\right)^{1/2} \underbrace{=}_{\rho = M\cdot V_m^{-1}} \left(\frac{N_{av}\pi}{6M}\frac{\delta^3}{K}\right)^{1/2} \tag{1.23}$$

So, from this equation, the thermal conductivity can be expressed as:

$$\kappa = \left(\frac{2}{3\pi N_{av}M}\right)^{1/2}\frac{C\cdot a}{K^{1/2}\cdot\delta^{1/2}} \tag{1.24}$$

Assuming a simple harmonic oscillator model for intermolecular interactions, the compressibility is proportional to the inverse of the spring constant k. Therefore, the thermal conductivity is sensitive, at the same time, to changes of intermolecular distances and to variations of the type and strength of the intermolecular bonds (see Figure 1.5).

This analysis shows that the thermal conductivity may be an important tool to study the microscopic arrangement of liquids and, particularly, how the disposition of molecules change in response to the

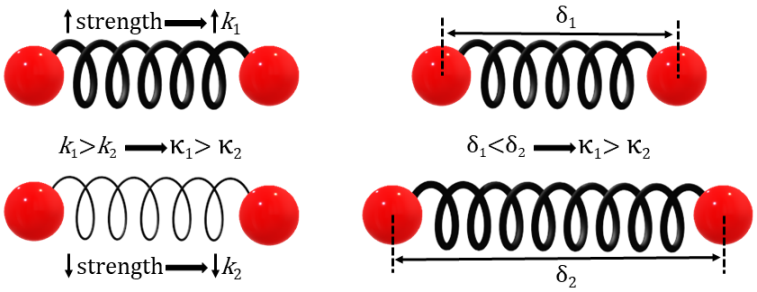

Figure 1.5: Scheme of the dependence of the thermal conductivity κ with the bond strength k and with the intermolecular distance δ.

presence of a solute. This opens a new strategy for the characterization of transient structures in liquids, and may be an ideal (and much more affordable) complement to high-resolution femtosecond IR spectroscopy [32, 33], neutron scattering [35] or high-resolution inelastic X-ray scattering [36]. Moreover, thermal conductivity is a bulk transport property, offering important information about the intermolecular arrangement beyond the first coordination shell of a molecule.

In this thesis we will use the high sensitivity of thermal conductivity to study the formation of supramolecular structures in liquids. Moreover, taking advantage from the fact that thermal conductivity is the only transport property which can be studied continuously across a liquid-to-solid phase transition, we will study the mechanism of formation of an ionic solid from its melt.

USC
UNIVERSIDADE
DE SANTIAGO
DE COMPOSTELA

2. The 3ω Method

The main experimental technique (methodology) used in this thesis is a variation of the 3ω method, for the measurement of the thermal conductivity of liquids. The method was originally developed by D.G. Cahill, for the study of solids and thin films [37, 38]. Due to its importance in this project, I will describe it in detail in this chapter.

There are several methods for measuring the thermal conductivity of solids and liquids, which can be broadly classified in two groups depending on the physical principle used: optical and electrical methods.

Optical methods (in the time or frequency domain) use the temperature dependent reflectance of the material. In these methods, a modulated laser heats the sample surface (pump) and another laser measures the resultant thermal wave (probe) [39–42]. They allow a rapid and accurate measurement of the thermal conductivity, even in electrically conducting samples. The drawback of these methods is that their implementation is complex and expensive, particularly for the case of time-domain thermoreflectance.

On the other hand, electrical methods, like the 3ω method, are more affordable and easier to use, although their application is limited to electrically insulating materials. These methods use a metallic strip, that serves as heater and sensor.

In this thesis we developed a variation of the 3ω method for measuring the thermal conductivity of liquids, optimized for measuring small volumes ($\sim$600 nL). This represents an important advantage over other methods, like the Hot-wire or transient Hot-wire methods, where sam-

ple volumes of the order of mL are normally needed [43]. The following sections include a detailed explanation of the 3ω method.

2.1 The 3ω Voltage

The 3ω method, developed by Cahill [37], uses the self-heating produced when an AC current is applied through a metallic line deposited on the top surface of a sample (Fig. 2.1). In this method, we measure the voltage drop at three times the input frequency ($V_{3\omega}$), which occurs as a consequence of the self-heating. This 3ω voltage is related to the temperature oscillations produced by the Joule effect, and depends on the thermal diffusivity of the environment. The mathematical relation between these magnitudes can be found in references [28, 37, 44].

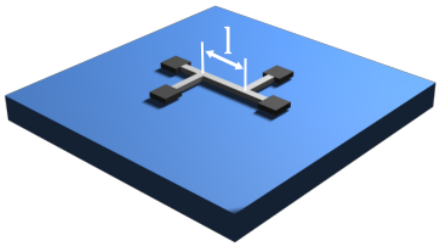

Figure 2.1: Scheme of the experimental setup used in 3ω measurements. We used a metallic Pt or Au line, as they both present a large temperature dependence of the electrical resistance, which increases the sensitivity of the method. The length 'l' represents the distance between the contacts.

An AC current ($I = I_0 \sin(\omega t)$) flowing through the heater deposited on top of the sample, like in Figure 2.1, dissipates a heat (Q):

$$Q = I_0^2 \sin^2(\omega t) R = \frac{I_0^2 R}{2} \left[1 - \cos(2\omega t)\right] = P \left[1 - \cos(2\omega t)\right] \quad (2.1)$$

The energy released produces a temperature wave through the sample, which is the sum of a transient (DC), and an oscillatory (AC) compo-

nent. The DC term is produced by the effective power dissipated (P), and reaches a constant value, ΔT_{DC}, after a certain time:

$$\Delta T_{DC} \equiv \frac{P}{G} \tag{2.2}$$

where G is the thermal conductance of the sample. The oscillatory component drives a temperature wave across the sample, which can be expressed as follows:

$$\Delta T(r,t) = -\Delta T(r)\cos(2\omega t + \phi) \tag{2.3}$$

where ϕ represents the difference of phase between the input current and the temperature wave.

Due to the temperature variation on the sample surface, the electrical resistance of the heater undergoes an oscillation (ΔR), whose amplitude depends on its temperature coefficient (dR/dT). After the equilibrium of ΔT_{DC} is reached, the change of resistance is given by:

$$\Delta R = \frac{dR}{dT}\Delta T(r)\cos(2\omega t + \phi) \tag{2.4}$$

On the other hand, the voltage drop across the resistance can be obtained by applying the Ohm's law:

$$\begin{aligned} V &= I_0 \sin(\omega t)\,(R_0 + \Delta R) = \\ &= \underbrace{A\sin(\omega t) + B\sin(\omega t + \phi)}_{V_{1\omega}} + \underbrace{C\sin(3\omega t + \phi)}_{V_{3\omega}} \end{aligned} \tag{2.5}$$

where:

$$\left.\begin{aligned} A &= I_0 R_0 \\ B &= I_0 \tfrac{dR}{dT}\tfrac{\Delta T(r)}{2} \\ C &= -I_0 \tfrac{dR}{dT}\tfrac{\Delta T(r)}{2} \end{aligned}\right\} \tag{2.6}$$

We can observe that the voltage drop has two components: one at the input frequency ($V_{1\omega}$), and another one at three times this value

($V_{3\omega}$); the temperature oscillation in the sample is therefore proportional to the amplitude of the third harmonic of the voltage ($V_{3\omega}$):

$$V_{3\omega} = \frac{1}{2} I_0 \frac{dR}{dT} \Delta T(r) \tag{2.7}$$

2.2 Solving the Heat Equation

Once we know how to measure the temperature oscillation across the sample, the next goal is to determine its relationship with the thermal diffusivity (D). This can be calculated by solving the heat equation. As shown in Figure 2.2.a, the distribution of temperature across the sample will depend on the distance to the heater. From the expected heat profile, it is convenient to express the heat equation in cylindrical coordinates:

$$\frac{1}{D}\frac{\partial T}{\partial t} - \left[\frac{1}{r}\frac{\partial}{\partial r}\left(r\frac{\partial T}{\partial r}\right) + \frac{1}{r^2}\frac{\partial^2 T}{\partial \theta^2} + \frac{\partial^2 T}{\partial z^2}\right] = \frac{q(r,t)}{\kappa} \tag{2.8}$$

where κ is the thermal conductivity of the sample and $q(r,t)$ the heating power per unit volume. In the limit of an infinitely narrow and long heater ($l >>$ w), the temperature profile at a distance $l >> r >>$ w is approximately cylindrical ($T = T(r,t)$) and, consequently, it does not depend on θ or z:

$$\frac{1}{D}\frac{\partial T(r,t)}{\partial t} - \left(\frac{1}{r}\frac{\partial T(r,t)}{\partial r} + \frac{\partial^2 T(r,t)}{\partial r^2}\right) = \frac{q(r,t)}{\kappa} \tag{2.9}$$

As discussed in the previous section, there is an oscillatory component of the temperature, which can be written as:

$$T(r,t) = T(r)e^{2i\omega t} \tag{2.10}$$

Introducing this solution in equation 2.9, we obtain:

$$\frac{1}{r}\frac{\partial T(r)}{\partial r} + \frac{\partial^2 T(r)}{\partial r^2} = \frac{2i\omega}{D} T(r) - \frac{P\delta^2(r)}{l\kappa} \tag{2.11}$$

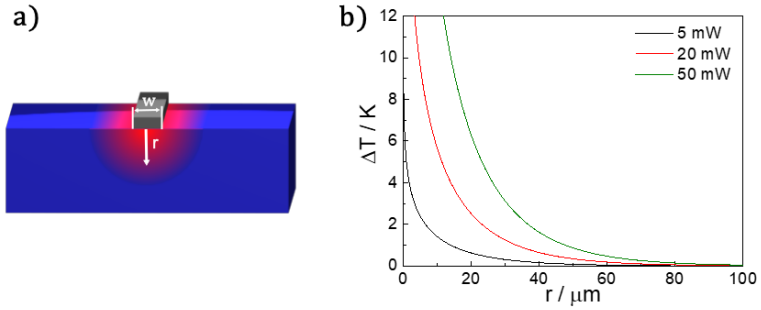

Figure 2.2: a) Scheme of the expected temperature distribution across the sample thickness. 'w' represents the width of the metallic strip and 'r', the radial direction in cylindrical coordinates. b) Solution of the heat equation for different powers dissipated trhough the heater, for a heater of 1 mm long. To calculate the penetration depth, we used the expected value of the thermal diffusivity for the borosilicate glass used in the experiments ($\alpha = 6.6 \cdot 10^{-7}$ m$^2 \cdot$s^{-1}), and set the frequency to 300 Hz.

where we assumed that in the approximation of an infinitely narrow resistance (w $<< l$), the heat is only released at $r = 0$:

$$q(r,t) = P\frac{\delta^2(r)}{l}e^{2i\omega t} \tag{2.12}$$

The solution of this equation is proportional to the modified zeroth-order Bessel function of second kind (K_0) [44, 45]:

$$\Delta T(r) = \frac{P}{\pi l \kappa}\int_0^\infty \frac{\cos\left(\frac{rt'}{\delta}\right)}{\sqrt{t'^2+1}}dt' = \frac{P}{\pi l \kappa}K_0\left(\frac{r}{\delta}\right) \tag{2.13}$$

where δ is the penetration depth of the temperature wave:

$$\delta = \sqrt{\frac{D}{2i\omega}} \tag{2.14}$$

This equation relates the dependence of the amplitude of the oscillation to the thermal conductivity of the sample, and the distance to the

heater (see Figure 2.2.b). In order to obtain an analytical expression to calculate the thermal conductivity, we should apply different approximations. If we analyze the temperature profile close to the surface ($r << \delta$), the Bessel function can be approximated by [37, 46]:

$$K_0\left(\frac{r}{\delta}\right) \simeq -\ln\left(\frac{r}{2\delta}\right) - \gamma \tag{2.15}$$

where $\gamma \simeq 0.5772$ is the Euler-Mascheroni constant. Introducing this approximation into equation 2.13, we obtain:

$$\Delta T(r) \simeq \frac{P}{\pi l \kappa}\left[\ln(2) - \gamma + \frac{1}{2}\ln\left(\frac{D}{r^2}\right) - \frac{1}{2}\ln(2\omega) - \frac{i\pi}{4}\right] \tag{2.16}$$

This equation shows a linear dependence of $\Delta T(r)$ with $\ln(2\omega)$. Consequently, if we measure the temperature oscillation for different input frequencies, we can obtain the thermal conductivity of the sample from the slope of a linear fit. It is worth noting that the amplitude of the thermal wave depends on the thermal diffusivity and on the dissipated power. Consequently, it is necessary to select an appropriate P depending on κ and D of each particular sample (see Figure 2.3 and its discussion).

This solution was obtained supposing a infinitely narrow resistance. However, we can obtain the solution for a strip with a finite width by taking into account the heat generated by many infinitely narrow heaters, i.e., by performing the convolution of equation 2.13 with the spatial heat generation function. To perform the convolution of both equations, we will use the properties of the Fourier space, where the convolution of two functions is transformed into their product, simplifying the calculation. The Fourier cosine transform of equation 2.13 at the surface ($r = |x|$) can be expressed as follows:

$$f_1(k_x) = \int_0^\infty \frac{P\ K_0\left(\frac{|x|}{\delta}\right)}{2\pi l\kappa}\cos(k_x x)dx = \frac{P}{2l\kappa\sqrt{k_x^2 + \left(\frac{1}{\delta}\right)^2}} \tag{2.17}$$

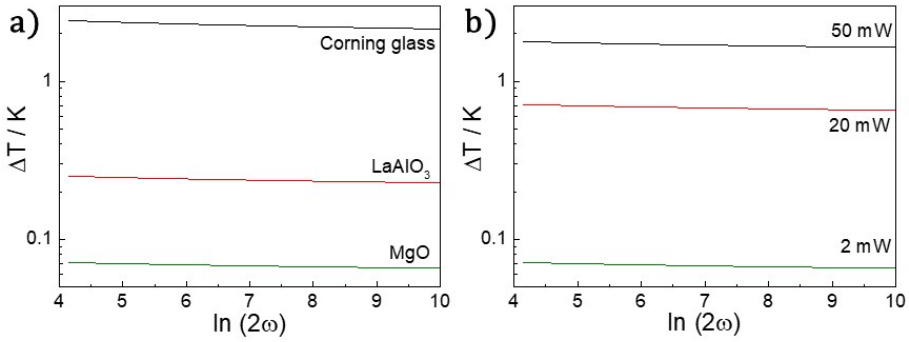

Figure 2.3: a) Comparison between the amplitude of the temperature oscillation between materials with different κ and D at 300 K (Corning glass: $\kappa = 1\,\mathrm{W{\cdot}m^{-1}{\cdot}K^{-1}}$, $D = 6.6{\cdot}10^{-7}\,\mathrm{m^2{\cdot}s^{-1}}$; $LaAlO_3$: $\kappa = 12\,\mathrm{W{\cdot}m^{-1}{\cdot}K^{-1}}$, $D = 4.2 \cdot 10^{-6}\,\mathrm{m^2{\cdot}s^{-1}}$; MgO: $\kappa = 47.4\,\mathrm{W{\cdot}m^{-1}{\cdot}K^{-1}}$, $D = 1.35 \cdot 10^{-5}\,\mathrm{m^2{\cdot}s^{-1}}$). The power dissipated through the resistor is set at 2 mW. b) ΔT for MgO using different dissipated powers. Note that for obtaining a ΔT similar to Corning glass, it is necessary to increase the power ~ 25 times.

On the other hand, the spatial heat generation function can be written as a normalized rectangle function in the x direction:

$$f_2(x) = \frac{\mathrm{rect}\left(\frac{x}{\mathrm{w}}\right)}{\mathrm{w}} \tag{2.18}$$

whose Fourier transform is:

$$f_2(k_x) = \int_0^\infty \frac{\mathrm{rect}\left(\frac{x}{2\mathrm{w}}\right)}{2\mathrm{w}} \cos(k_x x)dx = \mathrm{sinc}(k_x \mathrm{w}) \tag{2.19}$$

In order to obtain the temperature distribution function on the sample surface, we have to perform the inverse Fourier transform of the product of $f_1(k_x)$ and $f_2(k_x)$:

$$\Delta T(x) = \frac{P}{2\pi l \kappa} \int_0^\infty \frac{\mathrm{sinc}\left(\frac{k_x \mathrm{w}}{2}\right) \cos\left(k_x x\right)}{\sqrt{k_x^2 + \left(\frac{1}{\delta}\right)^2}} dk_x \tag{2.20}$$

Finally, the spatial average across the width of the heater leads to the mean temperature measured by the strip:

$$\Delta T = \frac{2}{\mathrm{w}} \int_0^{\mathrm{w}/2} \Delta T(x) dx = \frac{P}{\pi l \kappa} \int_0^{\infty} \frac{\mathrm{sinc}^2\left(\frac{k_x \mathrm{w}}{2}\right)}{\sqrt{k_x^2 + \left(\frac{1}{\delta}\right)^2}} dk_x \tag{2.21}$$

This expression does not have an analytical solution, and has to be solved numerically. However, for very narrow strips the upper limit of the integral can be substituted by the inverse of the half width ($1/b = 2/\mathrm{w}$) and $\mathrm{sinc}(k_x b)$ can be approximated to 1:

$$\begin{aligned} \Delta T &\simeq \frac{P}{\pi l \kappa} \int_0^{1/b} \frac{1}{\sqrt{k_x^2 + \left(\frac{1}{\delta}\right)^2}} dk_x = \frac{P}{\pi l \kappa} \ln \left[\sqrt{1 + \left(\frac{\delta}{b}\right)^2} + \frac{\delta}{b} \right] \simeq \\ &\simeq \frac{P}{\pi l \kappa} \left[\frac{1}{2} \ln\left(\frac{D}{b^2}\right) - \frac{1}{2} \ln(2\omega) + \ln(2) - \frac{i\pi}{4} \right] \end{aligned} \tag{2.22}$$

We observe that the dependence of the temperature profile with frequency is the same than in equation 2.16, actually both equations only differ in the Euler-Mascheroni constant at $r = b$. It is worth noting that the thermal conductivity will be the same in both approximations, as we can obtain it from the slope of a ΔT vs. $\ln(2\omega)$ plot. Therefore, we can write a general solution as a function of a constant η, which depends on the sample diffusivity [38]:

$$\Delta T \simeq \frac{P}{\pi l \kappa} \left[\frac{1}{2} \ln\left(\frac{D}{b^2}\right) - \frac{1}{2} \ln(2\omega) + \eta - \frac{i\pi}{4} \right] \tag{2.23}$$

It is remarkable that the imaginary component in both approximations is independent of the frequency and can be used to identify the range of frequencies where these equations are valid.

Finally, by introducing this solution for the temperature profile into equation 2.7 we obtain:

$$\frac{V_{3\omega}}{V_{1\omega}} = \frac{I_0^2}{4\pi l\kappa}\left(\frac{dR}{dT}\right)\left[\frac{1}{2}\ln\left(\frac{D}{b^2}\right) - \frac{1}{2}\ln(2\omega) + \eta - \frac{i\pi}{4}\right] \tag{2.24}$$

Therefore, if we measure the temperature dependence of the resistance (dR/dT), we can calculate the thermal conductivity of any electrical insulating substrate from the slope (m) of a $V_{3\omega}/V_{1\omega}$ vs. $\ln(2\omega)$ plot:

$$\kappa = \frac{I_0^2\frac{dR}{dT}}{8\pi l m} \tag{2.25}$$

2.3 Thermal conductivity of liquids

To solve the heat equation in the previous section, we have assumed that the heat is dissipated through the substrate. However, if we place a drop of a liquid (or another solid) over the metallic strip, an additional component of the heat flux ($\vec{J_Q}$) across the liquid develops (see Figure 2.4). If we assume that there is not heat transfer between the liquid and the solid, we can solve the equation by supposing two independent heat diffusion processes [47]. Consequently, the solution of the heat equation can be written in a similar way than equation 2.21 [47–49]:

$$\Delta T = \frac{P}{\pi l}\int_0^\infty \frac{\text{sinc}^2\left(\frac{k_x \text{w}}{2}\right)}{\kappa_s\sqrt{k_x^2 + \left(\frac{1}{\delta_s}\right)^2} + \kappa_l\sqrt{k_x^2 + \left(\frac{1}{\delta_l}\right)^2}}dk_x \tag{2.26}$$

where the subscripts 's' and 'l' refer to the substrate and the liquid respectively.

To obtain an analytical solution, we can solve independently the heat equation in each media and then apply the energy conservation principle. In this approximation, the power dissipated is:

$$P = P_s + P_l = \frac{\Delta T_s \pi l \kappa_s}{\mathcal{H}_s(b/\delta_s)} + \frac{\Delta T_l \pi l \kappa_l}{\mathcal{H}_l(b/\delta_l)} \tag{2.27}$$

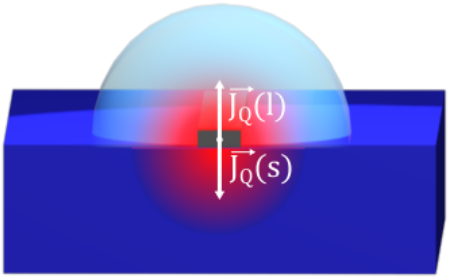

Figure 2.4: Scheme for the heat dissipated through the liquid and the substrate.

where we define $\mathcal{H}_j(x) = -\ln(x) + \eta_j$. If the penetration depths inside the liquid and the substrate are similar, i.e., the difference between the thermal diffusivities are small, we can assume that the temperature oscillation in both media are similar ($\Delta T \simeq \Delta T_s \simeq \Delta T_l$). Therefore, the solution of the heat equation under these approximations is:

$$\Delta T \simeq A \left[\frac{P}{\pi l(\kappa_s + \kappa_l)} \mathcal{H}_l \left(\frac{b}{\delta_l} \right) \right] \tag{2.28}$$

where A is given by:

$$A = \left[1 + \frac{\kappa_s}{\kappa_s + \kappa_l} \left(\frac{\mathcal{H}_l(b/\delta_l)}{\mathcal{H}_s(b/\delta_s)} - 1 \right) \right]^{-1} \tag{2.29}$$

In the approximation of similar thermal diffusivities, A can be approximated to 1 and the equation becomes linear and similar to 2.23. By comparing both equations, we observe that the effective thermal conductivity calculated from a $V_{3\omega}/V_{1\omega}$ vs. $\ln(2\omega)$ plot has the contribution of both the liquid and the substrate:

$$\kappa_e = \kappa_s + \kappa_l \tag{2.30}$$

Therefore, we can obtain the thermal conductivity of the liquid by a simple substration, with the previous measurement of the thermal conductivity of the substrate.

2.4 Experimental determination of κ

Once we know how to obtain the thermal conductivity using the 3ω method, we proceed to build up and optimize a system for these measurements. First, we determined the optimal dimensions of the heater/sensor metallic strip, and the input frequencies in order to stay in the linear regime, where we can use equations 2.23 and 2.28. To do this, we solved numerically the integral of equation 2.21 using the Python code showed in Table 2.1.

```
import numpy as np
from scipy.integrate import quad

def int_r(x,b,rho,Cp,k,f):
   D=k/(rho*Cp)
   d=(D/(2j*f))**.5
   return np.real((np.sinc(x*b))**2/((x**2+(1./d)**2)**.5))

def int_im(x,b,rho,Cp,k,f):
   D=k/(rho*Cp)
   d=(D/(2j*f))**.5
   return np.imag((np.sinc(x*b))**2/((x**2+(1./d)**2)**.5))

f=2*np.pi*np.linspace(5,2000,1000) #Frequencies
#(length, power, width, cond., heat capacity, dens.) in SI
[l,P,w,k,Cp,rho]=[1e-3,5e-3,10e-6,1.,650.,2.23e3]
b=.5*w #half width

DTreal=np.zeros(1000)
for i in range(1000):
   integ = quad(int_r, 0, 1000000, args=(b,rho,Cp,k,f[i]),limit=200)
   DTreal[i]=P*integ[0]/(np.pi*l*k) #Real component

DTimag=np.zeros(1000)
for i in range(1000):
   integ = quad(int_im, 0, 1000000, args=(b,rho,Cp,k,f[i]),limit=200)
   DTimag[i]=P*integ[0]/(np.pi*l*k) #Imaginary component
```

Table 2.1: Python code for the calculation of ΔT vs. $\ln(2\omega)$ for different line widths. The values for the thermal conductivity, heat capacity and density are approximated to the expected values for the borosilicate glass used in the experiments. The lineality increases with the thermal diffusivity, as the approximations performed to solve the heat equation are more accurate.

In Figure 2.5 we represent ΔT vs. $\ln(2\omega)$ for different line widths, observing that for w$= 10\ \mu$m the dependence of the temperature oscillation on frequency is almost linear up to 2 kHz, while the curvature increases for line widths of 30 and $50\ \mu$m, as expected. Consequently, we decided to use $10\ \mu$m widths, the lowest size that we can achieve (routinely) by standard optical lithography in our laboratory.

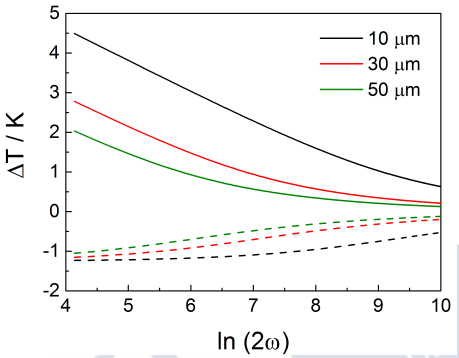

Figure 2.5: Predicted dependence of the temperature oscillation ΔT with frequency for different line widths. Solid and dashed lines represent the real and imaginary components respectively.

On the other hand, to solve the heat equation it is necessary to suppose a cylindrical temperature distribution and, consequently, the length of the strip (l) does not modify the curvature. However, the length of the strip must be much higher than the thermal penetration depth ($10 - 100\ \mu$m) to use this approximation. Furthermore, equation 2.24 shows that the amplitude of the 3ω component is proportional to dR/dT, which depends on the material used and on the value of the resistance, as follows:

$$\frac{dR}{dT} = \alpha(T)R(T) \tag{2.31}$$

where α is a characteristic coefficient of the material, that depends solely on temperature. Therefore, we can increase the signal-to-noise ratio of $V_{3\omega}$ by increasing l, α and R. Taking this analysis into account,

we decided to use 1 mm Pt resistances of thickness between 50 and 100 nm, in a compromise between durability and sensitivity.

Based on the simulations performed in Figure 2.5, we measured the 3ω voltage for input frequencies in the range of 56 to 2119 Hz. From the data plotted in Figure 2.6.a, we determine that the best region to calculate the thermal conductivity is between 86 and 362 Hz. In this range of frequencies, the real and imaginary components are linear and constant respectively, reproducing the dependence of equation 2.24. We use this range of frequencies in all the measurements.

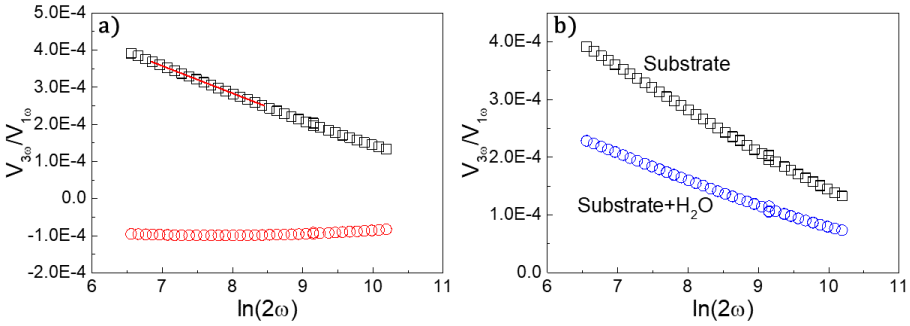

Figure 2.6: a) Real (black squares) and imaginary (red circles) components of the 3ω voltage. b) Comparison of the real component of $V_{3\omega}$ for a metallic strip deposited on top of the bare surface of a borosilicate Corning® glass, and after the deposition of a drop of water over it.

When we deposit a drop of liquid over the resistance, the slope of $V_{3\omega}$ vs. $\ln(2\omega)$ decreases, consistent with a higher apparent thermal conductivity (see Figure 2.6.b). From the difference between the apparent and substrate thermal conductivities, we can calculate the thermal conductivity of the liquid.

Finally, we optimized the method so that sample volumes as small as $\sim$ 0.6 μL can be accurately measured. This allows the possibility of introducing the sample inside a cryostat and measure the thermal conductivity under different cooling/heating ramps, ensuring an optimal thermallization.

To measure κ continuously across a phase transiton, with enough accuracy to detect abrupt and hysteretic changes, it is necessary to reduce the acquisition time of the slope (m) of the $V_{3\omega}/V_{1\omega}$ vs. $\ln(2\omega)$, from the $\sim$ 6 min that it takes under normal conditions in our setup. To do that, we only measured $V_{3\omega}$ at two frequencies (86 and 362 Hz) within the linear regime, decreasing the temperature differences during the calculation of m. Despite this methodology increases slightly the noise of the measurement, the acquisition time decreases to $\sim$ 10 s, which is more appropriate to determine phase transitions accurately under the cooling/heating ramps used (1 K/min) (see Figure 2.7). We have corroborated that the values of the thermal conductivity obtained in the ramp method are accurate, by measuring some points at intermediate temperatures, after reaching a steady state for several minutes and measuring the whole frequency range.

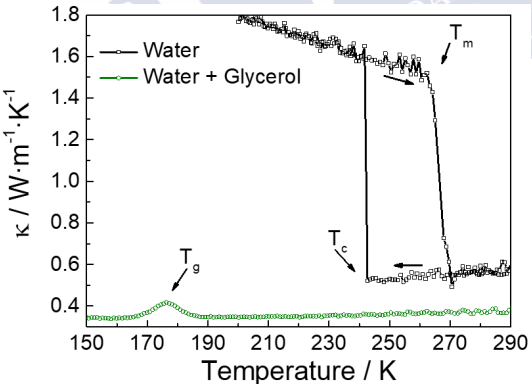

Figure 2.7: Example of the continuous measurement (1 K/min) of $\kappa(T)$ for water and a mixture of water and glycerol at a molar fraction of 0.3. We observe the crystallization and melting of ice at T_c and T_m respectively. By the addition of glycerol, we prevent the crystallization and a glass transition at T_g appears, in accordance to Ref. [50].

2.4.1 Sample preparation

The Pt heater/sensors, of 1 mm long, 10 μm wide and 100 nm thick, were deposited by standard optical photolithography and lift-off, on the top surface of a low thermal conductivity borosilicate Corning® glass (see Figure 2.8.a). We deposited a 10 nm layer of Cr prior to Pt, to ensure a good adhesion to the substrate. The deposition was performed with a GATAN 682 Precision Etching and Coating System (PECS). To perform the electrical connections with the different instruments, the substrate was pasted over a Chip Carrier using silver paint to ensure an optimal thermal contact. Sample and chip pads are wire bonded using Al wire of 30 μm diameter.

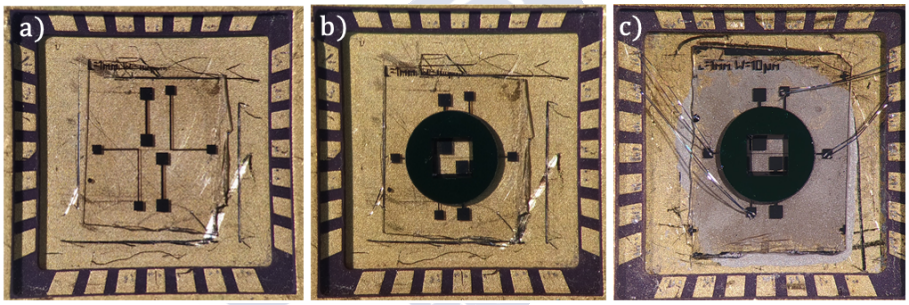

Figure 2.8: Photographs of the experimental setup used for the measurement of the thermal conductivity of liquids. a) Pattern of Pt on Cornign glass, glued on a chip carrier to fit into the cryostat. The inner square of the chip carrier is 7.4×7.4 mm^2. In b) we can observe the PELCO® silicon frame disk with a square aperture of 1 mm^2 and 200 μm of thickness, sealed with Masterbond® EP62-1LPSP epoxy resin, used to hold the liquid; and in c) the wire bonding performed with Al wire of 30 μm of diameter.

To hold liquid samples, we place a PELCO® silicon frame disk with a square aperture of 1 mm^2 and 200 μm of thickness over the platinum strip (see Figure 2.8.b). Inside this receptacle, we place sample volumes between 0.6 and 1.5 μL depending on the evaporation rate of the liquid. To measure the thermal conductivity of liquids with very high vapour pressures, we place a small quartz tube (ϕ = 2 mm) over

the receptacle, which allows us to increase the volume and solve the problems with sample evaporation close to the resistance. The sample was introduced inside a cryostat to perform measurements at different temperatures. To prevent water condensation over the sample at low temperature, the cryostat was purged with He, and the cryogenic measurements were performed under this gas, at 1 atm. This strategy also avoids the evaporation of liquids with high vapor pressures, which could be impossible if the measurements were performed under vacuum.

2.4.2 Cancellation of $\mathbf{V_{1\omega}}$

The 3ω voltage in the Pt heater was measured a Stanford Research Systems SR830 lock-in amplifier. The AC current was injected at ω with a Keithley 6221 AC current source. The typical ratio of $V_{1\omega}/V_{3\omega}$ signals is between $10^3 - 10^6$, depending on the material. Because the maximum input amplitude of the lock-in amplifier is $1\ V$, it is necessary to suppress the 1ω voltage in order to increase the dissipated power and, consequently, obtain an optimal signal-to-noise ratio.

For this task, we designed the circuit shown in Figure 2.9. In this circuit we added an external potentiometer (5K Vishay Foil Resistors series 1240, $\pm 10\ \mathrm{ppm/^oC}$) in series with the metallic resistance deposited on the top surface of the substrate. We selected a potentiometer with very low temperature coefficient, to avoid generating an additional 3ω voltage in this resistance. By adjusting the value of the potentiometer, we can obtain similar voltage drops ($V_{1\omega}$) between the extremes of both resistances, that can be subtracted using three differential amplifiers (Analog Devices AD8221BRZ) in the configuration showed in Figure 2.9.a. In order to perform a first approximation to the heater/sensor resistance and then use the potentiometer to perform a fine tuning, we included three additional resistances in parallel with the potentiometer. The effect on the voltage can be appreciated using an oscilloscope (see Figure 2.10).

Moreover we included two different channels to measure resistances with the same configuration, which can be selected by a manual switch. This configuration allows the simultaneous measurement of two

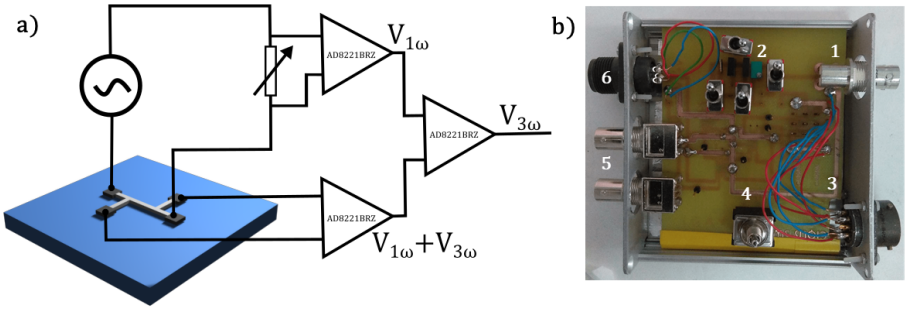

Figure 2.9: a) Scheme of the circuit used to suppress the 1ω voltage. b) Photograph of the circuit designed with the different elements identified: **1)** AC current input, **2)** Low PTC potentiometer and additional resistances, which can be activated using the different switches. We added a first switch to disable the cancellation and allow the measurement of the strip resistance using the same setup. **3)** Connector to the cryostat. **4)** Channel selector. **5)** $V_{3\omega}$ signal output to the lock-in amplifier. **6)** Power supply for the instrumental amplifiers.

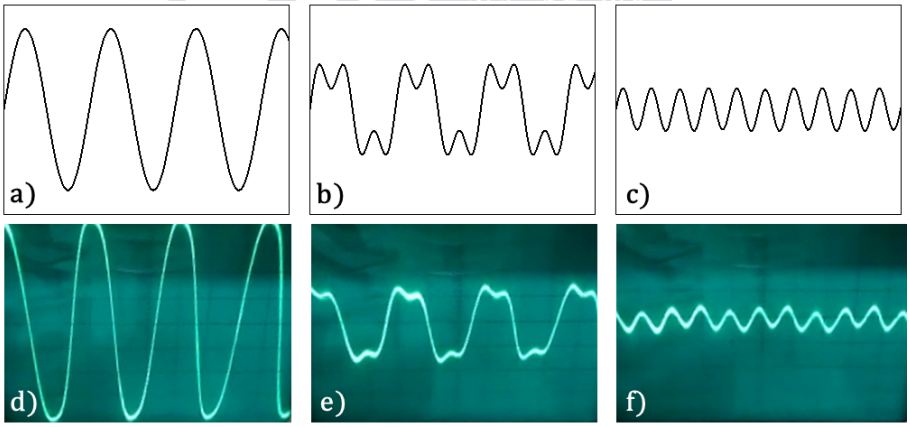

Figure 2.10: a-c) Simulation of the voltage drop for a signal composed of the first and third harmonic ($V = V_{1\omega}\sin(\omega t) + V_{3\omega}\sin(3\omega t)$). The $V_{3\omega}:V_{1\omega}$ ratios are 1:1000, 1:2 and 25:1 respectively, simulating the cancellation process. d-f) Actual pictures of the screen of the oscilloscope, showing the reduction of $V_{1\omega}$ with the electrical circuit described above.

different samples (or substrate, and substrate plus sample) under exactly the same temperature conditions.

2.5 Dependence of η on D

In previous sections, it was demonstrated that the thermal conductivity of solids and liquids can be obtained from a linear fit of $V_{3\omega}$ vs. $\ln(2\omega)$. However, equation 2.24 also shows that the intercept has information about the diffusivity ($D = \kappa/\rho C_p$) and, consequently, about the heat capacity C_p . In order to measure the heat capacity using the 3ω method, it is necessary to obtain the dependence of η with the diffusivity [28], which develops from the difference between equation 2.21 and the approximation in Eq. 2.22.

The parameter η, must be proportional to the difference of the arguments of both integrals:

$$\eta \propto \frac{1}{\sqrt{x^2 + \left(\frac{1}{\delta}\right)^2}} - \frac{\mathrm{sinc}(bx)}{\sqrt{x^2 + \left(\frac{1}{\delta}\right)^2}} \tag{2.32}$$

Performing the power series expansion of both terms we obtain:

$$\begin{aligned} \eta \propto \delta - \frac{1}{2}\delta^3 x^2 + O(x^4) - \delta + \frac{(3\delta^2 + b^2)\delta}{6} x^2 + O(x^4) \simeq \\ \simeq \frac{\cancel{-3\delta^3} + \cancel{3\delta^3} + b^2\delta}{6} x^2 = \frac{1}{6} b^2 \delta x^2 \Longrightarrow \boxed{\eta \propto \delta \propto D^{1/2}} \end{aligned} \tag{2.33}$$

To probe the dependence of η with $D^{1/2}$, we measured independently, the thermal conductivity (using the 3ω method) and the heat capacity (using a Physical Properties Measurement System, PPMS, of Quantum Design) of several single crystal oxide substrates, as well as of Corning glass, at different temperatures (see Figures 2.11.a-b). Using the value of heat capacity, we calculated the value of η given by equation 2.24. In Figure 2.11.c we represent η vs. $D^{1/2}$, confirming the linear behaviour predicted by equation 2.33. By introducing this fit into equation 2.24, we can calculate the heat capacity of different liquids, resulting in

values similar to those obtained by other experimental techniques (see Table 2.2 and further discussion in the experimental chapters).

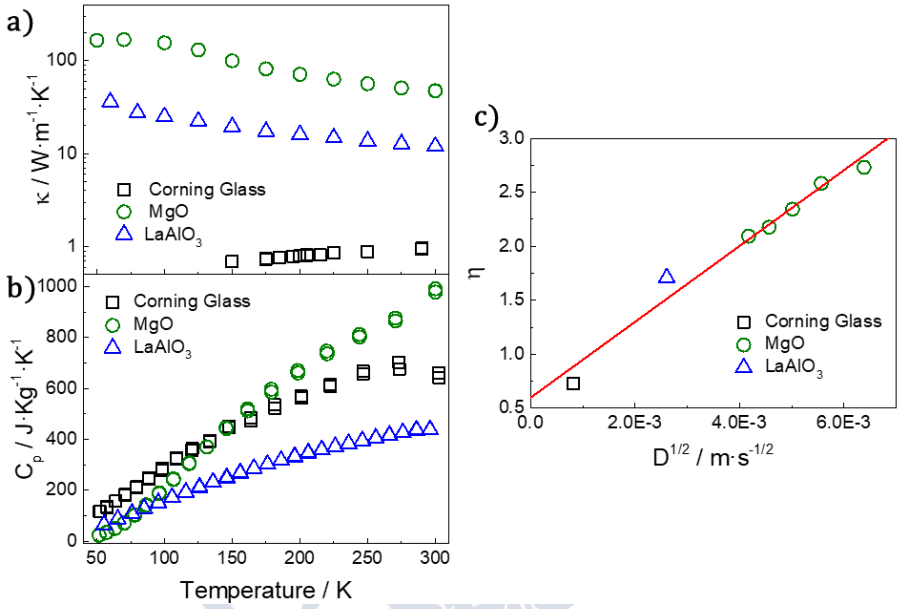

Figure 2.11: a-b) Thermal conductivity (κ) and heat capacity (C_p) for several substrates at different temperatures. c) Dependence of η on substrate diffusivity. The diffusivity of MgO was calculated in between 150-300 K, while for $LaAlO_3$ and Corning glass we only plot the value at 300 K due to the small temperature dependence of the diffusivity. The data shows a linear behavior $\eta = a + bD^{1/2}$, where $a = 0.60 \pm 0.12$ and $b = 351 \pm 27$ $\mathrm{m}^{-1}\cdot\mathrm{s}^{1/2}$.

We want to remark the interesting possibilities that offer the possibility of measuring both κ and C_p in such a small volumes. Obtaining certain types of nanoparticles, biological molecules, or many other solutes in large quantities, is sometimes a problem that can make their characterization difficult using techniques that require sample volumes of a few millilitres. Lowering these volumes to the microliter range will help to overcome those barriers.

Name	C_p (exp.)	C_p (lit.)
	$J \cdot mol^{-1} \cdot K^{-1}$	
Trimethylpropane trioleate	1849 ± 84	1798[51]
Polyethylene glycol 400	732 ± 32	835.6[52]
Dimethylformamide	160.0 ± 6.0	146.05[53]
1-Butyl-3-methylimidazolium triflate	375 ± 10	421.6[54]

Table 2.2: Comparison between the heat capacity obtained in our setup, and the values reported in literature, for some liquids. The differences are between 3 and 12%. The measurements were performed at 293 K.

2.6 Finite-element simulation of the convective flow

The differences in temperature across the liquid produced by the heat dissipated induce a convective flow which contributes to the heat transport, and is a source of error in the value of the thermal conductivity (the conductive component of heat dissipation). To analyse the effect of the convective flow in our setup, we performed finite-element simulations using COMSOL® [55].

We defined a geometry similar to our experimental setup, with a semi-spherical drop of polyethylene glycol of 1 μL over a 500 μm thick silica glass substrate. We also included a Au strip with the same dimensions than in our experimental setup (1 mm $\times$ 10 μm $\times$ 100 nm). To perform the simulation, we used the following physics-based models included in the program:

- **Joule Heating**.- This model defines the current driven through the resistance and the heat dissipated by the heater, which was fixed to 5 mW, a typical value in our measurements. We set the initial temperature and the temperature at the outside surfaces to 293.15 K, where we have supposed that the penetration depth of the thermal wave is much smaller than the thickness of the sub-

strate and the radius of the droplet. We also assumed that there is not significant heat transport between the substrate and the liquid, so we thermally isolated the top surface of the substrate.

- **Heat Transfer in Liquids**. We set the pressure at 1 atm, the initial temperature at 293.15 K and the boundary conditions as in the previous model. We selected a natural convective heat flow for the heat flux.

- **Laminar Flow**. We selected a Newtonian liquid with static initial conditions and no fluid displacement at the outside drop walls.

The results of the simulation are presented in Figures 2.12.a and 2.12.c, observing that both the temperature and the convective flow are equilibrated after $\sim$ 100 seconds. For comparison, we also performed the simulation for a common geometry and input current in Hot-wire methods [56], observing that the fluid velocity is three orders of magnitude lower in our setup (Figure 2.12.b, note the different scales in the velocity profiles).

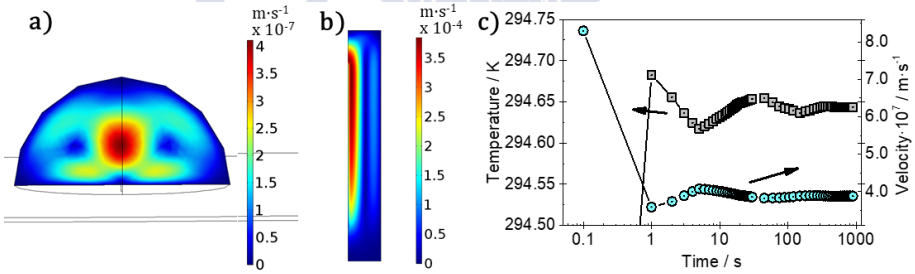

Figure 2.12: a-b) Comparison between the convective flow of our 3ω-based setup, and hot-wire methods, respectively. Note the different scale in the temperature profiles of both cases. c) Temperature distribution at the center of the strip and maximum flow velocity.

In order to analyze if this convective flow contributes significantly to the thermal transport, we can use the Rayleigh number and determine the ΔT_{crit} (Eq. 1.2), which indicates the lower temperature difference

necessary to produce a significant convective flow. The value of ΔT_{crit} obtained for PEG at 300 K is $\sim 10^{10}$ K, in this geometry, in perfect accordance with the small fluid velocity obtained from the simulations. This demonstrates that the small size of our system reduces dramatically the convective flow and, consequently, its contribution to the heat transport becomes negligible.

3. Experimental techniques

In this thesis we demonstrate the utility of the study of the heat transport for the understanding of fluids of different types. However, the complexity of the phenomena observed makes necessary the use of complementary experimental techniques and methodologies, in order to fully understand and discuss in deep the results obtained. In the following sections I will describe, briefly, the foundations of the main experimental techniques used in this project.

3.1 Differential Scanning Calorimetry

Differential Scanning Calorimetry, DSC, is one of the most used experimental techniques for the analysis and characterization of phase transitions, and provides the enthalpy and entropy associated to them [57].

A DSC calorimeter is composed by two cells, a reference (an Al pan) and the sample under study (an Al pan plus the sample; see Figure 3.1). When a temperature ramp (dT/dt) is programmed, a certain amount of heat is transferred to each cell, so they maintain exactly the same temperature (T_0). The heat flow rate (Φ) in each cell depends on the specific heat capacity ($c_p = C_p/m$) of the material:

$$\Phi = c_p \cdot \mathrm{m} \cdot \frac{dT}{dt} \tag{3.1}$$

In order to obtain Φ, the system measures the difference of temperature between both cells, which is proportional to the difference of the heat flow rate:

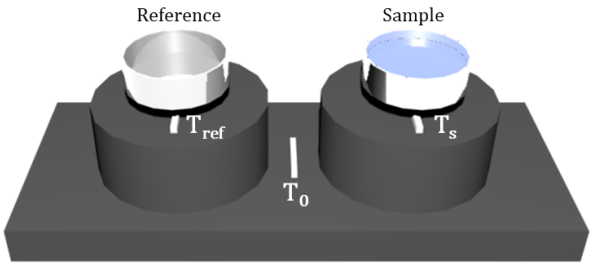

Figure 3.1: Scheme of the experimental setup of a Differential Scanning Calorimeter (DSC). For measuring the reference (T_{ref}), sample (T_s) and set point (T_0) temperatures, three individual heater and sensor thermocouples are placed below the two cells and in the center.

$$\Delta\Phi \propto T_s - T_{\text{ref}} \tag{3.2}$$

Under these conditions, the heat flow measured ($\Delta\Phi$) is proportional to the specific heat capacity of the substance studied:

$$\Delta\Phi = \Phi_s - \Phi_{\text{ref}} = \Phi_{\text{m}} + \Phi_{\text{pan}} - \Phi_{\text{pan}} = \Phi_{\text{m}} \propto C_p \tag{3.3}$$

where Φ_{m} is the extra heat flow due to the presence of the material. To determine the heat capacity of the sample, it is necessary to know the coefficient of proportionality (β) between the heat flow rate and the heat capacity. For this task, it is used a three-step procedure:

1. First, we measure the differences between the heat flow rate of the two empty pans used in the experiments (Φ_0). By performing this measurement, we can cancel the contribution of the inevitable asymmetries inside the DSC.

2. After measuring the base line, we introduce a reference sample with a calibrated heat capacity. This measurement allows to determine the proportionality constant β, which can be written as:

$$\beta = \frac{\Phi(\text{cal}) - \Phi_0}{c_p(\text{cal}) \cdot \text{m}(\text{cal})} \tag{3.4}$$

For increasing the accuracy, it is important to use a substance with a heat capacity similar to the value expected for the sample under study.

3. Finally, the heat flow rate of the substance studied can be written as:

$$\Delta\Phi(s) = \Phi(\mathrm{s}) - \Phi_0 = \beta \cdot c_p(\mathrm{s}) \cdot \mathrm{m(s)} \tag{3.5}$$

Therefore, by introducing equation 3.4 into 3.5, we can obtain the specific heat capacity of a substance:

$$c_p(s) = \frac{\Phi(s) - \Phi_0}{\Phi(\mathrm{cal}) - \Phi_0} \cdot \frac{\mathrm{m(cal)}}{\mathrm{m(s)}} \cdot c_p(\mathrm{cal}) \tag{3.6}$$

To ensure a quasi-static (equilibrium) regime during the measurement, we programmed a very slow ramp ($0.1\ \mathrm{K \cdot min^{-1}}$) from 3 degrees below the desired temperature (see Figure 3.2). Using this strategy, the error in the heat flow introduced by the thermal lag after starting the ramp is reduced considerably.

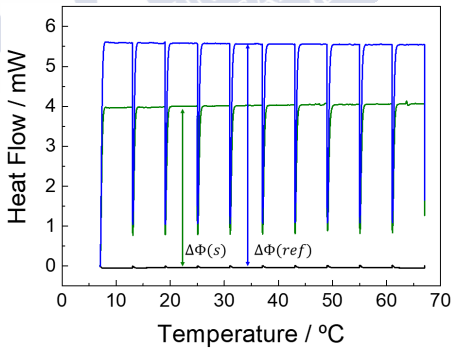

Figure 3.2: Heat capacity measurement at different temperatures of an aqueous solution of tetrabutylammonium bromide (TtBABr) at a concentration of [TtBABr]=6 m (green). We use water as reference substance (blue) and perform a previous background measurement of the two empty cells (black). The heat capacity is calculated from the heat flow using equation 3.6.

3.1.1 Phase transitions

The analysis of the heat capacity change is a powerful tool to determine the type and order of phase transitions [58,59]. By studying the different peaks observed in the DSC thermogram (Figure 3.3), it is possible to identify if the phase transition is a crystallization/melting (first-order) or a glass transition (second-order). An increase in the heat flow from the heater to the sample is produced by an exothermic event, while an endothermic process leads to a decrease of the heat transferred.

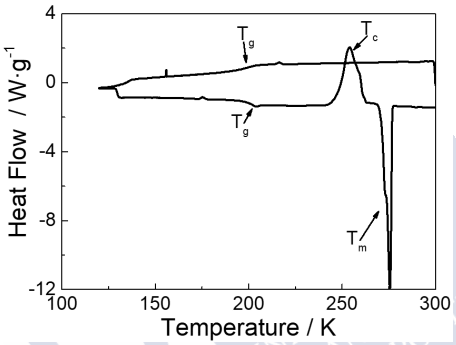

Figure 3.3: DSC thermogram for the ionic liquid 1-Methyl-3-octylimidazolium hexafluorophosphate. $\mathrm{T_g}$, $\mathrm{T_c}$ and $\mathrm{T_m}$ represent a glass transition, a crystallization and its melting respectively.

First-order phase transitions produce a change in the arrangement of the molecules of the system, leading to a discontinuity in the entropy (S). This sudden change in the entropy results in an absorption or a release of heat (latent heat, ΔH), which is observed in the DSC thermogram. For instance, in a crystallization process the entropy decreases and, consequently, the heat is released showing an exothermic peak, while a crystal-to-liquid transition produces an endothermic peak. The amount of heat associated to the phase transition can be obtained by integration of these peaks.

On the other hand, second-order phase transitions do not have associated a change in the order of the system and, consequently, the entropy

is continuous and does not involve a latent heat. However, the heat capacity ($C_p = T \cdot dS/dT$) shows a discontinuity. As we have shown in equation 3.3, the heat flow rate is proportional to the heat capacity and, consequently, we observe a discontinuity in the DSC thermogram. Contrary to first-order phase transitions, in this class of processes there is not any hysteresis between the solid-to-liquid and liquid-to-solid transitions.

In this project we use two different Differential Scanning Calorimeters. For the characterization liquid-to-solid phase transitions we use a TA Instruments Q200 DSC equipped with a Refrigerated Cooling System RCS90, which allows the measurement in a broad range of temperatures (-90 ^{o}C $< T <$ 550 ^{o}C). Despite this system is ideal to obtain a complete phase diagram, the low sample volume used reduces the accuracy on the determination of C_p. For this reason, we also used a Setaram Micro DSC-III calibrated with water to measure heat capacities. This instrument gives an accurate measurement of C_p but has a limited temperature range (6 to 70 ^{o}C).

3.2 Polarized Optical Microscopy

In the previous section we observe how to detect phase transitions by Differential Scanning Calorimetry. Despite this technique is very sensitive to phase transitions, sometimes it is difficult to distinguish between the formation of crystals or liquid crystals.

Liquid crystals have the ability to flow, as liquids, at the time that break rotational and traslational symmetries along a certain direction, like solid crystalline materials. Thus, isotropic-to-liquid-crystal phase transitions appears similar than a simple crystallization in the DSC thermogram, and makes necessary the use of complementary experimental techniques to analyze the different phases formed in a system.

One of the most used techniques to distinguish between the formation of liquid crystals and conventional crystallization is the Polarized Optical Microscopy (POM). This technique uses the birefringence produced in optically anisotropic materials, like liquid crystals [60]. In

these systems, the physical properties are strongly anisotropic; particularly, the refractive index depends on the incident direction and, consequently, light is refracted differently along different directions.

Light is an electromagnetic wave of frequency ω propagated in a direction $\vec{k}$ perpendicular to both the electric $\vec{E}$ and magnetic $\vec{B}$ fields [61]:

$$\vec{E} = \vec{E}_0(r,t)\cos\left(\vec{k}\vec{r} - \omega t\right) \tag{3.7}$$

As we observe in this equation, the direction of $\vec{E}_0$ can also be time dependent and will determine the polarization state of the light. In linearly polarized light the orientation of the electromagnetic field is constant:

$$\vec{E} = \left(E_{0x}\hat{i} + E_{0y}\hat{j} + E_{0z}\hat{k}\right)\cos\left(\vec{k}\vec{r} - \omega t\right) \tag{3.8}$$

Lets suppose now two perpendicular light waves propagated in the same region of the space and in the z direction:

$$\begin{aligned}\vec{E}_1(z,t) &= E_{0x}\cos(kz - \omega t)\hat{i}\\ \vec{E}_2(z,t) &= E_{0y}\cos(kz - \omega t + \varepsilon)\hat{j}\end{aligned} \tag{3.9}$$

where ε is the phase difference between the two waves. Then, the resultant wave can be expressed as:

$$\vec{E} = \vec{E}_1 + \vec{E}_2 = E_{0x}\cos(kz - \omega t)\hat{i} + E_{0y}\cos(kz - \omega t + \varepsilon)\hat{j} \tag{3.10}$$

Depending on the value of ε, the resultant wave will have a different polarization:

- **Linear Polarization**. If $\varepsilon = \pm n\pi$ $(n = 0, 1, 2, 3...)$, the resultant wave would be:

  $$\vec{E} = \left(E_{0x}\hat{i} \pm E_{0y}\hat{j}\right)\cos(kz - \omega t) \tag{3.11}$$

  which is again linearly polarized.

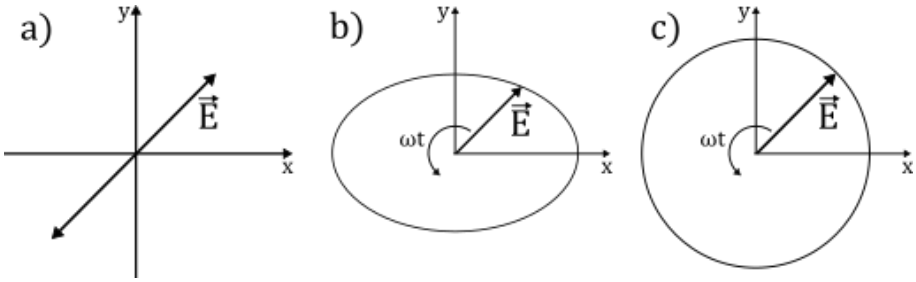

Figure 3.4: Scheme of the profile in the x-y plane formed by $\vec{E}(t)$ for the different types of polarization.

- **Elliptical Polarization**. When $\varepsilon = \pm\left(n + \frac{1}{2}\right)\pi$ the orientation of $\vec{E}$ depends on time:

$$\vec{E} = E_{0x}\cos(kz - \omega t)\hat{i} \pm E_{0y}\sin(kz - \omega t)\hat{j} \tag{3.12}$$

  This function describes an ellipse in the x-y plane whose axis are E_{0x} and E_{0y} (see Figure 3.4.b)

- **Circular Polarization**. In the particular situation when $E_{0x} = E_{0y} = E_0$, the modulus of the field is constant and the ellipse converges into a circle (see Figure 3.4.c).

$$\vec{E} = E_0\left[\cos(kz - \omega t)\hat{i} \pm \sin(kz - \omega t)\hat{j}\right] \tag{3.13}$$

Furthermore, the refractive index (n) is defined as the ratio between the speed of light in vacuum (c) and the speed of light through a certain material (v) [61]:

$$n = \frac{c}{v} \tag{3.14}$$

where n must be ≥ 1. Some systems, like liquid-crystals, have two different refractive indexes depending on the direction. This effect is known as birefringence and the axis with different n is called optical axis, which is usually defined as x-axis. It is particularly interesting the effect of this kind of materials on linearly polarized light.

The strategy used in POM is to introduce two linear polarizers between the light source and the eyepiece of a microscope, which is usually replaced by a camera [60]. The first is used to linearly polarize the light in a certain optical axis. The second is called analyzer and it is common to set its axis perpendicular to the first one (crossed polarizers). In this configuration, the light does not come out from the second polarizer if there is not any sample between both polarizers, or if it is optically isotropic.

Imagine now that the linearly polarized light beam, generated by the first polarizer, is propagated along the z direction, as defined by equation 3.11, passing across an optically anisotropic material. In this situation, the component parallel to the optical axis $\vec{E}_x$ travels at a different velocity than the y-component $\vec{E}_y$. Consequently, it is introduced a phase difference ε between them, which depends on the difference between the refractive indexes and on the thickness of the material. In general, the light wave which comes out from the material can be expressed as:

$$\vec{E}_{out} = E_{0x}\cos(kz - \omega t)\hat{i} + E_{0y}\cos(kz - \omega t + \varepsilon)\hat{j} \tag{3.15}$$

which may or may not be linearly polarized, depending on ε, as we shown previously. Consequently, the component of the resultant wave parallel to the optical axis of the second polarizer will pass through it, and will be observed through the objective of the microscope [60].

Finally, the dependence of the refractive index on frequency produces the dispersion of the incident light and leads to the beautiful colors observed in Figure 3.5, and which are so characteristic of liquid crystals; see for example the images in reference [60].

By comparing POM and thermal conductivity measurements, we were able to identify transitions between different types of ordered and isotropic phases. Particularly, the analysis of the ionic liquids studied in this work, at different temperatures, using both techniques, allowed us to demonstrate the spontaneous nucleation of tiny crystals within a glassy phase, undetectable through X-ray diffraction, and not reported before [62].

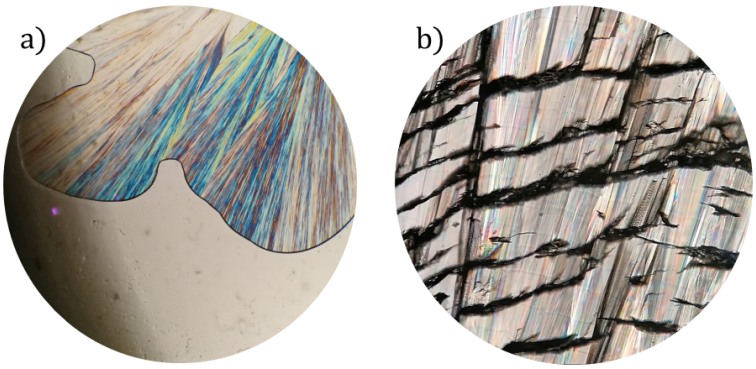

Figure 3.5: Examples of POM images for two crystallized ionic liquid: a) 1-Butyl-3-methylimidazolium trifluoromethanesulfonate and b) 1-Ethyl-2,3-dimethylimidazolium bis(trifluoromethylsulfonyl)imide, at 200 K and 240 K respectively. Images were recorded using an Olympus BX51-P Polarized Light Microscope. The sample was introduced in a Linkam LTS350 stage, and the temperature was controlled using a Linkam TMS94 Temperature Controller.

3.3 Infrared Spectroscopy

In the previous section we centered our analysis on how light-matter interaction changes its velocity and polarization. However, when a light beam goes through a material, some frequencies of the light are absorbed, causing the different colors in nature. The analysis of these absorbed frequencies gives important information about the interactions and arrangement at molecular level and, as we will discuss, can be very important to understand the propagation of heat through vibrational coupling between different molecules in a fluid [15, 16, 28, 63].

In the simplest approximation, low energy intermolecular an intramolecular vibrations can be treated as the interaction between two particles of masses m_1 and m_2 connected by a spring [59]. In this situation, the system vibrates as a simple harmonic oscillator of reduced mass μ:

$$\mu = \frac{m_1 \cdot m_2}{m_1 + m_2} \tag{3.16}$$

whose potential energy is:

$$V = \frac{1}{2}k(r - r_0)^2 \tag{3.17}$$

In this analogy with an harmonic oscillator, the force constant k represents the strength of the bond between two atoms or molecules. By solving the equation of motion, we can obtain the characteristic frequency of vibration of this oscillator:

$$\nu = \frac{1}{2\pi}\sqrt{\frac{k}{\mu}} \tag{3.18}$$

At molecular level it is necessary to solve the Schrödinger equation under this potential, whose solution is:

$$E = \left(n + \frac{1}{2}\right) h\nu \tag{3.19}$$

where h is the Planck's constant, ν is the characteristic frequency of the oscillation and $n = 0, 1, 2...$ is a positive integer number. This equation leads to quantified energy levels separated by a constant:

$$\Delta E = h\nu \tag{3.20}$$

This equation is the Bohr's frequency condition, which establishes that only photons of energy ΔE will be absorbed and produce an excitation to a higher energy level. This restriction for the absorption frequencies leads to the different colors of matter and is the principle of spectroscopy. It is worth noting that it is common to represent the wavenumber ($\bar{\nu}$) instead of the frequency. Both magnitudes are related as follows:

$$\bar{\nu} = \frac{\nu}{c} \tag{3.21}$$

where c is the speed of light.

The characteristic wavelengths for the different types of vibrational modes of a molecule are in the infrared part of the spectrum ($\bar{\nu} \sim 10^2 - 10^4\ \mathrm{cm}^{-1}$) [64], so the study of this kind of processes is called Infrared Spectroscopy (IR). Particularly, intramolecular vibrations are usually situated in the mid-IR region ($400 - 4000\ \mathrm{cm}^{-1}$), while intermolecular modes like hydrogen bonds are placed in the far-IR region ($10 - 400\ \mathrm{cm}^{-1}$) [65].

By shining light of different frequencies to the sample, and observing the absorption bands, we can determine ΔE of the molecular vibrations produced in the molecules of the system. This analysis allows us to identify changes on the type and strength of the molecular interactions, and is a very important aid for a complete understanding of heat transport in liquids, as we will discuss further in the next chapters.

Finally, in order to disentangle the different absorption bands in the spectrum, it is important to know the possible vibrational modes of the molecule under study. The number of possibilities depends on the amount of atoms forming part of the molecule (N) and on its distribution. In general, it can be determined using the following rule [66]:

- Linear molecules: $3N - 5$
- Non-linear molecules: $3N - 6$

Despite the number of absorption bands in an IR spectrum can be large for complex molecules, we can separate it in some common groups with known characteristic frequencies. This simplification allows to identify and separate the different contributions to the spectrum.

3.3.1 Spectrum of H_2O

Because of the relevance of water in this project, its characteristic absorption bands will be detailed. In the spectrum of pure water we can distinguish five absorption bands: three intramolecular (O-H) and two intermolecular due to the presence of hydrogen bonds [67] (see Figure 3.6):

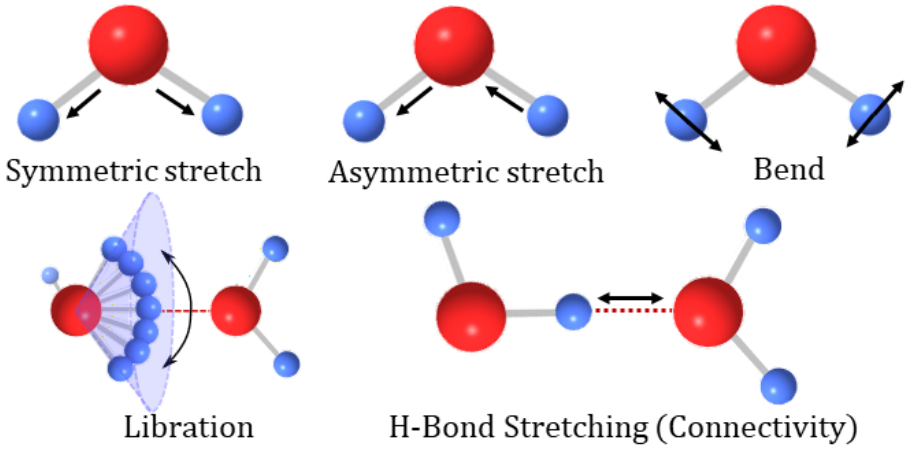

Figure 3.6: Scheme of the motion associated to the intramolecular (top) and intermolecular (bottom) vibrational modes of water.

1. **Stretching Band** ($\bar{\nu} \approx 3400\ \mathrm{cm}^{-1}$). Oscillations of the distance between hydrogen and oxygen around the equilibrium position. This can be symmetric if both bond lengths increase and decrease simultaneously, or asymmetric if one bond is lengthening while the other is shortening.

2. **Bending Band** ($\bar{\nu} \approx 1650\ \mathrm{cm}^{-1}$). Oscillation of the angle between the two O-H bonds.

3. **Libration Band** ($\bar{\nu} \approx 675\ \mathrm{cm}^{-1}$). Rotation of the whole molecule around the hydrogen bond axis.

4. **Connectivity Band** ($\bar{\nu} \approx 200\ \mathrm{cm}^{-1}$). Vibrations of the hydrogen bond (O-H$\cdots$O).

However, some vibrational modes can be coupled and lead to new absorption bands. For example, at $\approx 2100\ \mathrm{cm}^{-1}$ there is a tiny peak in the spectrum of water originated by an anharmonic coupling of bending and libration modes (see Figure 3.7) [68]. The position and intensity of this band are highly sensitive to the characteristic hydrogen bond

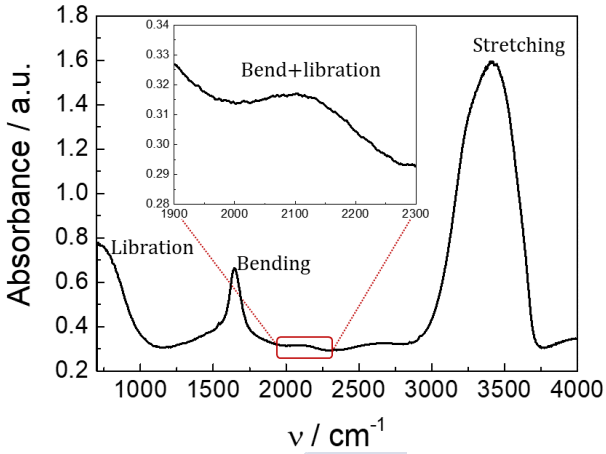

Figure 3.7: Mid-IR spectrum of pure water. The inset shows the peak observed around 2100 cm^{-1}, which is associated to the bend+libration combination band.

structure of water, and can be used to detect collective changes on it due to the presence of different solutes [69].

3.3.2 FTIR spectrometer

In order to collect the IR spectrum of a substance, the most used technique is the Fourier Transform Infrared spectroscopy (FTIR). These instruments measure the interference pattern (interferogram) produced when two light beams travelling different distances interact. They are composed by an infrared light source, an interferometer and a detector.

When a light beam of a single wavelength λ passes though an interferometer, it produces a certain interference pattern (interferogram) depending on λ. However, the IR source generates light in a broad range of frequencies, leading to a complex interferogram which is the convolution of all single wavelength patterns [70].

To disentangle this interferogram, FTIR spectrometers perform the Fourier transform of the composed signal detected. In general, the Fourier transform $f'(x)$ of any function $f(x)$ can be expressed as [71]:

$$f'(x) = a_0 + \sum_{n=1}^{\infty} [a_n \cos(nx) + b_n \sin(nx)] \tag{3.22}$$

where the coeficients a_0, a_n and b_n are given by:

$$\left.\begin{aligned} a_0 &= \frac{1}{2\pi}\int_{-\pi}^{\pi} f(x')dx' \\ a_n &= \frac{1}{\pi}\int_{-\pi}^{\pi} f(x')\cos(nx')dx' \\ b_n &= \frac{1}{\pi}\int_{-\pi}^{\pi} f(x')\sin(nx')dx' \end{aligned}\right\} \tag{3.23}$$

The fundamental parameter in an interferogram is the absolute difference between the path lengths (δ) of the two light beams passing across the interferometer. The interference is constructive if δ is a multiple of the wavelength, while it is destructive for odd multiples of $\lambda/2$. Therefore, the interferogram is an even function and consequently b_n is always zero.

By applying the Fourier transform to the interferogram, we can separate a certain function into its sinusoidal components of a specific frequency. As we said, each wavelength produces an interference pattern with a certain periodicity and, consequently, will contribute to only one term of the series. The coefficient a_n gives information about the relative intensity of each frequency.

When a substance is placed between the interferometer and the detector, some of the frequencies will be absorbed depending on the type and strength of the bonds. This absorption will be reflected in the coefficient a_n associated to these wavelengths. Consequently, by performing the Fourier transform of the resulting interferogram, we obtain the IR spectra of the substance under study.

Depending on the IR regime we are interested in, we have to use different instruments, as beamsplitters and sample cells which do not absorb light in this regime are necessary. For room temperature mid-IR measurements we use a Nicolet 6700 FTIR spectrometer from the Functional Materials and Nanotechnology Group (CIQUS, USC), and

the samples were placed inside CaF_2 cells. We also perform cryogenic measurements by introducing the cell in a Oxford Instruments DN1704 liquid-N_2 cryostat during a research stay at the Van't Hoff Institute for Molecular Sciences. Temperature was controlled using an Oxford Instruments ITC4 temperature controller and a K-type thermocouple fixed close to the sample. These measurements were performed using a Perkin Spectrum Two FTIR spectrometer. For collecting the far-IR measurements, we use a Bruker Vertex 70v FTIR spectrometer from the IR-Raman services of RIAIDT-USC, equipped with a DLaTGS detector. Samples were mixed with polyethylene powder and pressed into 13 mm diameter pellets.

As we will discuss in the experimental chapters of this thesis, combining IR spectroscopy and thermal conductivity measurements, we demonstrate that very low amounts of ethanol in water can lead to the strengthening of the cooperative H-bond structure of water and improve the heat transport [72]. We also detect the formation of supramolecular structures in aqueous solutions of tetrabutyammonium bromide, with important applications in energy storage and conversion [73].

Finally, by studying the relation between the thermal conductivity and the strength of the H-bonds in ionic liquids, we demonstrate that strong H-bonds between anion and cation difficult the crystallization of ionic liquids, up to the point to be impeded [62].

These are only three examples of the large number of applications that offer the combination of both techniques for studying and understand complex systems.

3.4 Density and speed of sound

In order to calculate the thermal diffusivity (α) from thermal conductivity (κ) and heat capacity (C_p), it is necessary to know the density (ρ) of the material under study:

$$\alpha = \frac{\kappa}{\rho \cdot C_p} \tag{3.24}$$

Moreover, changes on the dependence of the density with the temperature or the solute concentration are indicative of changes in intermolecular distances. Consequently, the analysis of the density, and how it correlates with changes in the thermal conductivity, is fundamental to understand their effect on the heat transport [3].

As we have discussed in Chapter 1, thermal conductivity depends on the mean distance between molecules and on the velocity of energy exchange along their bonding paths. In the introduction chapter, we have demonstrated that the thermal conductivity depends on the sound velocity and on the adiabatic compressibility ($K = 1/\rho v^2$)), as follows:

$$\kappa \propto \delta \cdot v_s \propto \delta^{-1/2} \cdot K^{-1/2} \tag{3.25}$$

Therefore, the measurement of the sound velocity, and its relation with the thermal conductivity, allows to understand if the variations of the heat diffusion observed are produced by changes on the type and strength of the intermolecular bonds (and consequently on their sound velocity and compressibility), or if they are caused by changes on the mean interatomic distances.

For these reasons, we measured the density and sound velocity for the different systems treated in this thesis. For this task, we used an Anton Paar DSA 5000 (Propiedades Termofísicas e Superficiais de Líquidos Group, USC), which allows the simultaneous measurement of both magnitudes by combining two inline cells introduced inside a thermostat (see Figure 3.8), which allows measurements in a temperature range of 6 to 70 ^{o}C [74].

For measuring the sound velocity, the sample is placed between two piezoelectric ultrasound transducers separated $d = 5$ mm; one of the transducers emits sound waves at 3 MHz, which are received by the other after a certain time (t). Dividing this time by the distance between the transducers, we can obtain the sound velocity (v_s). However, in order to obtain an accurate measurement, the equation programmed in the system apply some corrections due to thermal effects on d and electronic effects, and it can be expressed as:

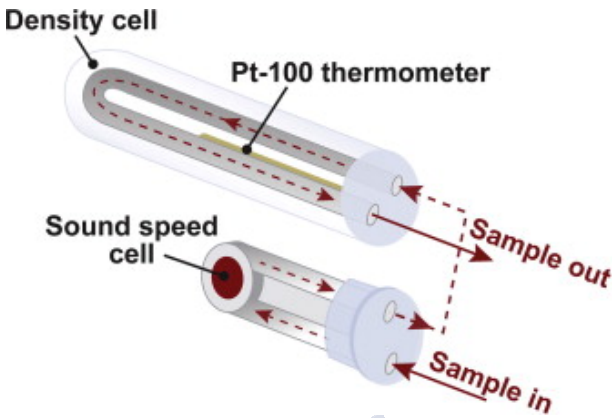

Figure 3.8: Scheme of the cells used for the measurement of the density and speed of sound. Reprinted from [74] with permission from Elsevier.

$$v_s = \frac{d \cdot (1 + 1.6 \cdot 10^{-5} \cdot \Delta T)}{\frac{t}{512} - \tau \cdot f_3} \tag{3.26}$$

where ΔT is the difference of temperature respect 293 K, τ is the time delay of the electronics and f_3 a temperature correction factor of τ. In order to obtain all these parameters, it is necessary to perform a calibration with water and dry air at different temperatures, prior to each set of measurements.

Density measurement uses the dependence on the mass (m) of the characteristic period of oscillation (τ) of an harmonic oscillator [74,75]:

$$\tau = 2\pi\sqrt{\frac{m}{k}} \tag{3.27}$$

where k is the spring constant. If a liquid of density ρ is introduced inside a tube of volume V, equation 3.27 can be rewritten as:

$$\tau^2 = 4\pi^2 \frac{m_t + m_l}{k} = 4\pi^2 \frac{m_t + \rho \cdot V}{k} \tag{3.28}$$

where m_t and m_l represent the masses of the tube and the liquid respectively. Therefore, the density of a liquid can be calculated by measuring the period of oscillation of a vibrating tube as:

$$\rho = \frac{k}{4\pi^2 V}\tau^2 - \frac{m_t}{V} \tag{3.29}$$

As in sound velocity measurements, the equation used includes some corrections for the temperature, viscosity and non-linearity effects and, consequently, it is also necessary to perform a calibration with water and dry air at different temperatures.

In this thesis we demonstrate that an analysis of the density, the sound velocity and, particularly, the adiabatic compressibility can be really useful to detect and understand the formation of cooperative structures within the characteristic H-bond network of water [72, 73].

3.5 Viscosity

One of the main conclusions of this thesis, is the formation of supramolecular structures in water solutions of tetrabutylammonium bromide [73]. For a proper analysis of these results, it is required a study of the viscosity (η) of the solutions, at different concentrations. These measurements were performed using the commercial rotational viscometer Anton Paar SVM 3000 Stabinger Viscometer from the NaFoMat Group (USC).

The system is a variation of the Couette-type viscometer [76, 77], in which the liquid is placed between two concentric cylinders of radius R_1 and R_2 ($R_2 > R_1$, see Figure 3.9). The outer cylinder rotates at a constant angular velocity (Ω_2) and transmits the rotation to the inner cup, which rotates at a certain angular velocity Ω_1 depending on the viscosity of the liquid (η).

The fluid velocity v can be obtained by solving the Navier-Stokes equation in cylindrical coordinates with z along the axis of the cylinders [78]:

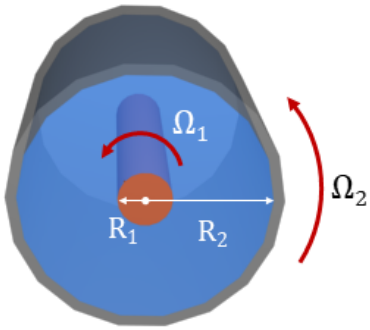

Figure 3.9: Scheme of a rotational viscometer. The liquid sample is placed between the two cylinders.

$$\frac{d^2v}{dr^2} + \frac{1}{r}\frac{dv}{dr} - \frac{v}{r^2} = 0 \tag{3.30}$$

whose solution is:

$$v = ar + \frac{b}{r} \tag{3.31}$$

where a and b are constants. By applying the boundary conditions at $r = R_1$ ($v = R_1\Omega_1$) and $r = R_2$ ($v = R_2\Omega_2$), the fluid velocity can be rewritten as follows:

$$v = \frac{\Omega_2 R_2^2 - \Omega_1 R_1^2}{R_2^2 - R_1^2} r + \frac{(\Omega_1 - \Omega_2) R_1^2 R_2^2}{R_2^2 - R_1^2} \frac{1}{r} \tag{3.32}$$

Finally, the driving torque associated to this movement is:

$$M_1 = R_1 \eta \left(\frac{\partial v}{\partial r} - \frac{v}{r} \right)_{r=R_1} = \frac{2\eta(\Omega_2 - \Omega_1) R_1 R_2^2}{R_2^2 - R_1^2} \tag{3.33}$$

Therefore, measuring the torque induced to the inner cylinder provides an accurate measurement of the viscosity.

The variation for this method used in the Anton Paar SVM 3000 Stabinger Viscometer includes a magnet inside the inner cylinder and

measures the eddy currents generated by the movement of the magnet. From the frequency of the AC current we can obtain the velocity of the inner cylinder. Moreover, the torque generated by this magnet (M_B) is proportional to its angular velocity and must be equal to M_1:

$$M_B = \beta\Omega_1 = \frac{2\eta(\Omega_2 - \Omega_1)R_1R_2^2}{R_2^2 - R_1^2} \tag{3.34}$$

where β is the proportionality constant which is determined by a previous calibration of the system. Then, the viscosity of the liquid can be obtained as follows:

$$\eta = \frac{\beta\Omega_1(R_2^2 - R_1^2)}{2(\Omega_2 - \Omega_1)R_1R_2^2} \tag{3.35}$$

The diffusion of a molecule within a liquid (D) decreases as its hydrodynamic radius (r_h) and the viscosity of the liquid increase. This relation is given by the Stokes-Einstein equation, which can be expressed as follows:

$$D = \frac{k_BT}{6\pi\eta r_h} \tag{3.36}$$

Therefore, the study of the viscosity is fundamental in order to identify if a decrease in the diffusivity is produced by an increase in the viscosity or by the formation of supramolecular structures, which increases the effective hydrodynamic radius. Using a combination of Nuclear Magnetic Resonance (NMR) with viscosity measurements, we have demonstrated the presence of clathrate like structures in aqueous solutions of tetrabutylammonium bromide, as we will discuss in more detail the corresponding chapter [73].

4. Heat transport in alcohol-water solutions

Many of the anomalous physicochemical properties of liquid water, that make it such a special liquid, are linked to the formation of a dynamic, close to tetrahedral, long-range supramolecular network, through cooperative hydrogen bonding [36, 79].

Solutes, polar and non-polar, disturb this network in different ways, changing dramatically the properties of the solution with respect to pure water. For instance, in 1987 Hofmeister observed a trend on the solubility of proteins in water under the influence of different ions, which has important consequences in biological systems [80, 81]. He suggested that chaotrope ions, also called "structure breakers", disrupt the tetrahedral structure of liquid water, and lead to a high solubility of proteins. On the other hand, kosmotrope ions, or "structure makers", promote the formation of a stable H-bond network and, consequently, reduce the solubility of proteins [82] (see Figure 4.1).

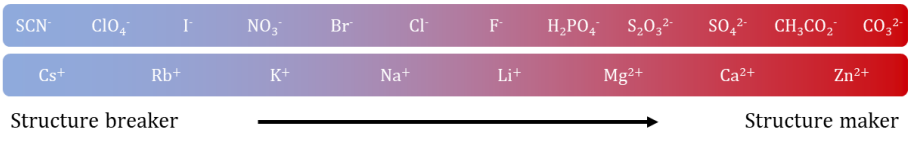

Figure 4.1: Hofmeister series for different anions and cations. The classification are performed according to the data reported on [69] and [82].

Dissolving organic molecules, with their hydrophobic chains, has a profound effect in the H-bond network of water around them, which affects the thermodynamic properties of the solutions [83]. For instance, water solutions of ethanol show an anomaly in the excess of molar enthalpy and sound velocity, and the partial molar volume shows a deep minimum at low concentrations of this solute [84, 85] (see Figure 4.2).

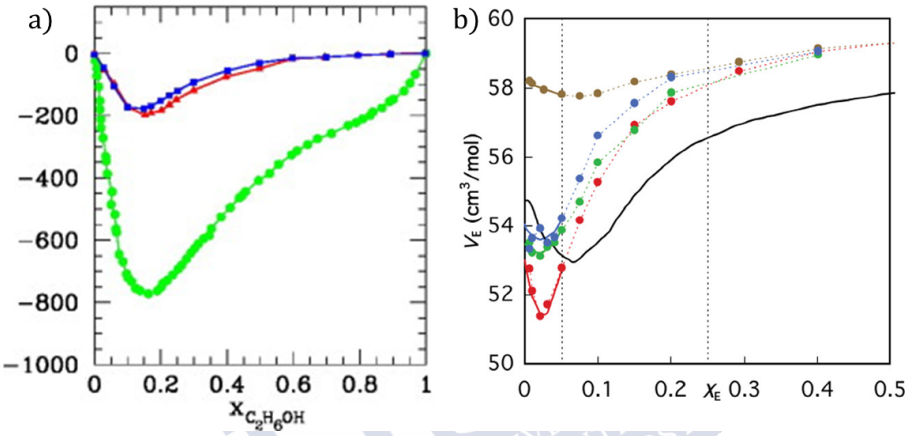

Figure 4.2: a) Excess of ultrasonic speed (blue), hypersonic speed (red), and molar enthalpy (green) as function of the mole fraction of ethanol at 293.15 K. Reprinted from [84] with permission of Elsevier. b) Partial molar volumes of ethanol as a function of ethanol mole fraction. Reprinted from [85], with the permission of AIP Publishing.

In systems with even larger concentrations of solutes, like living cells, Tros et al. [86] reported important changes in the rotational dynamics of water due to a disturbance of the hydrogen bond supramolecular network [87] (see Figure 4.3).

Frank and Evans suggested that all these effects are the consequence of a structuring of water molecules around the solutes, particularly around hydrophobic tails, in an ice-like structure, what has become to be called ”the iceberg model” [88]. In this model, solutes do not affect the bulk water properties beyond the first/second hydration shell [82].

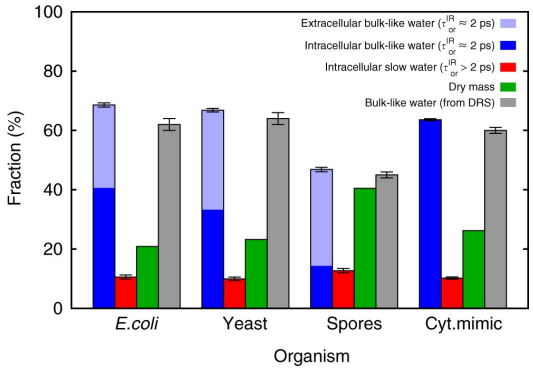

Figure 4.3: Fractions of water with different rotational dynamics in different organisms. Despite the majority of water shows bulk-like dynamics, an approximately 10% of water molecules are affected by the presence of the different types of solutes. Reproduced from [86] under a Creative Commons Attribution 4.0 International License.

However, most studies about the influence of different solvents on the structure of water are based on local spectroscopy [89–104] or molecular dynamics (MD) simulations [84, 85, 105, 106], which do not probe the effect of solutes on the tetrahedral bond network beyond the first/second hidration shell [107].

However, bulk neutron diffraction data suggest an incomplete mixing at molecular level, at least at high alcohol concentrations [89]. In the case of ethanol, it was reported the formation of ordered pockets of ethanol and water within a disordered liquid, also supported by MD simulations [84]. Moreover, recent analysis of the the bend+libration IR combination band, which reflects the collective dynamics of the H-bond network of water [93], points towards a change of the bulk structure of water under the influence of different ions, beyond the inmediate hydration shells of the solute [69]. All these results contradict the iceberg picture, and show the strong controversy of the effect of the presence of organic and inorganic molecules in the bulk structure of water.

Small alcohols are particularly suitable for solving this type of controversies: they have a hydrophilic head that may form H-bonds with

water, and a hydrophobic tail whose lenght can be changed at will to increase the effect of hydrophobic interaction.

Molecular dynamics simulations proposed a very complex scenario for ethanol-water solutions, with three differentiated regimes as a function of the concentration, each one showing a particular microstructural arrangement of the water molecules [85, 105] (see Figure 4.4).

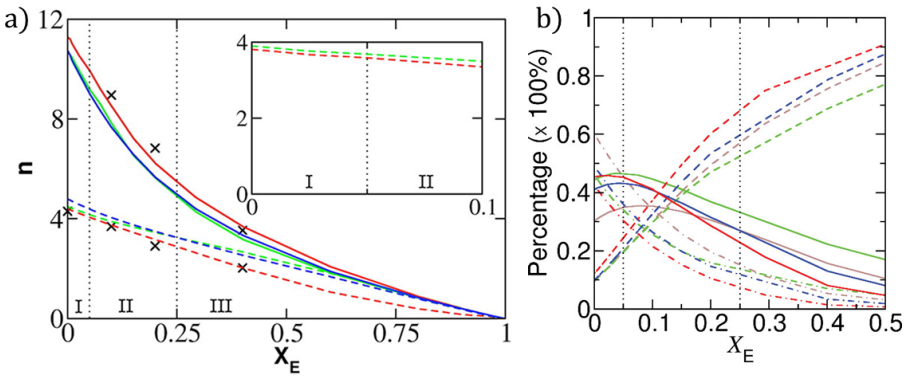

Figure 4.4: a) Coordination numbers of the hydration shell for the three regimes distinguished, obtained using different force fields (different colours) and by neutron diffraction experiments (x). Solid and dashed lines represent de C_2-O and O-O bonds respectively. Reproduced with permission from [105]. Copyright (2013) American Chemical Society. b) Percentage of water molecules with different numbers of nearest neighbor water molecules: five neighbors (dot dash), four (solid) and one to three (dash). Different colors represent the different force fields used in the simulations. Reprinted from [85], with the permission of AIP Publishing.

In regime I, they predicted the formation of densely packed hydration shells around each alcohol molecule. These hydration spheres come into contact in regime II, where alcohol-alcohol H-bonds start to form. Above $\chi = 0.25$, they recover the incomplete mixing accepted for the high concentration range [84]. These predictions are partially supported by mass spectroscopy analysis [96, 97]. Spectroscopic techniques confirm that, despite there is a strengthening in the H-bonds

around small hydrophobic groups, the structure does not differ much from bulk water [90, 91].

In this chapter we will try to shed light on all this controversy, through an analysis of the thermal conductivity of water solutions of different alcohols. As we discussed in the Introduction of this thesis, thermal conductivity is highly sensitive to dynamic changes on a time-scale that could be sensitive to the effect of different solutes on the long-range cooperative H-bond network of water. However, only few works analyzing the transport of heat in such solutions can be found in the literature [108–115], and none of them attempted to correlate their results with the molecular structure of water.

In the following we report a systematic analysis of the thermal conductivity and thermal diffusivity of alcohol-water solutions, correlating our results with spectroscopic and other thermodynamic data, like density, sound velocity or adiabatic compressibility. Part of the results and analysis discussed in this chapter are published in Ref. [72].

4.1 Hydrophobic solvation in alcohols

As we have discussed previously, the details of hydrophobic solvation in the cooperative H-bond network of water is still under discussion. In this regard, alcohols are ideal systems to elucidate the origin of the several anomalies observed, as we can perform systematic studies, varying easily the size and shape of the hydrophobic part of the molecule.

We performed accurate thermal conductivity measurements of water-alcohol mixtures at small concentration, combined with FTIR spectroscopy, adiabatic compressibility and DSC analysis. We compare the results between ethanol and 1-propanol, in order to study the effect of the alkyl chain length. We also include measurements of 2-propanol solutions to analyze the influence of the shape. Finally, we study the contribution of the OH part, by changing the hydrophilic group.

4.1.1 Water-Ethanol mixtures

Different groups reported several anomalies in the physicochemical properties of aqueous solutions of small alcohols, particularly in water-ethanol mixtures, at low concentrations [84, 85, 90, 91, 96, 97, 105, 106].

First, we analyzed the IR libration+bend combination band, which is highly sensitive to changes on the cooperative structure of water [69, 93], as we mentioned before. The results are shown in Figure 4.5 for different concentrations of ethanol. From the evolution of the frequency with the molar fraction of ethanol, we can distinguish three regions: firstly, the frequency increases fast up to $\chi \approx 0.025$ (I); then, the increase is slowed down for $0.025 \lesssim \chi \lesssim 0.1$ (II) and, finally, it is approximately constant for $\chi \gtrsim 0.10$ (III). These results are in good agreement with the concentration boundaries observed by mass spectroscopy [96, 97], Raman [116] and X-Ray Compton Scattering [117] experiments, and with MD calculations [85, 105, 106].

The bluehift of the libration band suggests a continuous increase in the strength of the intermolecular H-bonds. This behavior is compatible with two scenarios: a simple formation of strong water-ethanol and ethanol-ethanol H-bonds, which increases the mean frequency of the band, or a cooperative rearrangement of the tetrahedral network of water.

It is expected that heat transport is affected in both scenarios differently, as the thermal conductivity and diffusivity are highly sensitive to changes on the molecular order. Therefore, the study of the heat diffusion could help, in principle, to determine the mechanism of solvation in alcohol-water mixtures.

There are some works where their authors tried to model the thermal conductivity of a liquid mixture, by introducing several experimental parameters in more or less complex models [115, 118]. Here, we will start by using a very simple binary solution model, which fits nicely the experimental results for different mixtures.

Thermal conductivity depends on the type and strength of the interactions between molecules. Consequently, κ would depend on the probability of occurrence of each interaction. In a simple mixture of two

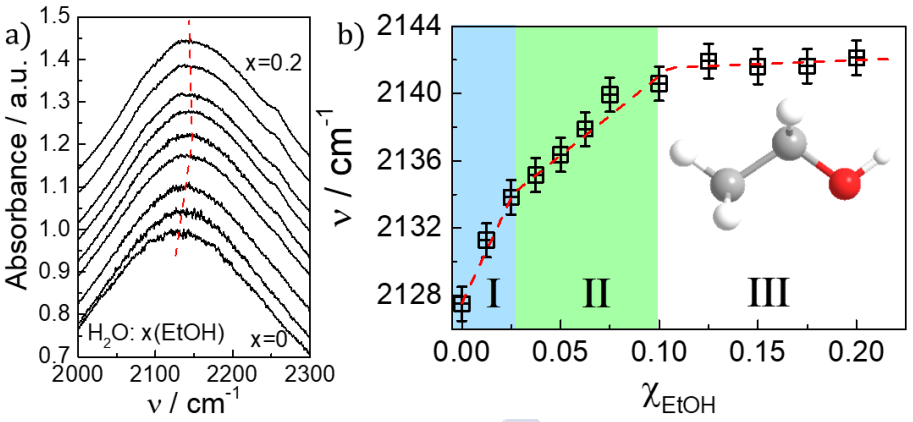

Figure 4.5: a) Room temperature IR absorption associated to the bend+libration combination band for ethanol, for different solutions with an increasing concentration of alcohol. b) Dependence of the frequency at the maximum absorption with the molar fraction of ethanol. The regimes suggested by the different slopes are highlighted. The value at each concentration and the error bars were calculated by the average and its standard deviation of the values obtained from five fits, selecting different range of data.

liquids, without structure rearrangement, the number of different intermolecular interactions is three: H_2O-H_2O, H_2O-EtOH and EtOH-EtOH (see Figure 4.6.a).

Although the empirical relations proposed by other groups usually use molar or mass fractions to weight the contribution of each type of interaction [115], it is more plausible that the probability of the interaction depends on the volume occupied by each molecule, as the probability of being in the close vicinity of another molecule increases with the size of the molecule. Therefore, in a first approximation, we can suppose that the thermal conductivity of a water-alcohol mixture can be modeled by an average of the κ of each component, weighted by their volume fractions, ϕ:

$$\kappa^2 = \underbrace{(\kappa_{H_2O} \cdot \phi_{H_2O})^2}_{\text{water-water}} + \underbrace{(\kappa_{H_2O} \cdot \phi_{H_2O})(\kappa_{OH} \cdot \phi_{OH})}_{\text{water-alcohol}} + \underbrace{(\kappa_{OH} \cdot \phi_{OH})^2}_{\text{alcohol-alcohol}} \quad (4.1)$$

Considering that $\phi_{H_2O} = 1 - \phi_{OH} = 1 - \phi$, the average thermal conductivity can be rewritten as:

$$\kappa = \sqrt{\kappa_{H_2O}^2 \cdot (1-\phi)^2 + \kappa_{H_2O} \cdot (1-\phi) \cdot \kappa_{OH} \cdot \phi + \kappa_{OH}^2 \cdot \phi^2} \quad (4.2)$$

As we show in Figure 4.6, this model nicely fits the experimental thermal conductivity values reported for several mixtures, and particularly those by R. Yano et al. [112] for water-ethanol solutions. However, there is not thermal conductivity data for molar fractions lower than $\chi = 0.1$.

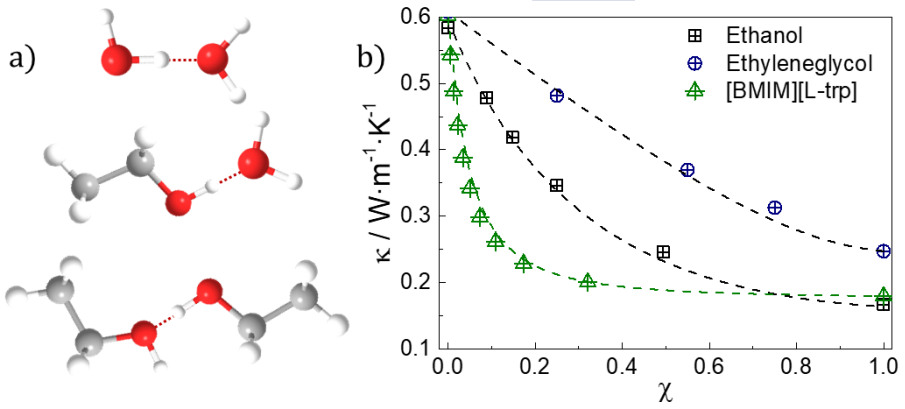

Figure 4.6: a) Possible interactions in a simple water-ethanol mixture model. b) Comparison of the thermal conductivity data for aqueous solutions of ethanol [112], etyleneglycol [119] and 1-Butyl-3-methylimidazolium L-Tryptophan ([BMIM][L-trp]) [120], and the prediction of the binary solution model proposed in equation 4.2 (dashed lines).

We measured the thermal conductivity (κ) and the diffusivity, calculated from the heat capacity and the density $\left(\alpha = \kappa \cdot \rho^{-1} \cdot C_p^{-1}\right)$, for aqueous solutions of ethanol at low concentrations (see Figure 4.7). The results obtained confirm the presence of the three regimes deduced in the IR spectra. The values for $\chi > 0.1$ are in accordance with those reported in literature [112].

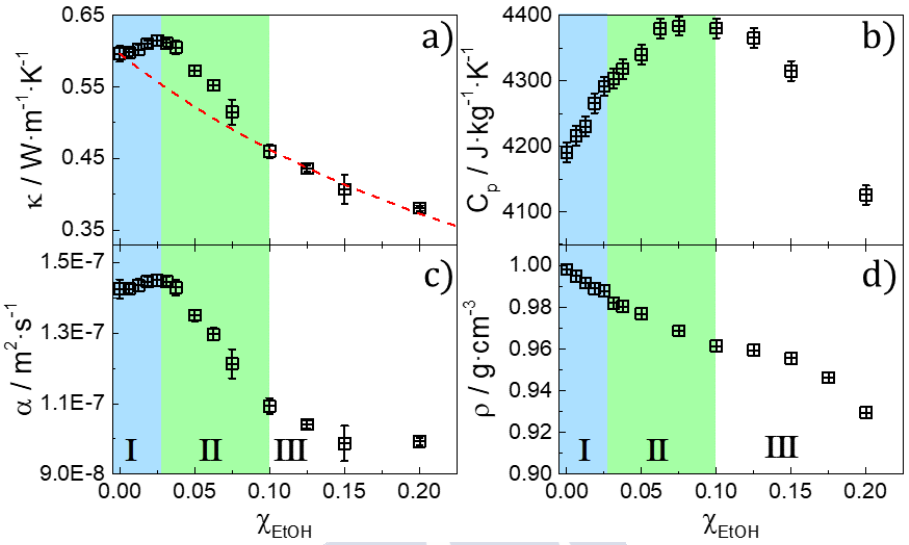

Figure 4.7: a) Thermal conductivity, b) heat capacity, c) thermal diffusivity and d) density, for water solutions of ethanol, at different concentrations. The red dashed line in a) represents thermal conductivity according to the binary solution model. The uncertainty of κ, $s(\kappa)$, was calculated by the standard deviation of three independent measurements; $s(C_p)$ was calculated by a propagation of the uncertainty from the error in the heat flow measured; $s(\rho)$ was estimated from a square distribution of the accuracy of the instrument, and is $2.9 \cdot 10^{-7}$ g·cm^{-3}; and $s(\alpha)$ was calculated by propagation of error.

Surprisingly, there is an increase in κ and α in Regime I, reaching a maximum of $\sim 3\%$ and $\sim 2\%$ at $\chi \approx 0.025$, respectively. Note that, despite this enhancement is not quantitatively very large, it is qualitatively relevant, as the formation of a cooperative H-bond network is responsible for the highest κ of water among liquids (except liquid metals, like Hg).

Dissolving "structure maker" ions, which produce an strengthening on the H-bond structure, invariably results in a decrease of the thermal conductivity (see Figure 4.8) [113, 114]. Therefore, the increase of κ observed in Region I, can not be produced by a simple strength-

ening of the tetrahedral network of bulk water, but it must be a consequence of a rearrangement of the water molecules around the alcohol; the life-time of these structures would be on a time-scale similar to thermal diffusion ($10^{-7}\ \mathrm{m^2 \cdot s^{-1}}$).

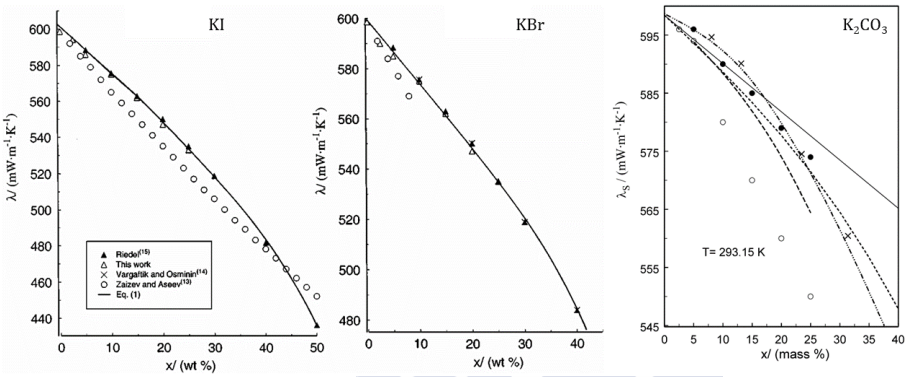

Figure 4.8: Thermal conductivity as a function of the concentration for different aqueous solutions. Reprinted by permission from Springer from [114] and [113]. Copyright (2001) and (2009).

Above $\chi \approx 0.025$, both κ and α decrease with the concentration. However, until $\chi \approx 0.1$ (Region II), the thermal conductivity is still higher than those predicted by the binary solution model. Increasing further the concentration, the experimental values of κ follows nicely the binary solution model discussed before (Region III).

These results are in very good agreement with the three regimes observed in mass spectroscopy [96,97], Raman [116] and X-Ray Compton Scattering [117] experiments. MD calculations [85, 105, 106] predicted the formation of densely packed hydration shells at low concentrations, with an enhanced and stronger tetrahedral order.

Tan et al. [105] predicted that these structures come into contact at $\chi \approx 0.05$. Above this concentration, they claim that the hydration shells start to break, which explains the progressive reduction of the thermal conductivity observed in Region II. However, in a more recent work they showed a maximum number of water molecules with four water

neighbors at $\chi \approx 0.025$ [85] (see Figure 4.4), in accordance with the maximum in κ observed in our work.

Furthermore, Raman spectroscopy experiments carried out by Davis et al. [121], estimated a number of ~ 36 water molecules in the first hydration shell of ethanol. Using this number, the boundary between Regions I and II would be at $\chi \approx 0.028$, similar to the concentration with the maximum thermal conductivity.

According to MD-simulations [105], the alkyl chains start to associate in Region II, which explain the continuous increase of the characteristic frequency of the libration band. This strengthening does not imply an enhancement on the tetrahedral order and, consequently, κ and α decrease. Above $\chi \approx 0.1$ (Region III), these superstructures are completely broken, recovering a simple mixture with a thermal conductivity following the binary solution model.

From a thermodynamic point of view, the formation of rigid hydration shells reduces the mobility of the water molecules around the alcohols [122]. This slowdown on the molecular dynamics leads to a reduction of the internal energy (U), as the number of degrees of freedom activated at room temperature decreases.

On the other hand, several studies reported an expansion of the tetrahedral network of liquid water, produced by the presence of hydrophobic molecules [85, 105, 123]. Both effects may influence the change of enthalpy upon crystallization/fusion at constant pressure ΔH, as this magnitude contains the information about the change in the internal energy (ΔU) and the volume expansion/contraction (ΔV):

$$\Delta H = \Delta U - P\Delta V \tag{4.3}$$

We performed DSC measurements to study the heat released during the melting of ice of the different solutions. In Figure 4.9.c we plot the enthalpy of fusion of the ice (ΔH_f) as a function of the ethanol concentration. In a simple binary solution model, it is expected that each ethanol molecule breaks a constant number of water-water H-bonds, leading to a monotonic reduction of the amount of ice formed and, consequently, a linear decrease of ΔH_f.

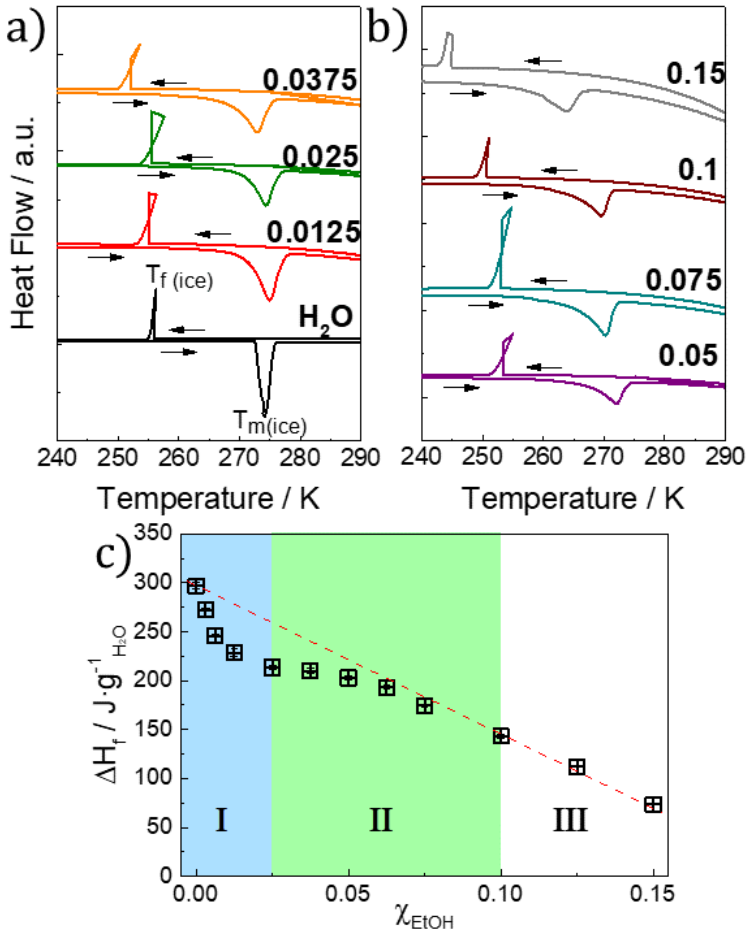

Figure 4.9: a-b) DSC thermograms for alcohol water mixtures at different concentrations. c) Dependence of the enthalpy of fusion of ice with the concentration of ethanol. The value of ΔH obtained was corrected by the actual mass of water in the mixture. The dashed line is the expected behavior in a simple binary mixture solution. The error bars were calculated by integrating five times the fusion peak obtained, using different data ranges.

In regions I and II there is a deviation from the expected trend, which has its maximum difference at $\chi \approx 0.025$, exactly the boundary

between regions I and II. Above $\chi \approx 0.1$, the values of ΔH_f recover the expected behavior.

From the difference between actual and expected values of ΔH_f, we can estimate the effective number of water molecules which are forming part of the rigid hydration shell and, consequently, do not contribute to the formation of ice (in the regular structure of pure water ice). This number is ≈ 22 for $\chi = 0.01$, i.e. around 11 per methyl group, similar to the value predicted in MD-simulations [105]. These thermodynamic considerations thus suggest the formation of rigid structures at low concentration of ethanol, with structures different to bulk water, as it was suggested by thermal conductivity measurements.

Adiabatic compressibility (K) is also a probe of the stability of the cooperative structure of bulk water. The stability of the tetrahedral network decreases as the temperature increases, leading to a minimum on K at $T_{\text{min}} \approx 60$ °C [124, 125]. This minimum separates two different regimes: one dominated by structural fluctuations of the tetrahedral network ($T < T_{\text{min}}$), and another one dominated by thermal fluctuations, as in simple molecular liquids ($T > T_{\text{min}}$) [126]. Therefore, changes on the cooperative tetrahedral network should, in principle, affect both the magnitude and temperature dependence of K.

To calculate the adiabatic compressibility $K = \rho^{-1} \cdot v_s^{-2}$, we measured the density and the sound velocity, from 10 °C to 66 °C, for ethanol-water mixtures (see Figure 4.10).

Density does not show a clear transition between regions I and II (see Figure 4.7.d), and this transition is also barely observable in sound velocity. At $\chi \sim 0.1$ (transition between region II-to-III) there is a maximum in the v_s, followed by a fast decrease, compatible with a rapid breakdown of the structures formed at low concentration.

The position of T_{min}, the curvature around the minimum, and the change of K with temperature in region I do not differ much than the values of bulk water (see Figure 4.11.d). Thus, the formation of the supramolecular structures characteristic of this low-concentration regime does not affect too much the mechanical properties of the cooperative network of H-bonds.

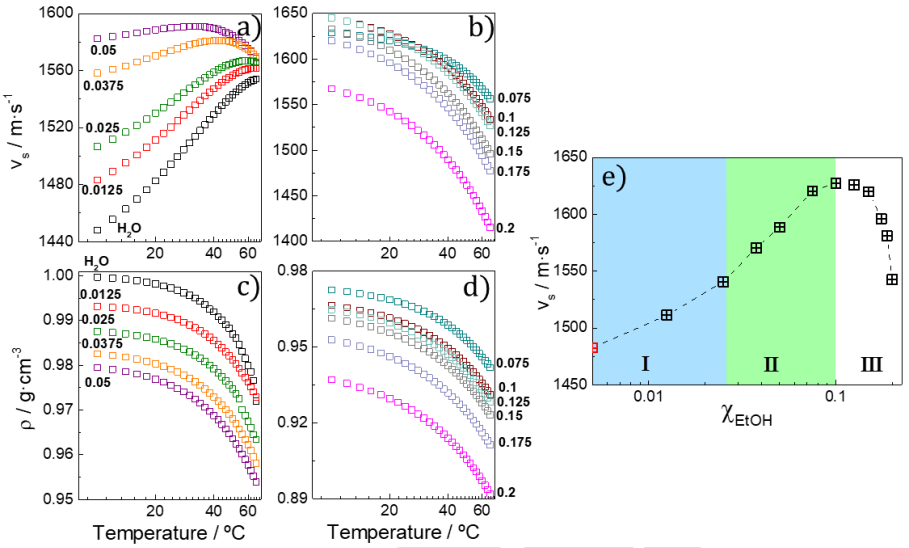

Figure 4.10: Dependence of the sound velocity a-b) and density c-d) with temperature for different ethanol-water mixtures. e) Dependence of the sound velocity with the molar fraction of ethanol at $T = 20$ ºC. The red square indicates the value for pure water. The uncertainty was calculated supposing a square distribution of error of the accuracy of the instrument, and is $2.9 \cdot 10^{-3}$ m·s^{-1}.

Increasing the concentration of EtOH leads to a rapid decrease of K and T_{min} in Region II. The minimum becomes shallower and the slope of $K(T)$ at room temperature increases rapidly, reaching the positive value characteristic of common liquids above $\chi \approx 0.05$. This suggests a rapid breakdown of the supramolecular structures at low concentrations.

At the boundary between regions II and III, the compressibility shows a minimum. Increasing further the concentration results in a fast increase of K, compatible with a simple binary mixture model, as the compressibility of pure ethanol ($K_{\text{EtOH}} = 0.585$ GPa^{-1}) is higher than pure water [127].

The boundaries between the three regimes match perfectly which those observed through thermal conductivity measurements. Thus, this

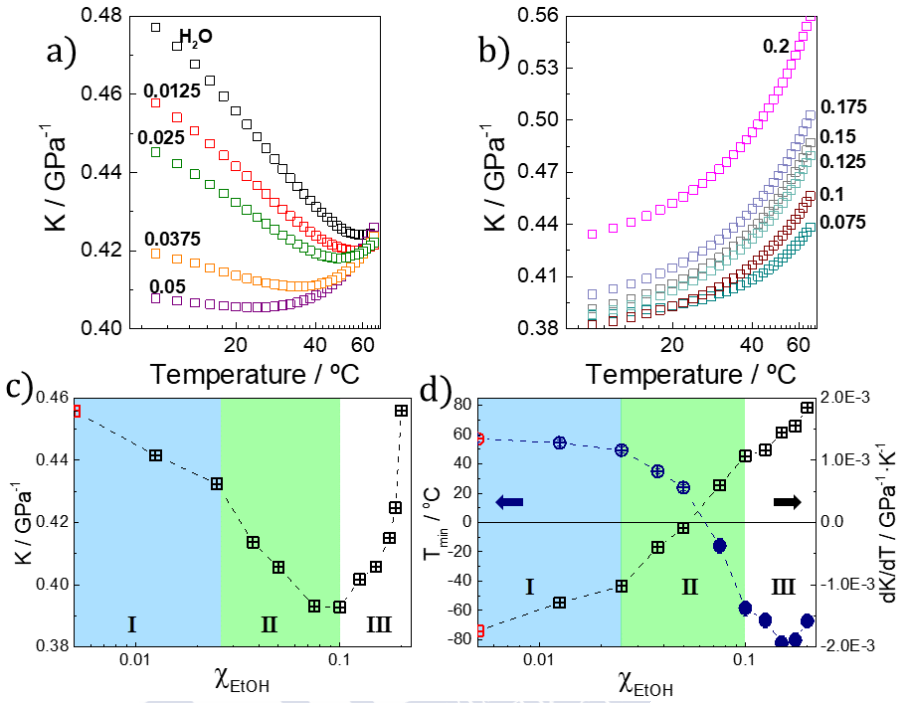

Figure 4.11: a-b) Dependence of the adiabatic compressibility on temperature for different ethanol-water mixtures. c) Dependence of K and d) dK/dT and $T_{\min}$ with the concentration of ethanol, at $T = 20$ °C. Red symbols indicate the value for pure water. For $\chi > 0.05$, the minimum of K is below the crystallization temperature, and out of the range of temperature of the measurement. The values of $T_{\min}$ for these concentrations were obtained by a parabolic extrapolation and represented with solid circles. The uncertainty of dK/dT was calculated by propagation of error and is 10^{-6} GPa^{-1}·K^{-1}.

analysis confirms the surprising result that the presence of ethanol may increase the rate of energy transfer (i.e. the thermal conductivity) between water molecules. This is most probably a general mechanism (not restricted to ethanol), which could enhance the communication among biomolecules, even at moderate-long distances, mediated by cooperative changes in the water molecules in between [128].

4.2 Effect of the size and shape of the alkyl chain

Once we demonstrate the importance of hydrophobic solvation on the cooperative structure of water, studying the effect of the size and shape of the alkyl chain is important to check the general valitidy of these observations. MD simulations show that the transition between regimes I and II in water-ethanol mixtures is produced by the coalescence of the hydration shells [105]; consequently, it is expected that an increase on the size of the alkyl chain of alcohol produces a displacement to lower concentrations of the boundaries between the different regimes.

Davis et al. [121] found a linear increase of the number of water molecules affected by the hydrophobic alkyl chain; they reported that 32 water molecules become affected by the interaction with methanol, and every CH_2 group adds another 4 water molecules to this hydrophobic hydration shell. Femtosecond IR spectroscopy experiments performed by Rezus et al. [122], also observed 4 water molecules around each CH_3 group presenting an anomalously long rotational relaxation time, although they only studied single carbon chains or closed rings.

To study the contribution of different size and shape of hydrophobic molecules, we followed the IR libration band of several aqueous solutions of 1-propanol and 2-propanol, which are represented in Figure 4.12. These isomers have the same number of carbons, but their distribution is different: while 1-propanol has a single alkyl chain with one terminal CH_3 group, 2-propanol has two small chains symmetrically distributed around the OH group, and consequently, two terminal CH_3 groups.

In Figure 4.13 we can see that the transition between regions I and II is not observed for 1-propanol, and it is barely observable in 2-propanol. The change in the slope at $\chi \approx 0.1$ probably reflects the transition between regions II and III, but the characteristic frequency continues increasing in Regime III, contrary to in ethanol-water mixtures.

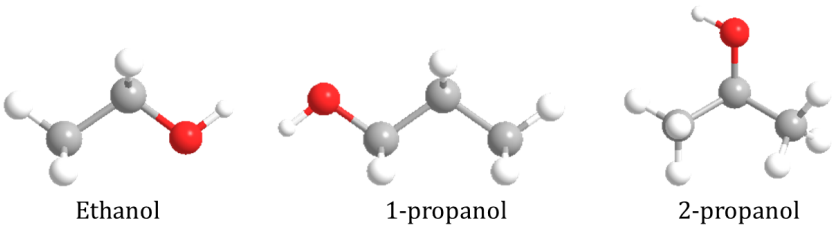

Figure 4.12: Scheme of the three alcohols studied in this work.

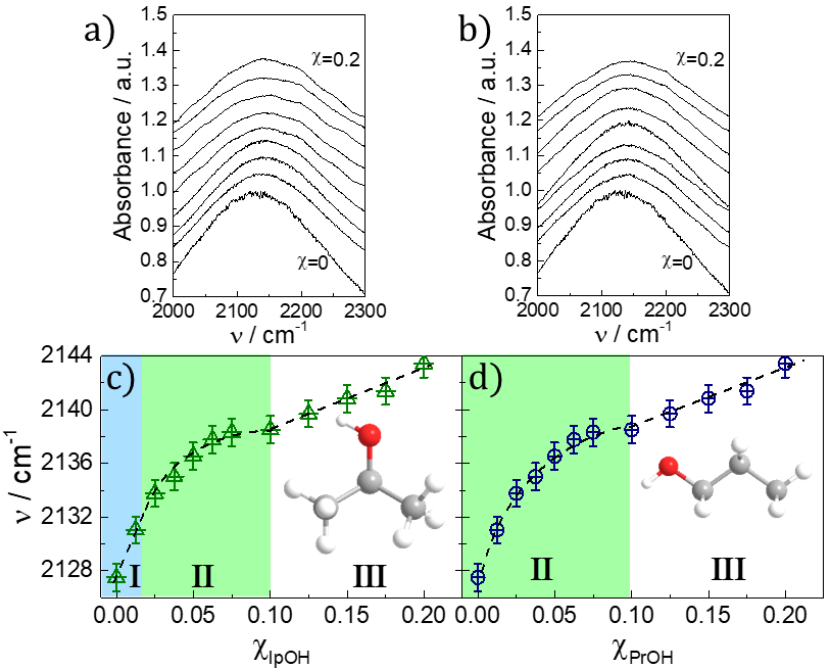

Figure 4.13: a-b) Room temperature IR absorption associated to the bend+libration combination band for 2-propanol (green) and 1-propanol (blue), respectively. c-d) Dependence with the molar fraction of the frequency at the maximum absorption. The dashed line is a guide to the eye. The error bar was calculated by the standard deviation of the values obtained for five fits, selecting different range of data.

As we discussed before, the presence of the -OH groups in alcohols induces the formation of hydrogen bonds, so it is difficult to determine the contribution to the average characteristic frequency. However, as we argued in the previous section, the thermal conductivity could allow us to determine the existence between different regimes as a function of the concentration of alcohol.

In Figure 4.14 we represent the thermal conductivity and diffusivity for both alcohols. The transition between regimes I and II is displaced to lower concentrations in isopropanol, while it disappears in 1-propanol. These results suggest that the longer alkyl chain in 1-propanol impedes the formation of the densely packed hydration shells and, consequently, it does not produce an enhancement on the rate of heat transfer.

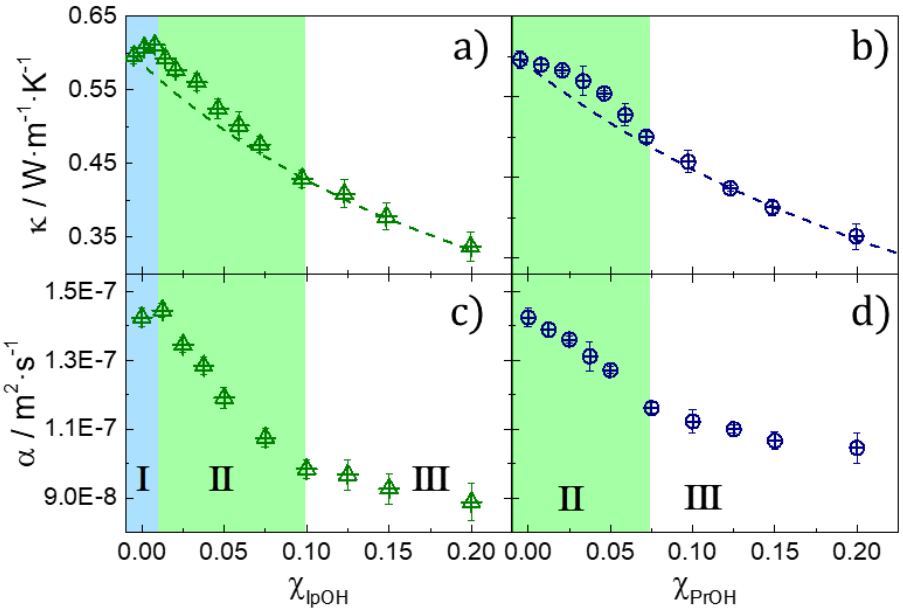

Figure 4.14: a-b) Room temperature thermal conductivity a-b) and thermal diffusivity c-d) for 2-propanol (green) and 1-propanol (blue), respectively. The red dashed line in a-b) represents thermal conductivity expected in a simple binary solution model. α was calculated from the density and heat capacity, which is represented in Figure 4.15.

The transition between regions II and III is also different in both isomers, contrary to what can be observed by IR analysis. The boundary between both regions in isopropanol is similar to ethanol, but is significantly displaced to lower concentrations in 1-propanol. It is worth noting that, even both isomers have the same number of carbon atoms in the chain, the behavior is completely different. The main difference between both isomers is the symmetry of the molecule.

In a very simple picture, isopropanol can be approximated to two ethyl groups sharing the center CH group. In this picture, the coalescence limit would be at half of the concentration observed in ethanol, as each isopropanol molecule contributes similar than two ethanol molecules. This is exactly what is observed in isopropanol-water mixtures, where the maximum of κ occurs at $\chi_{\text{max}} \approx 0.0125$, in comparison with a $\chi_{\text{max}} \approx 0.025$ in water-ethanol solutions.

Increasing the length of the hydrophobic chain suppresses the maximum in 1-propanol, but there is a higher than expected thermal conductivity up to $\chi \approx 0.075$. Probably, the hydration shells around the hydrophobic chain are larger for 1-propanol and, consequently, the system goes directly to Regime II even at very low concentrations.

Despite the structures formed in Regime II do not produce an enhancement of the heat transport, they have an effect on the structure and, consequently, on the heat capacity (see Figure 4.15). We observe the expected increase on the heat capacity, with a maximum at the transition between regimes II and III determined from κ, as in water-ethanol solutions.

Similar to what we did for water-ethanol mixtures, we measured the sound velocity and the adiabatic compressibility for the different aqueous solutions (see Figure 4.16). The results are in accordance with the heat capacity, showing a displacement of the maximum to lower concentrations. Moreover, the compressibility at the minimum for isopropanol is similar than the value obtained for ethanol, while it is not so pronounced in 1-propanol.

Rezus et al. [122] reported that the extension of the hydration shell depends only on the number of equivalent CH_3 groups. Under this hypothesis, the behavior of 1-propanol, with only one CH_3 group, would

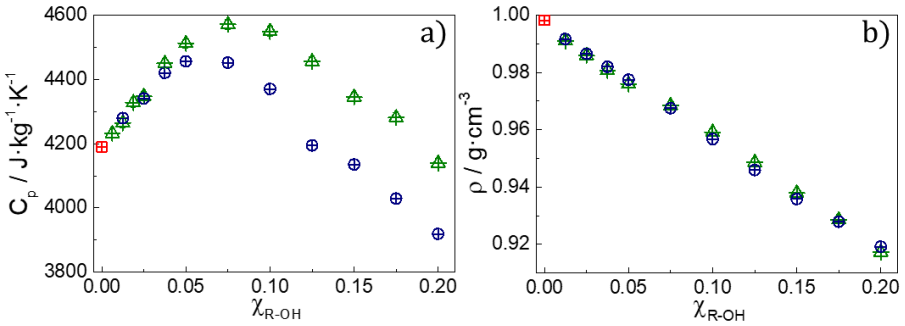

Figure 4.15: Heat capacity a) and density b) for aqueous solutions of 1-propanol (blue circles) and 2-propanol (green triangles) at different concentrations, at $T = 20$ °C . Red squares indicate the values of pure water.

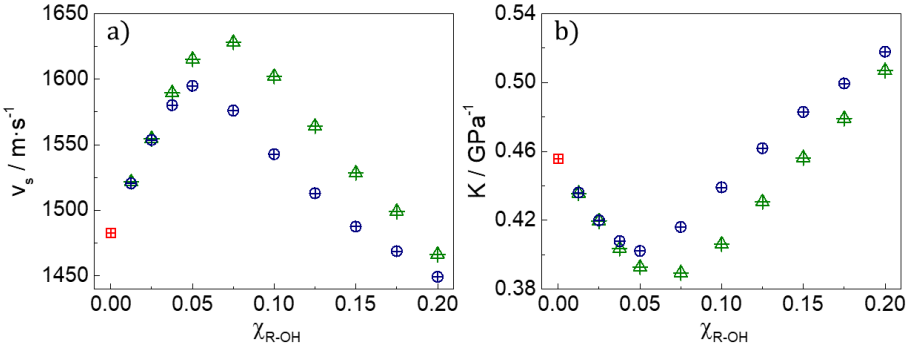

Figure 4.16: Sound velocity a) and adiabatic compressibility b) for aqueous solutions of 1-propanol (blue circles) and 2-propanol (green triangles) at different concentrations, at $T = 20$ °C. Red squares indicate the values of pure water.

be more similar to ethanol than for isopropanol, which has two CH_3. However, thermal conductivity and diffusivity measurements performed in this work show that longer hydrophobic chains impede the formation of coordinated structures at low concentrations.

Our results demonstrate that the shape and the symmetry of the molecules are fundamental parameters in order to determine the effect

of the hydrophobic solvation. We think that the increase on the velocity of energy transfer, and the cooperative rearrangement of the tetrahedral network of water, may be particularly relevant to understand biomolecular communication and recognition.

4.3 Contribution of the hydrophilic part

In the previous section we showed that increasing the size of the hydrophobic chain results in the suppression of the supramolecular structures formed at low concentrations of ethanol. However, the study of the contribution of the hydrophilic part is also necessary, in order to determine any contribution to this phenomenology.

In order to do that, we studied a series of molecules with different hydrophilic interactions, as it is showed in Figure 4.17. In these molecules, the oxygen has a double bond, or it is close to a positively charged nitrogen. Consequently, the ability of H-bond formation in this hydrophilic part is different in each of them.

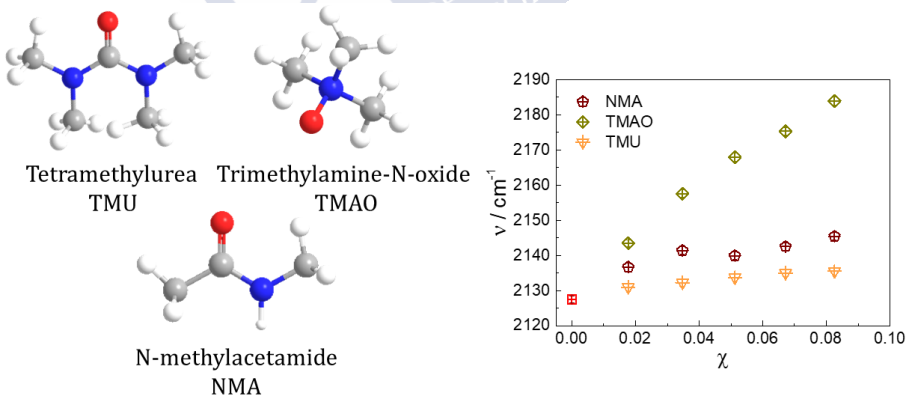

Figure 4.17: Scheme of the molecules studied; blue spheres represent nitrogen atoms. The graph presents the dependence of the room temperature IR absorption, associated to the bend+libration combination band, with the solute concentration. The red square indicates the value of pure water.

Dissolving these molecules produces a strengthening of the libration+bend combination band (see Figure 4.17). The increase of the characteristic frequency of this mode is similar than in alcohol-water solutions for NMA and TMU, but is much bigger in TMAO, probably caused by a protonation of the oxygen atom.

In Figure 4.18 we plot the results obtained in the study of the heat transport, similar than in previous sections. The data fit to the binary solution model even at low concentrations, demonstrating that the formation of ordered structures is not triggered by the ability of the polar group to form H-bonds with water. This hypothesis is also supported by the suppression of the maximum in the heat capacity, suggesting a

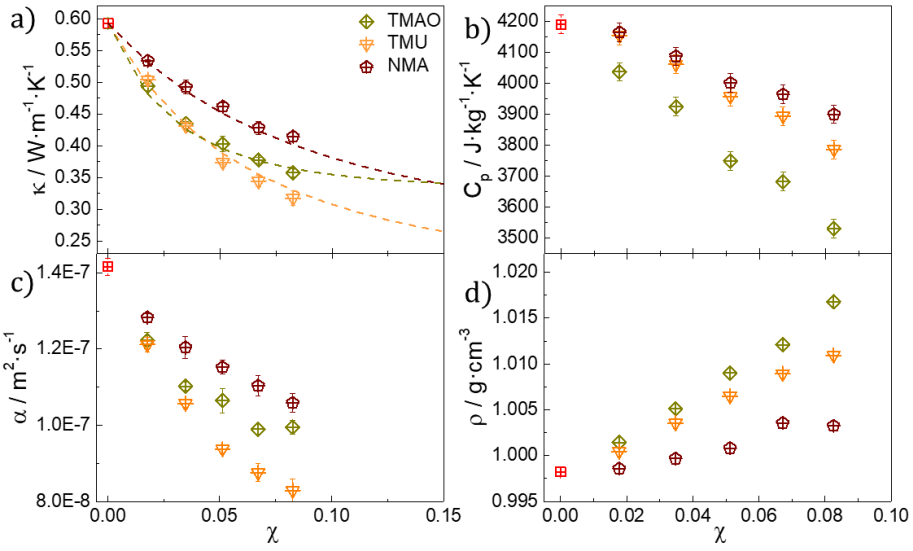

Figure 4.18: a) Thermal conductivity, b) heat capacity, c) thermal diffusivity and d) density of the three molecules studied, at $T = 20$ °C. The dashed lines in a) represent the binary solution model calculated using the κ of pure liquids (κ(TMU) $= 0.183(15)$ W·m^{-1}·K^{-1}; κ(NMA) $= 0.254(20)$ W·m^{-1}·K^{-1}). The value of κ for TMAO can not be measured, as it is solid, and was obtained from the fit (κ(TMAO) $= 0.337(10)$ W·m^{-1}·K^{-1}). Red squares indicate the values of pure water.

simple breaking of the tetrahedral network of bulk water as the concentration of solute increases.

Thus, the formation of supramolecular structures beyond the first hydration shell of the solute in alcohol-water solutions, must be a consequence of both hydrophilic and hydrophobic interactions. Despite hydrophobic chains are the main responsible of the arrangement of water molecules around alcohols [122], our results show the importance of the hydrophilic interaction to form enhanced structures.

To further support this picture, we also compare the sound velocity and adiabatic compressibility for these molecules with the results obtained in alcohols (see Figure 4.19). According to what is observed in heat transport measurements, these solutions do not show neither a maximum or a minimum in v_s and K, respectively.

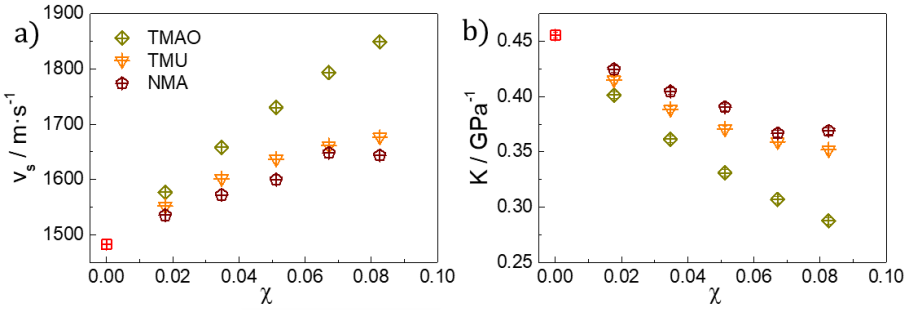

Figure 4.19: a) Sound velocity and b) adiabatic compressibility for water solutions of the different molecules studied, at $T = 20\,^{\circ}\mathrm{C}$. Red squares represent the values of pure water.

Thus, these results confirm the effect of the hydrophilic part into the solvation process. The incorporation of the OH group of alcohols into the water structure [129] leads to a completely different molecular arrangement, in spite of the similar hydrophobic interaction. In conclusion, the suppression of the OH group, or the presence of large hydrophobic groups, impedes an optimal accommodation into the cooperative structure of water and, consequently, reduces the energy transfer rate.

4.4 Hydrophobic solvation in the two-state water model

Several of the anomalies in the physicochemical properties of water, like density, adiabatic compressibility or heat capacity, are usually referred to a two-state water model [79]. This model, proposed in 1992 by Poole et al. [130], suggests that this rich phenomenology is related to a coexistence of water in two different structures, an extension of a first order transition between high density (HDA) and low density (LDA) amorphous ices to the liquid phase, as reported by Mishima et al. [131] (see Figure 4.20).

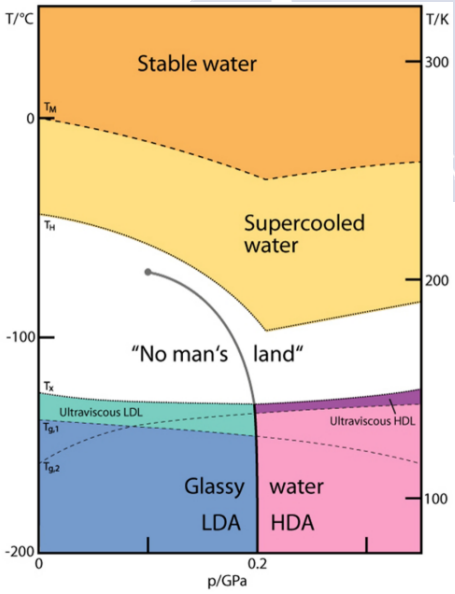

Figure 4.20: Phase diagram of non-crystalline water. Note that the liquid-to-liquid phase transition line is a continuation of the LDA-HDA line, which ends at the liquid-liquid critical point. Reproduced with permission from Gallo et al. [79]. Further permissions related to this material should be directed to the ACS.

Since this proposal, several groups have tried to access to this phase transition following different strategies, but the difficulty to prevent the fast ice crystallization at low temperatures, the so-called "no man's land", produces inconclusive attempts. For instance, decompression-induced melting of ice IV shows a discontinuity, compatible with a liquid-to-liquid phase transition, but the rapid crystallization of ice impedes an appropriate analysis of this transition [132].

One of the most used strategies is the addition of different solutes, at concentrations sufficiently high to impede the crystallization, but as low as possible to preserve the anomalies on its thermodynamic properties [133, 134]. Dissolving both hydrophilic and hydrophobic solutes results in a decrease of the crystallization temperature [135–138], which allows to access deeply into the supercooled region of water.

In 2012, Murata and Tanaka reported, for first time, the observation of a liquid-to-liquid phase transition in a water-glycerol mixture [50], confirming the two-state water model and allowing its characterization. Despite the absence of a macroscopic phase separation, Time-Resolved and 2D vibrational spectroscopy showed that this liquid-liquid transition is followed by the nucleation of ice, and consequently it is irreversible [139].

Recently, Woutersen et al. [140] reported similar results in an aqueous solution of hydrazinium trifluoroacetate at low concentration, avoiding completely the formation of ice. They performed MD simulations showing that the phases observed in this mixture have similar structures than those expected in bulk water. These results strongly support the two-state model for liquid water, which results in a coexistence of both structures, even at room temperature.

In support of this view, X-ray spectroscopy experiments [141–143] showed that $\approx$20-40% of water molecules are highly structured in a tetrahedral network (LDL), and a 60-80% present a locally distorted network (HDL), at room temperature.

If we look at the tetrahedral structure of low-density water, it resembles more a crystalline solid than a normal liquid. This open structure is a consequence of the accomodation of the coopeative H-bond network, and resembles the arrangement in ice, leading to the highest value of the

thermal conductivity among liquids, or the crystal-like dependence of κ with the temperature for the LDA [108, 109]. Thus, as a starting point, we could consider the distorted structure of HDL as a consequence of the presence of defects in the otherwise perfect tetrahedral structure of LDL; these distortions can be produced by the addition or elimination of one H-bond [144, 145].

The -OH group present in alcohols allows the incorporation to bulk water structure, affecting less to the cooperative network than other solutes, like ions [129]. The presence of the hydrophobic group creates a distortion on the tetrahedral H-bond network of water, which can be interpreted in terms of the coexistence of LDL and HDL.

MD simulations performed by Saito et al. [145] suggest that reducing the number of defects, by decreasing the temperature, produces a fragmentation of the low-structured clusters (see Figure 4.21). At high temperatures, close to room temperature, this fragmentation does not lead to an increasing number of locally distorted structures (LDS), but it induces the formation of new locally tetrahedral-structured clusters (LTS).

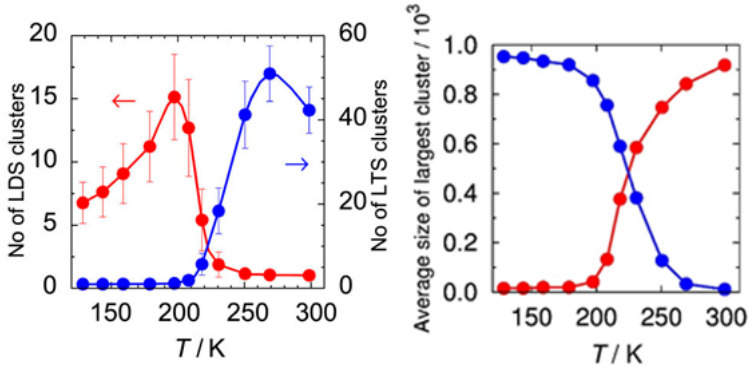

Figure 4.21: Number and size of clusters of locally tetrahedral-structured (blue) and locally distorted-structured (red) molecules. Adapted from [145], with the permission of AIP Publishing.

The incorporation of the water-like OH group of alcohols will be favored by an interaction with a water molecule with only three neighbors and, consequently, the number of defects is reduced. This reduction produces a displacement of the equilibrium between high-density and low-density water, which leads to an increase of the number of LTS clusters [146, 147]. This hypothesis is supported by MD simulations performed by Tan et al. [85], where they report an increasing number of four-neighbor water molecules at low ethanol concentrations (see Figure 4.4). The maximum increase will be reached at a concentration where the hydration shells are sufficiently large to affect significantly the LDS.

In principle, we could separate the system into a mixture of two different components, LDL and HDL, with a varying thermal conductivity and concentration. Then, the effective thermal conductivity of the mixture can be calculated as an average between a mixture of alcohol with LD water ($\kappa_{\text{LD-OH}}$) and with HD water ($\kappa_{\text{HD-OH}}$), weighted by the fraction of each component, as in the binary solution model discussed before:

$$\kappa = \lambda \cdot \kappa_{\text{LD-OH}} + (1 - \lambda) \cdot \kappa_{\text{HD-OH}} \tag{4.4}$$

where λ is the fraction of LD water. If we know the thermal conductivity of LD and HD water, we can calculate the fraction of each component at different ethanol concentrations, by measuring the thermal conductivity of the mixture.

Thermal conductivity of LD water (κ_{LD}) can be estimated as an extrapolation from the results of the low-density amorphous (LDA) water, supposing a small difference between liquid and glassy states, as it usually occurs [148–151]. Andersson et al. [108, 109] observed a crystal-like behavior of the LDA, following the T^{-1} trend of the Debye model. Thus, we can fit their data to a Debye type function, obtaining a value $\kappa_{\text{LD}} = 0.805 \pm 0.015\ \text{W}\cdot\text{m}^{-1}\cdot\text{K}^{-1}$ (see Figure 4.22).

For pure water ($\phi = 0$), equation 4.4 is simplified as follows:

$$\kappa_{\text{H}_2\text{O}} = \lambda_0 \cdot \kappa_{\text{LD}} + (1 - \lambda_0) \cdot \kappa_{\text{HD}} \tag{4.5}$$

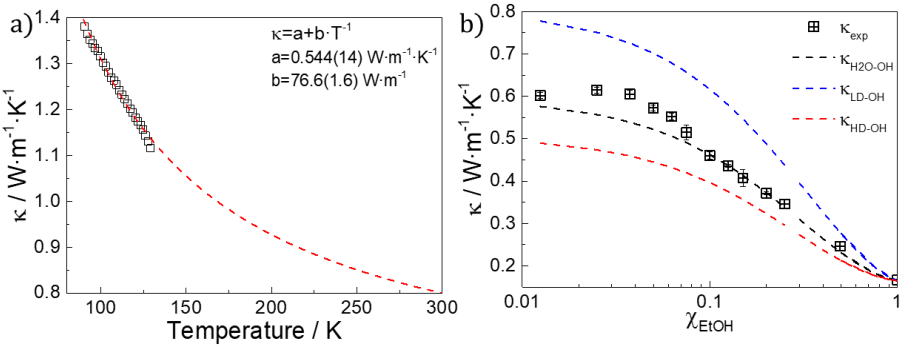

Figure 4.22: a) Thermal conductivity of LDA and fit to the Debye model. Experimental data was taken from the work of Andersson [109]. b) Comparison between the experimental thermal conductivity and the values predicted by the binary solution model of bulk, LD and HD water.

where λ_0 represents the fraction of LDL in bulk water. As we mentioned before, X-ray spectroscopy experiments [141–143] obtained a fraction of LD water between 20-40%. Therefore, the value of κ_{HD} can be calculated as follows:

$$\kappa_{\mathrm{HD}} = \frac{\kappa_{\mathrm{H_2O}} - \lambda_0 \cdot \kappa_{\mathrm{LD}}}{1 - \lambda_0} \tag{4.6}$$

which depends on the precise value of λ_0. Supposing a 30% of LDL, $\kappa_{\mathrm{HD}} = 0.506 \pm 0.017\ \mathrm{W \cdot m^{-1} \cdot K^{-1}}$.

Finally, using these values we can calculate the fraction of LD water λ at each ethanol concentration:

$$\lambda = \frac{\kappa - \kappa_{\mathrm{HD\text{-}OH}}}{\kappa_{\mathrm{LD\text{-}OH}} - \kappa_{\mathrm{HD\text{-}OH}}} \tag{4.7}$$

In Figure 4.23 we plot the fraction of HD and LD water for the different concentrations. We observe a maximum increase of $\sim 25\%$ of the LD phase for an ethanol-water mixture at $\chi \approx 0.025$, which is very similar to the change in the number of LTS clusters as temperature decreases (see Figure 4.21).

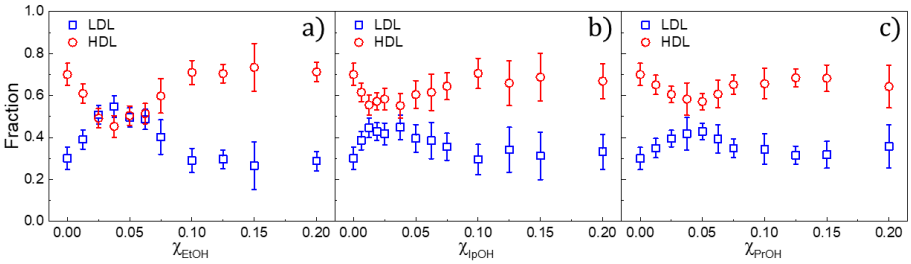

Figure 4.23: Fraction of HD and LD water as a function of the alcohol concentration, calculated from the difference between experimental thermal conductivity of ethanol, 2-propanol and 1-propanol aqueous mixtures and a binary solution model.

This analysis points towards a picture where the anomalous physicochemical properties of the water-alcohol mixtures can be intepreted in the scenario of the liquid-to-liquid phase transition of pure water. Our results demonstrate that the addition of alcohols, with a hydrophobic chain and a water-like OH group, can be interpreted as to produce a displacement of the equilibrium between LDL and HDL water, which results in an enhancement of the rate of energy transport across these systems.

4.5 Summary

In this chapter we have shown the effect of dissolving different solutes on the extensive structure of bulk water. We demonstrate that both hydrophobic and hydrophilic interactions play a role in the formation of ordered structures at low solute concentrations. In alcohols, these structures must have life-times of the same order of magnitude than the thermal diffusion time, so they are detectable through thermal conductivity experiments.

We also developed a very simple model which reproduces the experimental data for different aqueous mixtures, which can also be applied in the two-state water model. Importantly, adding small amounts

of ethanol results in an increase on the fraction of LDL water. Because this phase is more structured, it produces an increase in the thermal conductivity, i.e, of the rate of energy transfer.

Increasing the size of the hydrophobic groups results in a progressive suppression of this effect, as the alcohol can not be incorporated to the water structure without distorting the cooperative tetrahedral structure of water. Furthermore, changing the water-like OH group by another hydrophilic group changes the thermodynamic properties of bulk water as expected in a simple mixture.

Our study opens a new strategy to design liquids with specific molecular structures, by modifying the hydrophilic and hydrophobic interactions between the solute and the solvent. In the next chapter, we will show an example of how these effects can be used up to the point to create a new family of liquids.

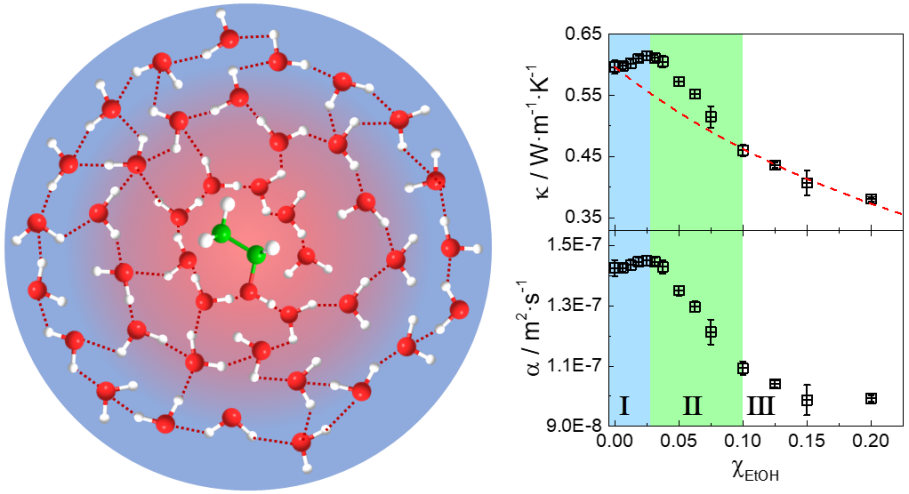

Figure 4.24: Graphical summary of the the main results of the chapter: the inclusion of ethanol in the tetrahedral network of water produces an increase of the rate of energy transfer, in a certain concentration window, probably due to a reconfiguration of the tetrahedral network of H-bond water molecules, well beyond the first hydration shell of the alcohol.

5. Molten Clathrates: a new family of supramolecular fluids

As discussed in the previous chapter, dissolving hydrophobic molecules in water leads to the formation of supramolecular structures, with different extentions and lifetimes, depending on the size, symmetry and hydrophobicity of the solute. Here, we discuss the effect of dissolving large and symmetric molecules based on the alkylammonium/phosphonium structure, showing a new phenomenology which could have applications in energy storage and conversion. The main results from this chapter were published in [73].

It is known that dissolving certain non-polar molecules may result in the formation of crystalline solids at low temperatures and/or high pressures, the so-called clathrate hydrates [152]. These structures coordinate a much higher number of water molecules than expected from a frozen "iceberg" derived from the hydrophobic solvation of an alcohol, for instance, as discussed in the previous chapter [88, 122]. As an example, while 4 molecules of water structure around each -CH_3 group of an alcohol, this number increases up to ~ 16 around methane in a liquid solution, or ~ 46 in its crystalline clathrate [152] (see Figure 5.1).

An important question regarding these crystalline clathrates is what happens above their melting temperature, in the liquid state: is the supramolecular structure maintained (in a short timescale) in the liquid? Do water molecules behave as bulk instead, except maybe within

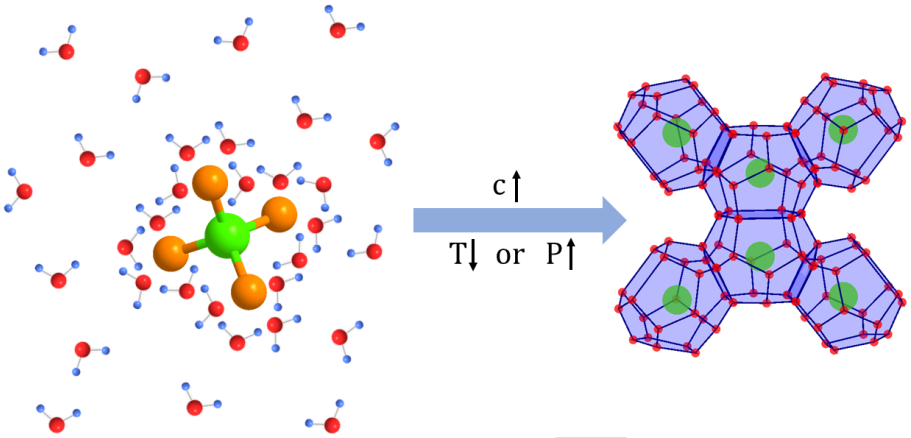

Figure 5.1: Scheme of the formation of clathrates in methane hydrates. Above a certain concentration, and at low temperature or high pressure, the simple hydrophobic solvation results in the formation of crystalline solid clathrates, where the methane (green) is enclosed by ~ 46 water molecules (red). The representation was performed according to the structure given in Ref. [152].

the first coordination shell? The dynamic supramolecular arrangement of water around these solutes should have an impact in the physicochemical properties of the solution, particularly on the heat transport, which, as discussed in the previous chapter, is a very sensitive probe to dynamic rearrangements of the cooperative structure of liquid water.

Quaternary ammonium salts induce the formation of similar cage structures, as methane, Ar, and other gases, but are much more easily handled [153,154]. Moreover, they crystallize at more accessible conditions, with crystallization temperatures/pressures close to room temperature [155–158]. Contrary to normal clathrate hydrates, part of the host molecule, the anion, is included into the structure of water, while the cation is enclosed by the cage. Consequently, these systems are usually referred as semi-clathrate hydrates. In many of them, due to symmetry constraints, packing is optimized when some of the cages are empty, and may host different additional molecules. For that reason, these systems find important applications in hydrogen storage, transportation or

gas separation [152, 155, 156, 159–164]. Particularly, storing methane or carbon dioxide inside these structures may suppose an important advance on the permafrost challenge, whose melting is beyond the explosions of gas in Siberia, and is a fundamental contribution to climate change [165].

One example of a molecule that induces the formation of semi-clathrate hydrates is tetrabutylammonium bromide (TtBABr) (see Figure 5.2). Aqueous solutions of this salt form crystalline clathrates at atmospheric pressure, below ~ -10 °C. Interestingly, once formed, they remain stable up to their melting point, around $9 - 12$ °C, [158, 160, 166, 167], and even reach room temperature (~ 20 °C) under specific conditions [168].

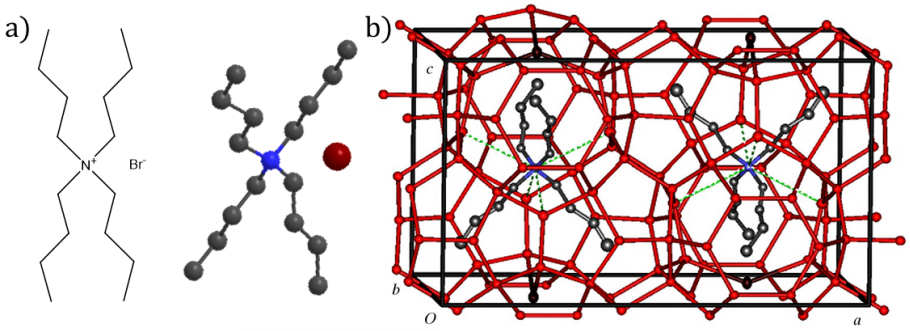

Figure 5.2: a) Molecular scheme and 3D model of tetrabutylammonium bromide ($(CH_3CH_2CH_2CH_2)_4N(Br)$, TtBABr) and b) its semi-clathrate hydrate. Bromine ions (dark red) are included into the supramolecular water structure (red). Reproduced with permission of the International Union of Crystallography from [158].

As we have shown in the previous chapter, the presence of several anomalies in the thermodynamic properties of bulk water are usually attributed to the presence of a liquid-to-liquid phase transition at low temperature. These effects are observable more than 80 K above the phase transition [79]. Moreover, the minimum of the heat capacity and compressibility at 36 °C and 60 °C, respectively, are also related to the

formation of ice-like structures within liquid water [124–126], again several degrees above the melting temperature of ice.

Despite the proximity to the phase transition in aqueous solutions of $TtBA^+$, the majority of the studies of the thermodynamic properties of clathrates are focused on the crystalline phase, neglecting the liquid structure at room temperature. However, there are several evidences pointing towards an anomalous hydration process in these systems, particularly in large tetraalkylammonium (TtAA) salts [169].

Dissolving this kind of solutes results in a negative entropy of solution [170, 171] and in the suppression of the density maximum of water [172], contrary to alcohols [173]. This suggests the formation of ordered structures around the $TtAA^+$ ions, which may extend over the whole liquid [170, 171]. This hypothesis is also supported by an increase in the stability of the water-water and cation-water interactions, particularly in those with large chains like $TtBA^+$ [169, 174].

Contrary to normal hydration processes in alkali halides, molecular dynamic (MD) simulations have shown an unexpected tangential orientation of the water molecules around $TtAA^+$, which extends beyond the first hydration shell for $TtBA^+$ [169, 175–177]. In this compound, the rotational time increases rapidly, for concentrations larger than 1 m, an effect not observed in smaller cations, like tetramethylammonium ($TtMA^+$) [169]. Moreover, Bradl et al. [172] reported a clathrate-forming tendency in undercooled $TtBA^+$ solutions, contrary to the glass-forming behavior of smaller $TtAA^+$ salts.

Notwithstanding that all these evidences point towards the formation of clathrate-like structures in solution, they were not detected by neutron scattering experiments, or they lead to inconclusive results [176, 178–182]. Probably, the continuous breaking and formation of these structures, with short life-times in solution, is the major impediment to the detection by many experimental techniques [174].

The formation of clathrate-like cages within the liquid may be observable by heat diffusion measurements, due to its high sensitivity to the formation of transient structures, as we have demonstrated in the previous chapter, and the characteristic timescale (see the Introduction Chapter).

Here, we discuss the analysis of calorimetric, spectroscopic and thermal transport measurements of different aqueous solutions of TtBABr and the equivalent phosphonium salt. Our results demonstrate that $TtBA^+$ (or similar pnictogen salts) induces the formation of large hydration spheres, which involve all the water molecules of the solvent, on a timescale large enough to modify the physicochemical properties of the liquid, forming a new family of supramolecular fluids.

5.1 Calorimetric characterization of TtBABr aqueous solutions

The formation of solid crystalline semi-clathrates, from aqueous solutions, is restricted to a certain range of concentrations, specific to each solute [153, 154, 171, 183, 184]. In the case of $TtBA^+$, the slow down in the rotational dynamics above ≈ 1 m, suggests a similar effect in the liquid phase [169]. Therefore, it is necessary to perform an accurate determination of the optimal concentration range for the formation of clathrate structures, in order to correlate the results between the solid and liquid phases.

With this purpose, we performed DSC measurements of a series of TtBABr aqueous solutions, at concentrations ranging between 0.2 m and 18 m (see Figure 5.3 a-b). The behavior up to 0.6 m is similar to pure water, showing an exothermic process at the ice crystallization temperature $(\mathrm{T_f(ice)})$ and an endothermic phase transition at its melting temperature, $\approx 0\ ^{\circ}\mathrm{C}$. Above this concentration, another exothermic peak appears at $\sim 10\ ^{\circ}\mathrm{C}$, before the crystallization of ice, as well as an exothermic transition at 9-12 $^{\circ}\mathrm{C}$, related to the formation and melting of the clathrate [154, 158, 160, 166, 167, 185].

From the ratio between the enthalpy of fusion of ice of pure water (ΔH_0) and the different solutions (ΔH), we can calculate the amount of water which forms ice (see Figure 5.3.c). Note that this value must be corrected by the actual mass of water in the solution, and can be expressed as:

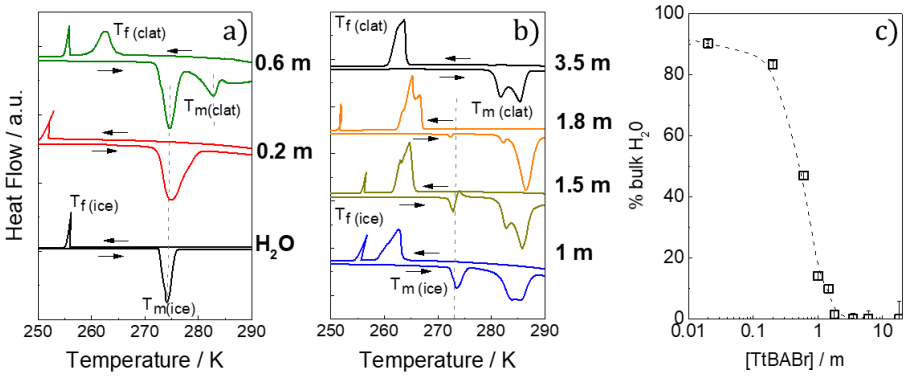

Figure 5.3: a) and b) DSC thermograms of aqueous solutions of TtBABr at different concentrations. Crystallization and melting of both ice and clathrate are produced at $\mathrm{T_f}$ and $\mathrm{T_m}$, respectively. Because the latent heat of ice crystallization is high, the endothermic peaks at $\mathrm{T_f(ice)}$ were cut to fit in the same scale. The temperature rate was set to 2 K/min. c) Fraction of ice-forming water extracted by the ratio between the enthalpy of fusion of ice at different concentrations and those of pure water, corrected by the actual mass of water in the solution.

$$\%\text{bulk } \mathrm{H_2O} = \frac{\Delta H}{\Delta H_0}\frac{m_T}{m_{H_2O}} \cdot 100 = \frac{\Delta H}{\Delta H_0}\left(1 + \frac{c \cdot M_s}{1000}\right) \cdot 100 \quad (5.1)$$

where $m_T = m_s + m_{H_2O}$ is the mass of the solution and M_s the molecular weight of the solute, divided by 1000 for having the same units as c.

Above 1.8 m, the amount of water participating in the formation of ice is practically suppressed. This concentration corresponds to a TtBABr:H_2O molecular ratio of 32.4, corresponding to one of the most stable clathrates of this compound [166]. Moreover, the enthalpy of fusion is $\Delta \mathrm{H_{fus}} = 183\ \mathrm{kJ/mol\ of\ hydrate}$, similar to the value reported by Rodionova et al. [166]. These results confirm that, above 1.8 m (and up to 3.5 m, at least, judging from the DSC curves) all water molecules are participating in the formation of solid clathrate hydrates, at low tem-

perature. The question is what is the dynamic molecular structure of the liquid when these clathrates melt.

5.2 Dynamic nature of the molten clathrates

Once the optimal concentration range for the formation of stable, solid clathrates was determined, the next step is the analysis of the liquid structure at these concentrations, and its relation (if any) with the clathrate structure. As mentioned before, the minimum in the temperature dependence of the adiabatic compressibility (K), is a probe of the transition between two different regimes [124, 125]: one above the minimum, dominated by thermal fluctuations, with a dK/dT>0, as most liquids; and another one at temperatures lower than T_{min}, in which structural fluctuations of the characteristic tetrahedral H-bond network dominate. Consequently, both the magnitude and the temperature dependence of K may be used as a probe to monitor the changes in the H-bond network of bulk water.

In Figure 5.4 we plot the results of the density and sound velocity of TtBABr aqueous solutions at different concentrations. Dissolving TtBABr results in a continuous increase of the density, with no significant changes on its temperature dependence. Nevertheless, the maximum in the v_{sound} vs. T is progressively suppressed, while the value at room temperature displays a maximum at [TtBABr]$\sim$ 3 m. These results are similar to those discussed in the previous chapter for water-alcohol mixtures, where the maximum in the sound velocity was related to the formation of ordered structures within the liquid phase.

To further corroborate this possibility, we have calculated the adiabatic compressibility and its temperature dependence (see Figure 5.5). Similar to sound velocity, increasing the concentration of TtBABr leads to a progressive displacement of the minimum to lower temperatures, and a rapid decrease on its magnitude, up to [TtBABr]$\sim$ 3 m. Above this concentration, K increases and recovers the temperature dependence of common liquids. Thus, considering the results presented in the previous chapter for the hydration of alcohols, it is plausible to assume

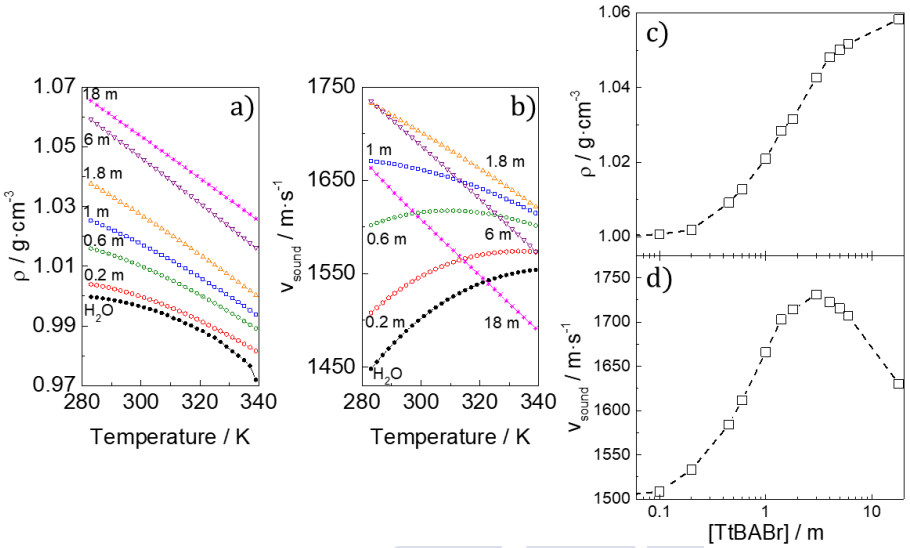

Figure 5.4: a-b) Temperature dependence of density and sound velocity, respectively, for aqueous solutions of TtBABr at different concentrations, and c-d) their values at 293 K. Not all concentrations are plotted in a-b), for clarity.

the formation of ordered, "iceberg-like" structures, stable at moderate concentrations (< 3 m).

However, thermal conductivity (κ) and diffusivity (α) measurements show a considerable reduction of both magnitudes at low concentrations (see Figure 5.6), faster above 0.2 m, in good agreement with the amount of bulk water present in the system (see Figure 5.3).

As we have discussed in the previous chapter, small alcohols are able to fit the water-like -OH group into the extensive network of water, without producing a significant distortion, at least at small concentrations. This results in an strengthening of the H-bond network and an enhancement of the rate of energy transfer.

However, the large hydrophobic chains of $TtBA^+$ are not compatible with the tetrahedral network of bulk water. Moreover, MD simulations have shown a small interaction between pairs of $TtBA^+$ molecules in solution [169], which suggest a complete solvation of the

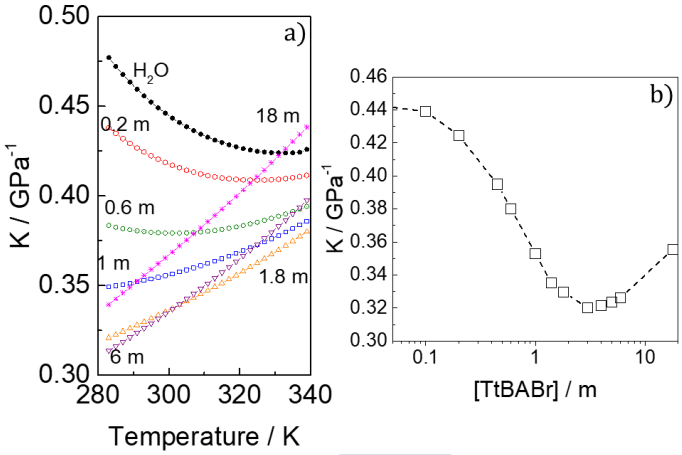

Figure 5.5: a) Temperature dependence of the adiabatic compressibility for aqueous solutions of TtBABr, at different concentrations, and b) its value at 293 K. Not all concentrations are plotted in a), for clarity.

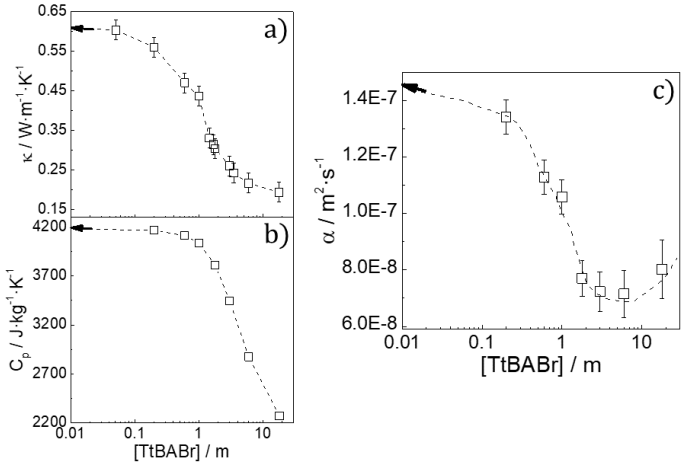

Figure 5.6: a) Thermal conductivity, b) heat capacity and c) thermal diffusivity of aqueous solutions of TtBABr, at different concentrations; all data taken at 293 K. The arrows indicate the corresponding values for pure water.

alkyl chains, without significant molecular segregation. Consequently, an enhancement of the heat diffusivity, as observed in alcohols, is not expected, despite they show similar behavior of the adiabatic compressibility. The message is that ordered structures do not always mean faster rate of energy transfer. What is relevant, however, is the minimum of α at exactly the same region as K.

We measured κ of an aqueous solution of $\mathrm{Mg(ClO_4)_2}$ with the same solute/water molecular ratio (1:30) than the 1.8 m solution of TtBABr. The $\mathrm{ClO_4^-}$ ion is known to be strongly coordinated to water molecules, an effect which can be monitored through the IR spectrum (see Figure 5.7). The IR absorption band of the OH-stretching mode of water presents two maximums, due to the presence of two distinct absorption components: OH groups hydrogen-bonded to $\mathrm{ClO_4^-}$ at high frequency, and OH groups hydrogen-bonded to other water molecules, peaking at lower frequencies. However, Omta et al. [103] demonstrated that this interaction is restricted to the first solvation shell, leaving the water molecules outside the closest vicinity, unaffected. Thus, by comparing the heat diffusion between TtBABr and $\mathrm{Mg(ClO_4)_2}$ solutions at the same molecular ratio, we can determine the origin of the anomalous heat transport in these systems.

We obtained a value of $\kappa = 0.52\ \mathrm{W\cdot m^{-1}\cdot K^{-1}}$ for $\mathrm{Mg(ClO_4)_2}$ (much higher than for TtBABr, $\kappa = 0.30\ \mathrm{W\cdot m^{-1}\cdot K^{-1}}$). Assuming four water molecules in the first solvation shell of each $\mathrm{ClO_4^-}$ ion, this amounts to a 13% of $\mathrm{H_2O}$ molecules affected by $\mathrm{ClO_4^-}$. Supposing that these molecules contribute with $0.16\ \mathrm{W\cdot m^{-1}\cdot K^{-1}}$ to the total thermal conductivity, leads $\kappa \approx 0.54\ \mathrm{W\cdot m^{-1}\cdot K^{-1}}$, close to the experimental value. Note that we used 0.16 $\mathrm{W\cdot m^{-1}\cdot K^{-1}}$, the thermal conductivity of ethanol, because it forms strong H-bonds with water, as in the first solvation shell of the perchlorate ion.

Thermal diffusivity leads to similar results; coordination around the ion leads to a decrease of $\sim 6.2\%$ in $\mathrm{ClO_4^-}$, while this reduction reaches a 47% in a 1.8 m aqueous solution of TtBABr . Consequently, the reduction of κ and α (and the minimum around 1.8 m) must be a consequence of an effect over the majority of water molecules of the

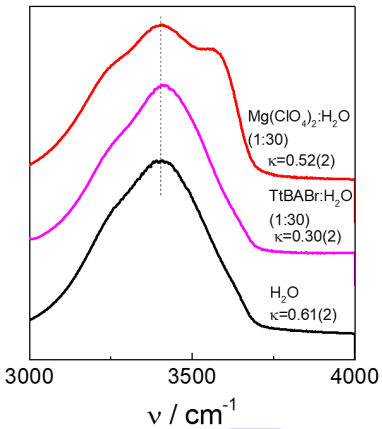

Figure 5.7: Comparison of characteristic IR absorption band of the intramolecular OH-stretching mode of water, for 1.8 m TtBABr and $\mathrm{Mg(ClO_4)_2}$ aqueous solutions. The thermal conductivity of each solution is indicated, in $\mathrm{W \cdot m^{-1} \cdot K^{-1}}$. All measurements were performed at room temperature.

system, as the low interaction between the cages [169] frustrates the heat transport.

The analysis of the temperature dependence of κ and C_p points in the same direction (see Figure 5.8). The negative slope of $\mathrm{dC_p/dT}$ below 36 $^{\circ}\mathrm{C}$ is related to the formation of ice-like structures in liquid water, and dissolving different solutes leads to a progressive recovery of the positive slope characteristic of most molecular liquids [186–189]. However, the negative slope of $\mathrm{dC_p/dT}$ increases for TtBABr, reaching a minimum at $\sim$ 1.8 m, and does not recover positive slopes until $\sim$ 5 m.

The formation of clathrate-like structures, where water molecules are locked into the structure during a certain amount of time, suppresses the translational and rotational modes at room temperature. These modes are the main contributions to $\mathrm{C_p}$ in bulk water above room temperature and, consequently, are the responsible of the positive $\mathrm{dC_p/dT}$. Thus, these results support an scenario where the liquid phase resembles a molten clathrate, with all water molecules forming part of a supramolecular structure, with rotational and translational dy-

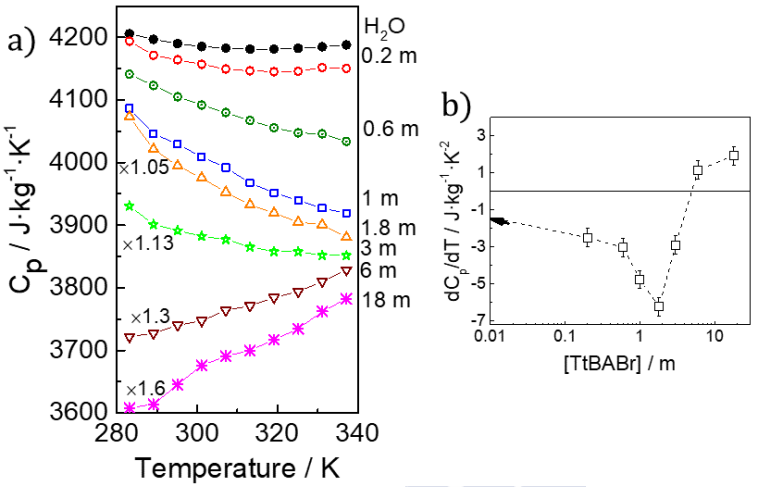

Figure 5.8: a) Temperature dependence of the heat capacity for aqueous solutions of TtBABr, at different concentrations. b) Slope, taken at 293 K, of the C_p vs.T, for different concentrations. The arrow indicates the value for pure water.

namics heavily influenced by the presence of the TtBABr. This is very different to the picture in which only the closest molecules to TtBABr behave differently to the bulk.

Regarding heat transport, Frenkel [30] introduced the notion of liquid relaxation time, τ, as the time between two consecutive molecular displacements at one point in space, so despite the absence of long-range translational symmetry, liquids may also support shear waves with frequency $> 1/\tau$, the timescale where the liquid structure remains solid-like. Thus, liquids are able to maintain phononic-like modes, although only those of very high-frequency, with wavelengths close to intermolecular separation. [4–7]. Quoting Trachenko and Brazhkin [7]: "liquids have solid-like ability to support shear stress, with the only difference that this ability exists not at zero frequency as in solids but at frequency larger than $1/\tau$".

This results in low heat diffusion rates, in comparison with crystalline solids. However, the formation of ordered networks, with larger

relaxation times, should in principle increase the spectrum of available frequencies, leading to larger thermal conductivities. The observation of a lower thermal conductivity in the optimum concentration range of TtBABr indicates a lower bond strength than in water, probably due to a larger intermolecular distance.

On the other hand, due to the increasing long-range order of the system upon crystallization, κ is particularly appropriate to the determination of the type of liquid-to-solid phase transitions.

We measured the temperature dependence of κ for two different TtBABr solutions and pure water (see Figure 5.9). Clathrate crystallization in the 1.8 m solution does not produce a large change in the thermal conductivity, contrary to what happens in pure water or at low concentrations. This situation suggests a small change between liquid and crystalline structures, similar than in a glass transition [151]. Consequently, these measurements confirm the formation of molecular clathrate-like structures already at room temperature in the liquid phase; cooling below the crystallization temperature (as observed by DSC) does not produce a significant increase of the thermal conductivity of the system.

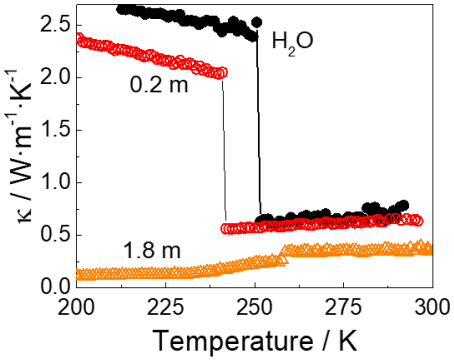

Figure 5.9: Temperature dependence of the thermal conductivity for two representative TtBABr solutions, and pure water. The measurements were performed with a cooling rate of 1 K/min, to increase the accuracy of the measurement.

5.3 Spectroscopic characterization of the solutions: IR and NMR

Spectroscopic measurements are one of the most used experimental strategies to investigate the structure of liquids, including water and its solutions [32, 33, 67, 86, 90, 92, 94, 98, 100–103, 122, 139, 140, 169, 174, 178, 182]. These techniques allow a detailed analysis of the inter and intramolecular structures, which are fundamental to corroborate the structure dynamics deduced from the analysis of the heat transport.

First, we analyzed the IR absorption associated to the intramolecular OH stretching mode of several TtBABr aqueous solutions (see Figure 5.10). The characteristic frequency of this mode is an indirect measurement of the strength of the H-bonds between pairs of water molecules [67, 190–192]. The experiments were performed in 4% D_2O in H_2O, to separate the contribution from symmetric and asymmetric stretching modes. The rapid increase of the wavenumber (ν) at 0.6-3 m indicates a strengthening of the intramolecular OH mode, associated with a weakening of intermolecular H-bonds, which suggests a change of the intermolecular interactions in this concentration range.

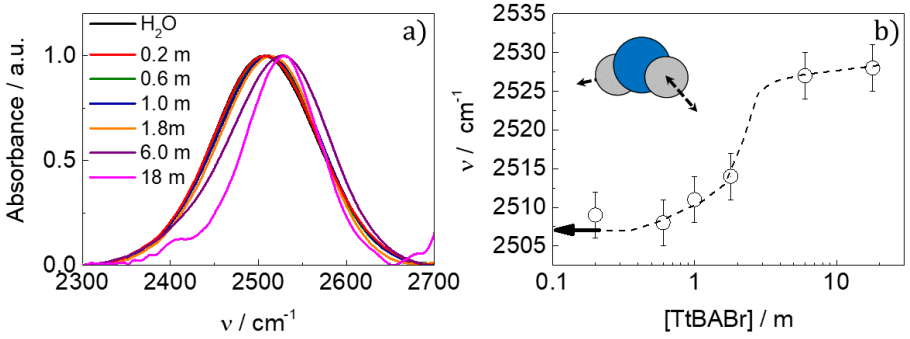

Figure 5.10: a) Room temperature IR spectra and b) the frequency at the absorption maximum, for different TtBABr solutions.The arrow in b) indicates the value of pure water. Experiments were performed in 4% D_2O in H_2O.

To further corroborate this interpretation, we followed the temperature dependence of this absorption band (see Figure 5.11). Above 0.6 m, the formation of clathrates at low temperature, $T_f(clat)$ produces a small increment of the intensity, followed by a larger increase below $T_f(ice)$; this second transition is suppressed at 1.8 m, confirming the absence of bulk-like water observed in DSC (see Figure 5.3.f). Note that the change of the intensity at $T_f(clat)$ is similar at all concentrations, suggesting a similar H-bond rearrangement (probably involving the same number of water molecules).

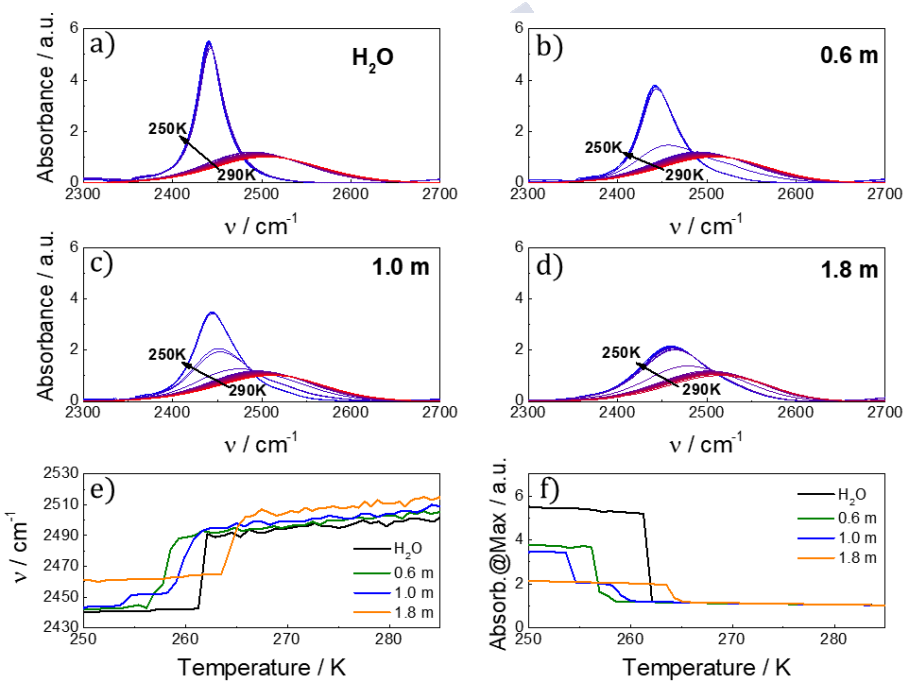

Figure 5.11: a)-d) Temperature dependence of the IR spectra for different TtBABr aqueous solutions. The experiments were performed dissolving the TtBABr in 4% D_2O in H_2O, to separate the contributions of symmetric and asymmetric stretching modes. e) Temperature dependence of the characteristic frequency and f) the maximum absorption, normalized to the value at room temperature. Samples were cooled down at 2 K/min.

The higher dipole moment of ice with respect to liquid water, as well as the strengthening and narrowing of the frequency distribution of H-bonds, produces a change of the absorption band from a Gaussian to a Lorentzian shape [192] (see Figure 5.12). However, this is not the case in the clathrate-crystallization process, where the experimental data fit better to a Gaussian function in the whole temperature range, suggesting a small structural change between liquid and crystalline phases.

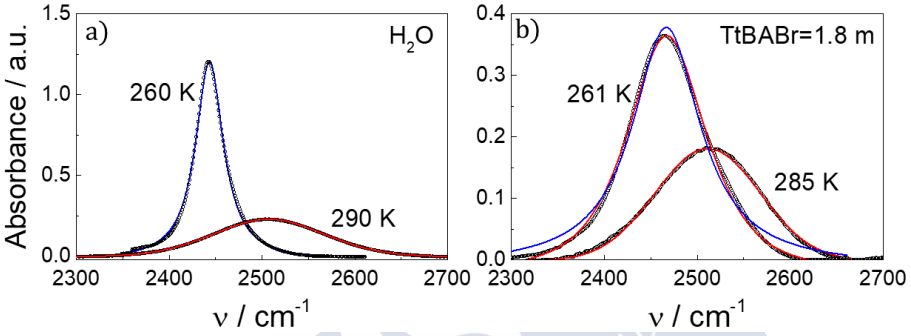

Figure 5.12: a) Fitting of the experimental absorption (black circles) of pure water and b) 1.8 m TtBABr aqueous solutions, at room temperature and below the crystallization temperature. Red/blue lines represent the fitting to a Gaussian and Lorentzian functions, respectively.

The results presented in this chapter suggest the formation of a supramolecular liquid, with a dynamic molecular structure similar to a crystalline clathrate. Consequently, each group of $\mathrm{TtBABr:xH_2O}$ (x=17-38) molecules behaves as an individual molecule, interacting loosely between them and, consequently, reducing the heat transfer rate. This scenario is in accordance to the lack of interaction between pairs of $\mathrm{TtBA^+}$ ions reported in MD simulations [169] and the slow down in their diffusion and rotational times [169, 174].

The anomalous dynamics of the cation can also be explained in terms of an interpenetration of water molecules inside the arms of the $\mathrm{TtBA^+}$ [169]. However, the analysis of the dynamics of the anion may be more conclusive, as it forms part of the semi-clathrate structure in the crystalline phase [158]. Thus, we have analyzed the $^{79}\mathrm{Br}$ NMR spectra

of TtBABr aqueous solutions at several concentrations. Comparing the results with those of a 1.1 m KBr solution (see Figure 5.13) confirms that the large broadening and deshielding observed in TtBABr solutions is not compatible with simple bromine hydration.

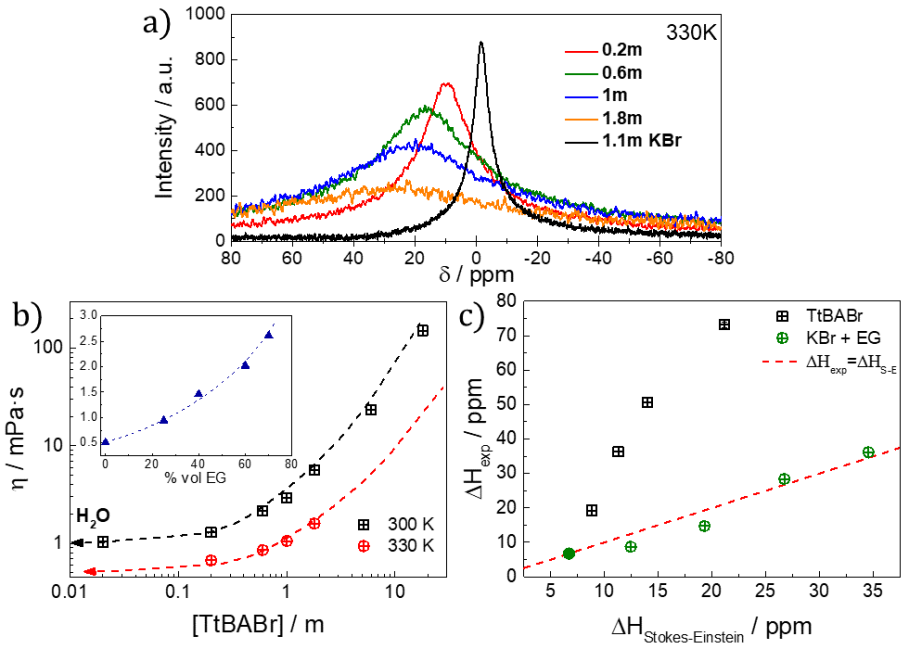

Figure 5.13: a) ^{79}Br NMR spectra for different aqueous solutions of TtBABr at 330K. We represent the values at this temperature in order to have an observable signal at high concentrations. We also measured a 1.1 m solution of KBr for comparison (black line), which has been divided by 4, to fit in the same scale. b) Experimental values for the viscosity for different concentrations of TtBABr, at 300 K and 330 K. The inset shows the viscosity for 1.1 m solutions of KBr in water-ethyleneglycol mixtures, at different volume fractions. c) Comparison between the experimental ^{79}Br NMR linewidth (ΔH) at 330 K (black squares) and the prediction from the Stokes-Einstein equation (red line), assuming the same hydrodynamic radius than simple bromine hydration of KBr (solid green circle). Green circles represent the experimental linewidths for solutions of KBr in different H_2O-EG mixtures.

To discard a possible line broadening produced by an increase in the viscosity of the solution (η), we have calculated the dependence of the NMR linewidth (ΔH) with η, using the Stokes-Einstein equation [193]:

$$\Delta H \propto \frac{1}{D} = \frac{6\pi\eta r_h}{k_B T} \tag{5.2}$$

where r_h is the hydrodynamic radius and T the temperature. Because r_h is unknown, we have assumed the same value than simple bromine hydration in KBr. Thus, ΔH can be rewritten relative to the value of the 1.1 m KBr solution as follows:

$$\Delta H = \frac{\eta}{\eta(\text{KBr})} \Delta H(\text{KBr}) \tag{5.3}$$

By adding ethyleneglycol (EG) to the KBr solution to increase the viscosity, the rise of ΔH agrees with the predictions from the Stokes-Einstein equation (see Figure 5.13.c). However, this is not the case of TtBABr, where a much larger broadening than expected is observed. This supports the hypothesis that Br^- is already forming part of the hydration skeleton of the clathrate-like structure, already in the liquid phase and, consequently, r_h is larger.

These structures are unstable as temperature increases, and the signal of Br^- is partially recovered and progressively displaced closer to $\delta = 0$ (see Figure 5.14). Note that the peak at 0.2 m is observable even at room temperature, suggesting the need of a specific water-salt ratio to form the supramolecular clathrate structures [154, 183].

5.4 Formation and stability of supramolecular structures in water solutions of other salts

The formation of clathrate hydrates in the solid state is not restricted to TtBABr, but there are a broad range of salts that induce similar structures [153]. This offers a chart of compounds which could induce the formation of supramolecular liquids, with interesting properties as

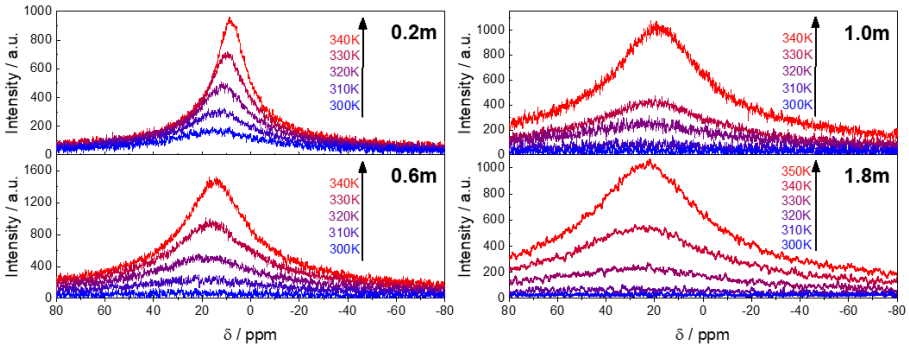

Figure 5.14: Temperature dependence of ^{79}Br NMR signal, for different concentrations of TtBABr in water.

discussed above. Because changing the anion produces small negligible changes on the temperature of formation and melting of clathrates [153, 155, 194, 195], we will focus on the effect of the cation. We restricted our analysis to cations with a symmetric disposition of the alkyl chains, as no crystalline structures were reported in compounds showing a strong asymmetry of the length/disposition of the organic chains [153].

First, we pursued the most obvious path: we studied the effect of the cation size in the formation of a supramolecular liquid, which has an important influence on the formation of solid clathrates [171]. Thus, we prepared solutions of different tetraalkylammonium bromide salts (TtXABr) at several concentrations, and compared their physicochemical properties with the TtBABr solutions (see Figure 5.15).

As discussed before, the maximum/minimum in v_{sound}, K, and α, can be taken as a probe of the formation of clathrate-like structures in the liquid phase, as we have demonstrated. The solutions of alkyl compounds shorter than $TtBA^+$ present a monotonic change of these properties, without any maximum/minimum. Increasing the length of the alkyl chain above TtPABr produces a fast increase of the heat capacity, maybe suggesting the begging of the formation of the supramolecular structures, but without reaching the singular behavior observed

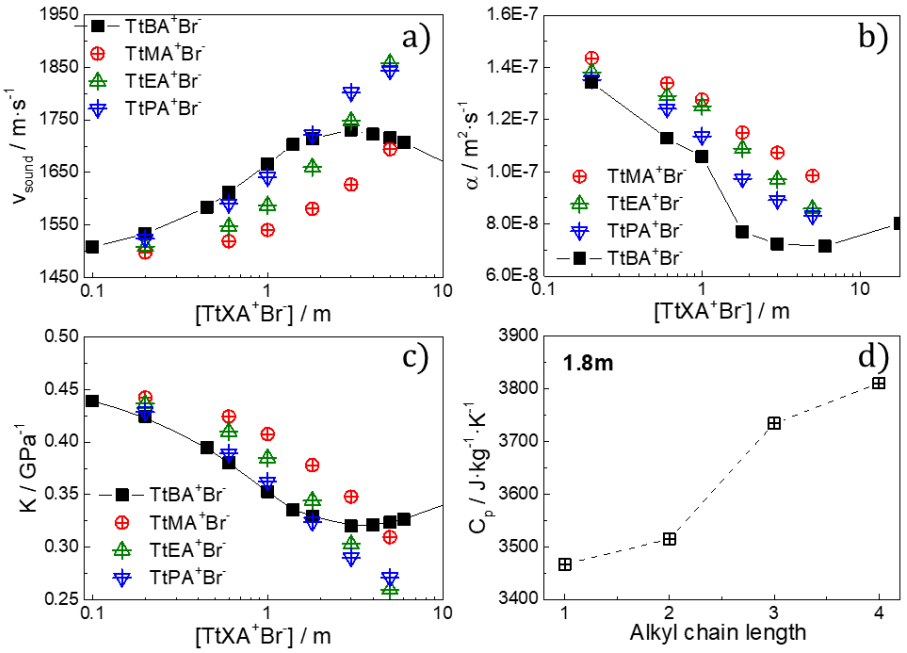

Figure 5.15: Room temperature v_{sound} (a), α (b) and K (c) for different solutions of tetra methyl (TtMABr), ethyl (TtEABr) and propyl (TtPABr) ammonium bromide in water. The data of TtBABr are presented again, for comparison. d) Room temperature heat capacity for 1.8 m aqueous solutions, as a function of the alkyl-chain length.

in the tetrabutyl compound. These results are in accordance with reports in the solid state, where small cations do not induce the formation of crystalline clathrates, or they involve a small number of water molecules [153].

The solubility of organic molecules decreases with the size of the alkyl chain [196,197]. However, this is not the case for tetraaklylammonium salts, where the participation of water molecules into the clathrate-like structure increases the solubility up to 7 times [198].

Next, we studied the effect of other pnictogen salts, involving equally large alkyl chains surrounding the central atom. Replacing

the central N atom by P (tetrabutylphosphonium bromide, TtBPBr), induces the formation of crystalline clathrates at similar molecular ratios as TtBABr:H_2O [155, 194, 195, 199, 200].

The DSC analysis of TtBPBr shows that in this case, the optimal concentration range occurs at concentrations slightly lower than in TtBABr (see Figure 5.16).

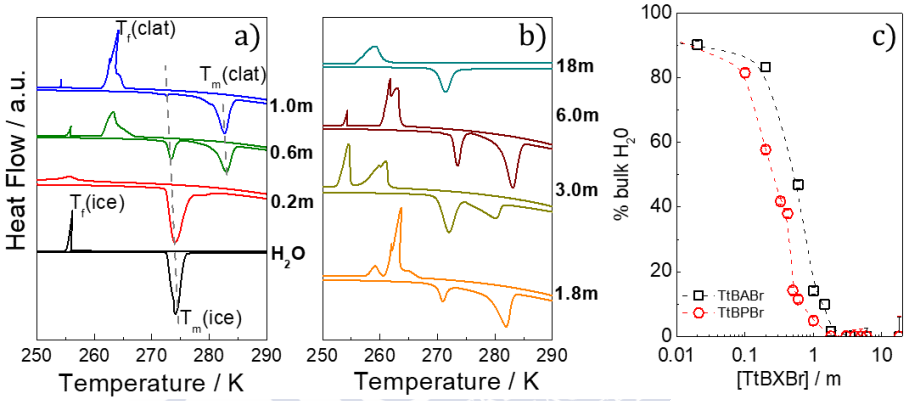

Figure 5.16: a) and b) DSC thermograms of aqueous solutions of TtBPBr at different concentrations. The endothermic peaks at $T_f(ice)$ were cut to fit in the same scale. c) Fraction of ice-forming water for different TtBABr and TtBPBr solutions, corrected by the actual mass of water in the solution.

The TtBPBr clathrates start forming above 0.6 m, and present crystallization and melting temperatures similar to TtBABr compounds. Note that above 1.8 m a new exothermic peak appears at T$\sim$273 K, which can be interpreted as ice crystallization because of the similarity of the melting temperatures. However, this peak stays present even at [TtBPBr]=18 m, where the ratio H_2O:TtBPBr is 3. Thus, this phase transition can not be associated to the formation of ice, and is probably a consequence of the presence of two different types of clathrates [194, 201].

The thermodynamic properties of the solutions show the same anomalies reported for the supramolecular liquid phase of TtBABr, sug-

gesting the existance of similar structures also in this case (see Figure 5.17).

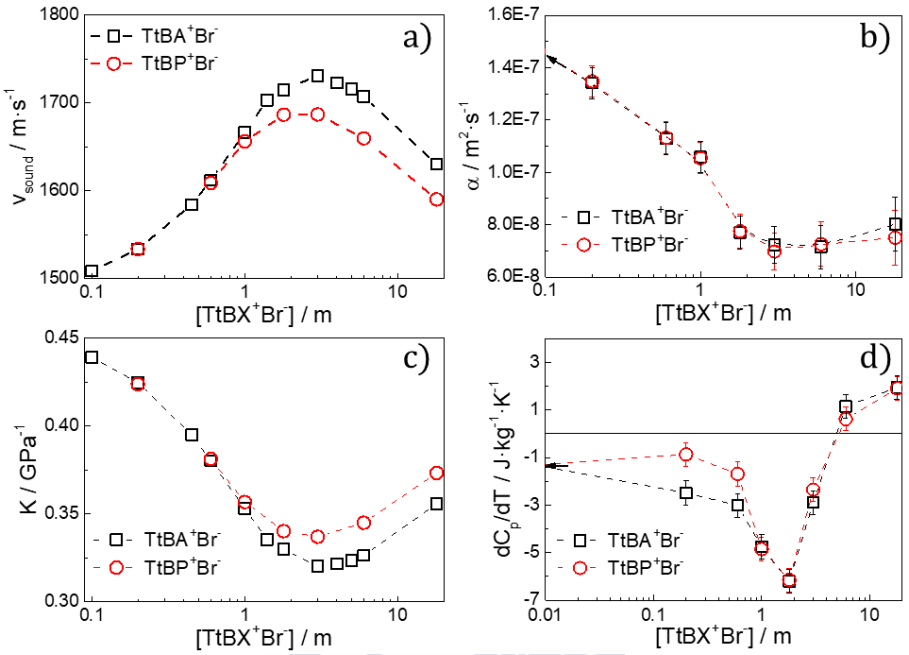

Figure 5.17: Room temperature v_{sound} (a), α (b), K (c), and the slope of C_p vs. T (d), for TtBPBr in water. The results for TtBABr are shown again, for comparison.

In conclusion, the formation of clathrate-like structures within the liquid phase is restricted to large and symmetric cations. The interesting physicochemical properties discovered are not particular of a specific salt; there are a broad range of possibilities which can be accessed by changing the atoms of the cation or by using different anions. These changes produce different thermodynamic properties, and have important consequences on the crystallization/melting temperatures. As a consequence, it should be possible to tune the melting/crystallization temperatures and physicochemical properties of this interesting type or liquids, for a particular application.

5.5 Summary

In this chapter we have studied the effect of increasing the hydrophobic effect, up to the point to create a new type of fluids which we coined as *"supramolecular fluids"*. The molecular structure of TtBABr aqueous solutions is related to the clathrate structure formed at low temperatures and/or high pressures, and involves the majority of water molecules. This allows the extrapolation of some of the interesting properties of solid crystalline clathrates, to the liquid phase, like the possibility of be used as sequestering agents in some chemical reactions.

Due to the formation of ordered structures with low connectivity, these fluids are highly incompressible and present a significant reduction of the thermal diffusivity, despite the increasing in the molecular order. These cages are more stable than the tetrahedral network of bulk water, and the physicochemical properties of the fluid are dominated by structural fluctuations of these structures, as it is deduced from the analysis of the temperature dependence of the adiabatic compressibility, and heat capacity.

Similar results were obtained for other large pnictogen salts, suggesting a general behavior of these systems. Note that this phenomenology is related with solid state structures, suggesting a possible rule in order to predict the formation of these supramolecular fluids, from the vast amount of data available regarding the stability of solid clathrates.

Our analysis of the heat transport as a probe of the dynamic molecular environment constitutes an original approach to the analysis and the design of new systems, which may have unforeseen properties and applications, as we have demonstrated in a recent article [73].

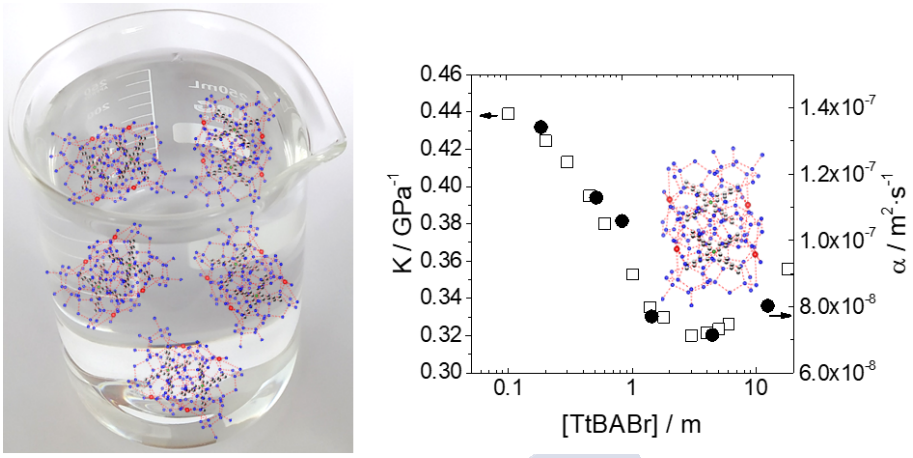

Figure 5.18: Graphical summary of the main results obtained in this chapter. Clathrate structures are formed within the liquid in a certain range of concentrations, creating a new family of supramolecular fluids with distinctive thermodynamic properties.

6. Thermal conductivity across solid-liquid phase transitions

An important part of this project is the analysis and design of systems which allow an effective control of the heat transport, the so-called thermal regulators. This challenging problem has centered the efforts of several groups in the last years [202–215], as it is fundamental for the development of effective energy storage solutions [9], phononic devices [10–13], etc.

Thermal regulators can be broadly defined as systems with two thermal states: a high/low thermal conductivity state that can be switched between them [13, 211]. This switching can be thermally induced (the vast majority), going across different phase transitions, or (ideally) it can be induced by an external stimulus, like the application of an electric/magnetic field [206, 207] or light [214, 216]. In one of the many possible applications of such devices, the high-conductivity mode could be activated when the temperature (or other magnitude of interest) reaches a certain value, to impede an excessive heating, maintaining the device within a specific range of temperatures (see Figure 6.1).

The main approach to this challenge consists in taking advantage of the thermal conductivity difference produced in some phase transitions [217]. The main challenge of this approach is to enhance the switching ratio. The most promising strategy is the suspension of carbon based nanostructures introduced by Chen et al. in 2011 [217]. In their work, they have demonstrated that the suspension of graphite or carbon nanotubes results in a large enhancement of the switching ratio,

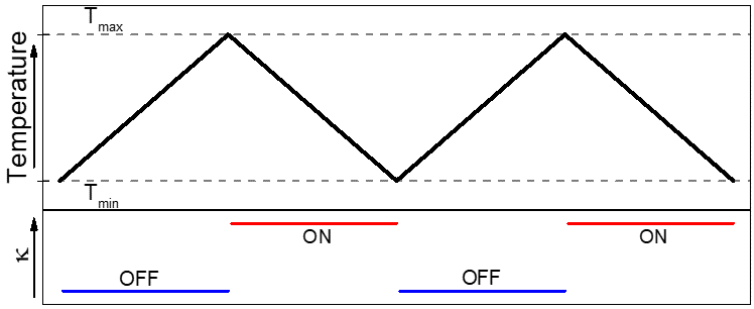

Figure 6.1: Sketch of the basis of thermal regulators. Once the temperature reaches a maximum value, the thermal regulator is switched on, increasing the thermal dissipation and, consequently, reducing the temperature of the device. ON an OFF indicate high and low thermal conductivity states, respectively.

reaching a value of 3.2 for a 1% graphite/hexadecane suspension. As they have demonstrated, this is a general mechanism for carbon-based nanofluids, which opens a new avenue in the design of thermal regulators.

In this regard, the use of Ionic Liquids (ILs) is also particularly interesting, as they display a large range of crystallization/melting temperatures (190-350 K) [218], which can be adjusted by selecting different anion-cation combinations, allowing the possibility of choosing the best system for a particular application.

In the aqueous solutions studied in previous chapters, the properties of the system vary according to how the presence of the solute affects the H-bond network of water. However, ILs are purely ionic and, consequently, they should be dominated by the Coulomb potential. However, H-bonds introduce directional interactions, which can be regarded as defects in the isotropic Coulomb potential [219]; as a consequence, the presence of strong H-bonds has been shown to be an important contribution for understanding the behavior of ILs [219–233]. This scenario was confirmed by MD simulations by Zahn et al. [234], where the presence of induction/dispersive forces reduces the energy barrier between

different cation/anion arrangements, which determines the crystallization temperature and the low temperature structure.

In this regard, imidazolium-based ILs (Im-ILs) are perfectly suitable compounds to perform a systematic study of the effect of different interactions on the formation of ionic solids. The strengthening of H-bonds decreases by an alkylation of the N(1) or C(X) sites of the imidazolium ring [227,233]. This effect is more pronounced if we change the group attached to C(2), at it is the preferred group for H-bonding [219]. Similar phenomenology can be achieved by changing the anion, where the introduction of protic groups increases significantly the H-bond strength [223, 224]. Further anisotropy in the intermolecular interaction potential can be introduced by increasing the alkyl chain length, as van der Waals forces and steric effects also contribute to the energy landscape (see Figure 6.2).

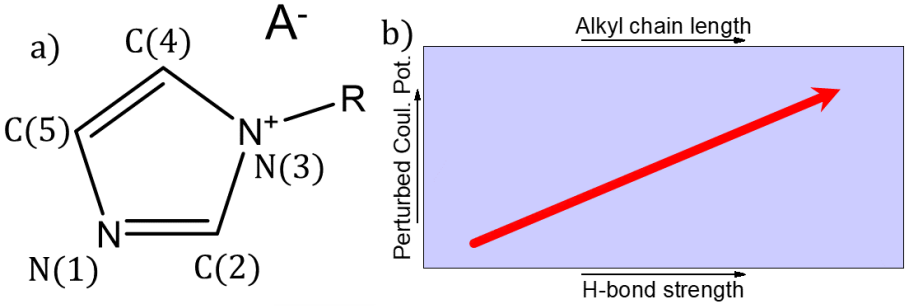

Figure 6.2: a) Scheme of imidazolium based ILs. The imidazolium ring shows four possible positions for H-bonding, labeled as C(2), C(4), C(5) and N(1); A^- represents the anion. b) Cartoon of the dependence of the disturbance to the Coulomb potential with the different types of defects. Their contribution increases with the alkyl chain length or with the H-bond strength, or a combination of both.

In this chapter, we report a systematic study of the effect of H-bonds and alkyl chain length on the nature of the solid phases formed at low temperature in a series of Im-ILs. Our results show how the ratio of these interactions can be used to determine the formation of a crystal

or a glass at low temperatures, with a profound effect in the transport of heat. Importantly, we show that a glass to partially crystalline phase may occur in some cases, with an important reversible change in the thermal conductivity of an all solid material [62].

Finally, as a prospective of this work, we show an example of a light induced phase transition in an azobenzene based compound, leading to a large thermal conductivity variation ($\approx 40\%$), close to room temperature. The versatility of these systems opens a new avenue for the design of thermal regulators controlled by an external-stimulus, allowing the control of heat transfer at the nanoscale [235–248].

6.1 Characterization of H-bond strength

As mentioned before, the main objective of this part of the work was to find a key that allows modifying the crystallization process in an ionic solid, with the aim of controlling the thermal transport of the solid phase that is formed at low temperature. Fumino et al. [219] established that directional H-bonds can be treated as perturbations to the isotropic Coulomb potential, and, if sufficiently strong, these defects can frustrate the crystallization at low temperature. We thus thought that the anisotropy introduced by H-bonds and long alkyl chains in the spherical potential of an ionic liquid, could be key to control thermal transport in ionic solids.

First, we performed a systematic analysis of the H-bond strength in a series of Im-ILs by FTIR spectroscopy [227, 249]. To do that, we studied two different regimes of the spectra: mid-IR ($400 - 4000\ \mathrm{cm}^{-1}$) and far-IR ($30 - 400\ \mathrm{cm}^{-1}$). The characteristic bands between $3000 - 3300\ \mathrm{cm}^{-1}$ are associated with the intramolecular C-H stretching mode, which is an indirect measurement of the intermolecular H-bond strength [224]. On the other hand, the wavelength at the maximum of the band at $\approx 50 - 175\ \mathrm{cm}^{-1}$ directly probe the strength of the intermolecular C-H $\cdots$ A^- H-bond [224] (see Figure 6.3).

We have analyzed the IR spectra of a series of Im-ILs, varying systematically the availability of the most acidic C(2) and N(1) positions

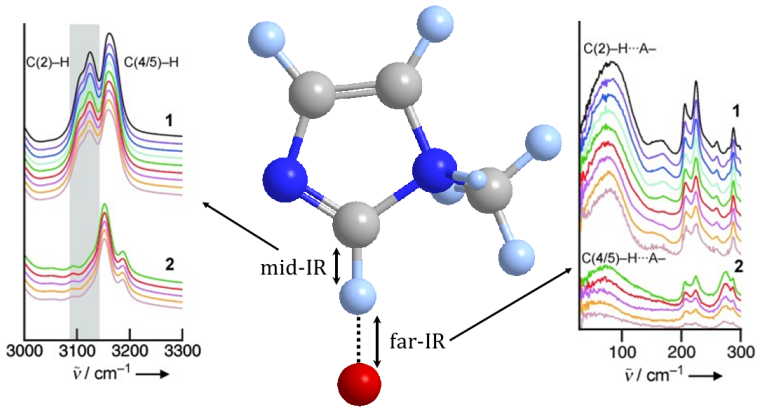

Figure 6.3: Scheme of the IR absorption bands associated to inter and intramolecular stretching modes in Im-ILs. In the molecular scheme, the red sphere represents the anion, which is hydrogen bonded to C(2) position at the imidazolium ring. Spectra are reproduced with permission from [219]. Copyright© 2008 WILEY-VCH Verlag GmbH & Co. KGaA, Weinheim.

and the anion (see Figure 6.4). There are two overlapped bands in the mid-IR spectra (see Figure 6.4.a): a low frequency band assigned to C(2)-H stretching, and a high frequency band due to the C(4/5)-H vibration [233]. The progressive redshift of the intramolecular C(2)-H suggests a strengthening of the intermolecular H-bond. These results are confirmed by the increasing frequency in the far-IR spectrum (see Figure 6.4.b).

It is worth noting that the decreasing of molecular weight in the series also contributes to the blueshift of the far-IR absorption band [225, 250, 251]. Assuming an harmonic oscillation model, the wavelength of the vibration can be expressed as:

$$\nu = \frac{1}{2\pi c}\sqrt{\frac{k}{\mu}} \tag{6.1}$$

where k reflects the strength of the interaction and μ is the reduced mass of the molecule:

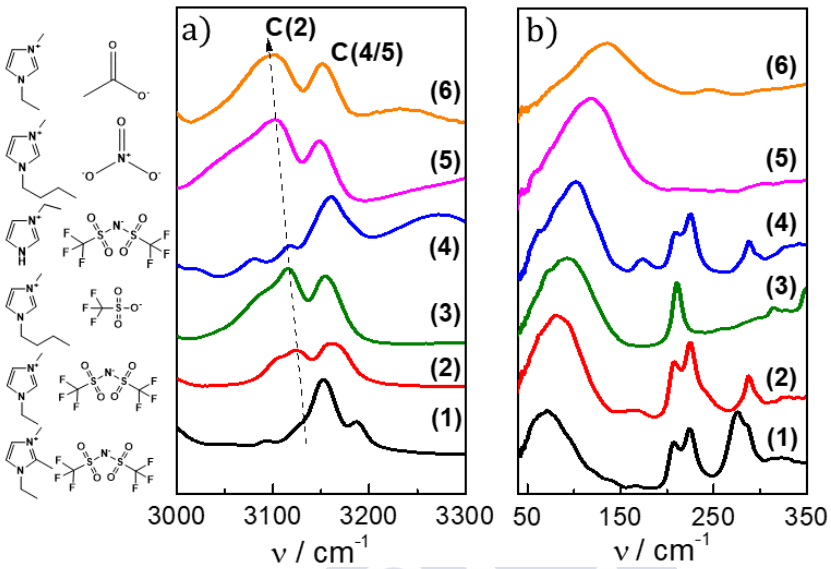

Figure 6.4: Mid-FTIR (a) and far-FTIR (b) spectra of the Im-ILs studied in this work. **(1)** 1-Ethyl-2,3-dimethylimidazolium bis(trifluoromethylsulfonyl)imide (EBisMIM-NTF_2); **(2)** 1-ethyl-3-methylimidazolium bis(trifluoromethylsulfonyl)imide (EMIM-NTF_2); **(3)** 1-butyl-3-methylimidazolium triflate (BMIM-TfO); **(4)** 1-ethylimidazolium bis(trifluoromethylsulfonyl)imide (EIM-NTF_2); **(5)** 1-butyl-3-methylimidazolium nitrate (BMIM-NO_3); **(6)** 1-ethyl-3-methylimidazolium acetate (EMIM-Ac). At the left we show the molecular scheme of the different molecules. C(2) and C(4/5) indicates band associated to the C-H stretching mode, at positions 2 and 4/5 of the imidazolium ring, as it is indicated in the scheme of Figure 6.2. The dashed arrow in (a) shows the blueshift of the C(2)-H band.

$$\mu = \frac{\mathrm{M(anion)} \cdot \mathrm{M(cation)}}{\mathrm{M(anion)} + \mathrm{M(cation)}} \tag{6.2}$$

Considering this relation, we have calculated the variation of ν associated to this effect, obtaining a much smaller effect than those observed experimentally (see Figure 6.5). This result demonstrates that

the main contribution to the frequency shift is the H-bond strengthening.

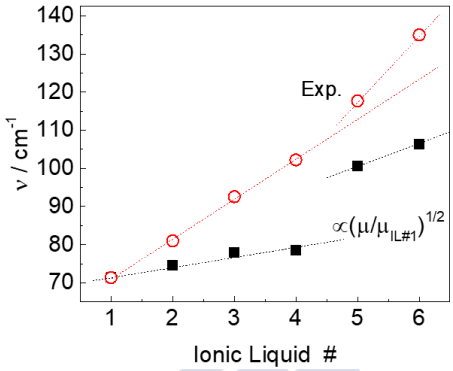

Figure 6.5: The experimental wavenumber of the C-H $\cdots$ A^- stretching mode (open red symbols), for different ILs studied in this chapter. The solid black squares represent the expected values considering the increase of the reduced mass, calculated from the harmonic oscillator approximation (Eq. 6.1). Lines are guides to the eye.

6.2 Liquid-to-solid phase transition

The effect of an increasing H-bond strength over the characteristic temperature of the liquid-to-solid phase transition was studied by DSC experiments. Overall, there is a clear tendency to decrease the crystallization temperature as the H-bond strength increases; slight deviations from this global trend, as the increase of T_c observed in **(3)**, are most probably a consequence of the smaller size of the anion in this case, which facilitates the molecular rearrangement and, consequently, the crystallization.

More interesting is the observation of the replacement of the sharp peak characteristic of the liquid-to-crystal phase transition, by a gradual change of slope of the DSC trace in the ILs with larger H-bond strength. In the warming curve, endothermic crystallization peaks are observed

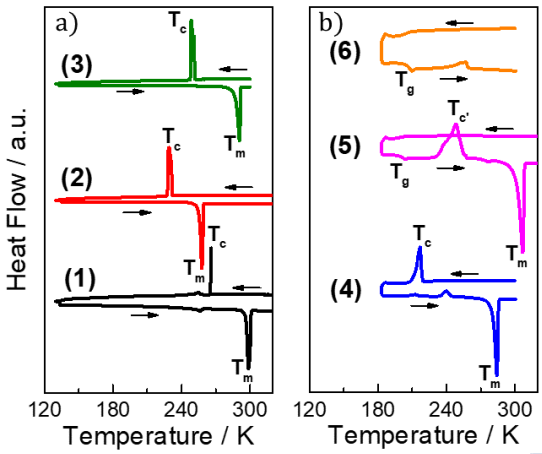

c)

	T_c / K	T_g / K	T_m / K
(1)	240		290
(2)	225		250
(3)	231		281
(4)	216		284
(5)		205	
(6)		210	

Figure 6.6: a)-b) DSC thermograms of the different ILs studied in this work. Temperature ramps were fixed to 2 K/min. T_c, T_m, T'_c and T_g correspond to crystallization, melting, recrystallization and vitrification temperatures, respectively. These temperatures are summarized in a table at c).

before the exothermic peak at the melting temperature. These observations suggest that a glass instead of a crystal is formed upon cooling the ILs with large H-bond strength, at sufficiently low a temperature. This hypothesis was corroborated by the measurement of the dependence of the electrical conductivity (σ) with temperature (see Figure 6.7). The ionic mobility is suppressed upon crystallization and, consequently, σ shows a sudden drop in ILs **(1)** to **(4)**. This insulator character is maintained up to the melting temperature, where liquid values are recovered. Increasing the H-bond strength results in a smother drop of σ and in a suppression of the hysteresis. Note that the partial recrystallization in **(5)** observed in DSC reopens the hysteresis at T'_c.

To study the nature of the glassy and crystalline phases formed at low temperature, we performed X-ray diffraction (XRD) and polarized optical microscopy (POM) experiments. In Figure 6.8 we show the results for three ionic liquids representative of the three different phases formed at low temperature.

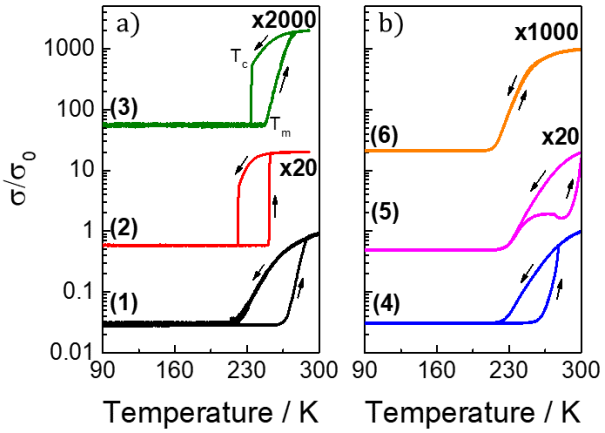

Figure 6.7: Dependence of the electrical conductivity with the temperature of the different ILs studied in this work. Temperature ramps were fixed to 1 K/min. The curves have been multiplied by a factor (indicated), to fit in the same scale.

The dots observed in the XRD pattern of Ionic Liquid **(1)**, which has the weakest H-bonds, suggest the formation of a 3D ionic crystal. In liquids **(2)** to **(4)**, and also after the recrystallization of **(5)**, the partial circles observed in XRD show the formation of liquid crystals [252], which is also supported by the texture observed in POM images. Finally, increasing further the H-bond strength results in the formation of a glass at low temperature [253, 254].

Surprisingly, this glassy state is unstable upon further cooling, and POM images show the sudden appearance of fracture lines throughout the whole sample below T_f (see Figure 6.8.d). However, this effect does not seem to be related to any phase transition, as is not observable in XRD, and, particularly, in DSC.

To shed light into the anomalous transition observed in POM, we analyzed the temperature dependence of the thermal conductivity (see Figure 6.9). As we have already shown in this thesis, this macroscopic transport property is highly sensitive to tiny conformational changes at molecular level. Different from electrical conductivity, heat diffusion

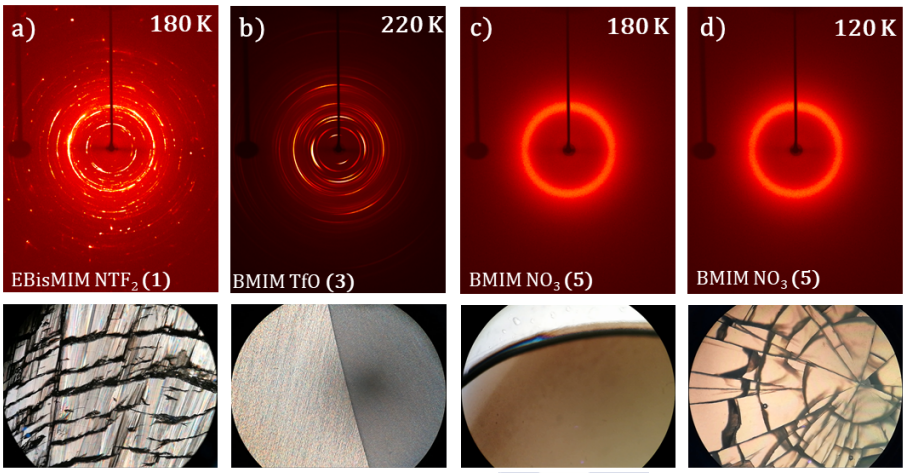

Figure 6.8: Top: Low temperature X-ray diffraction patters of three ILs representative of each type of solid phase. Bottom: POM images at the same temperatures. We represent two temperatures for IL **(5)**, in order to show the fracture lines formed upon further cooling. See the videos in the Supplementary files of our paper in Ref. [62] to follow the dynamics of the different phase transitions.

can be measured continuously across the liquid-to-solid phase transition, which makes κ a particularly appropriate property to study the nature of the crystallization of the ILs.

We can group the ILs in two different categories: (i) Liquids **(1)** to **(4)** and (ii) ILs **(5)** and **(6)**. The transition between both groups is evident even at room temperature, where the formation of strong H-bonds leads to a large increase of the thermal conductivity. In principle, this result points to an improved intermolecular communication by a water-like H-bond network in the IL [221, 224].

The first group of ILs shows a large increase of κ below $\mathrm{T_c}$, with the higher temperature dependence characteristic of ordered systems. On heating, the high thermal conductivity state remains up to $\mathrm{T_m}$, reproducing the hysteresis observed in DSC and electrical conductivity experiments.

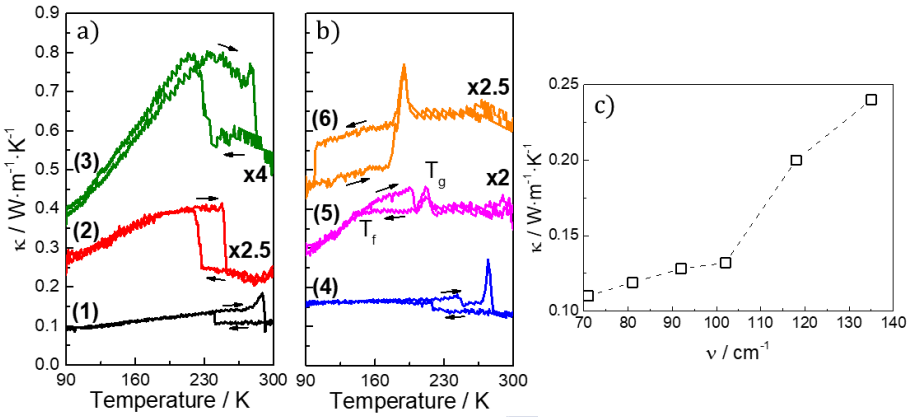

Figure 6.9: a-b) Temeperature dependence of κ for the ILs studied in this work. Temperature ramps were fixed to 1 K/min. The curves have been multiplied by a factor (indicated), for clarity. c) Thermal conductivity as a function of the H-bond strength, at T=300 K.

In the second group, large enough H-bond interactions frustrate the formation of an ionic crystal at low temperature, leading to a glass. This is reflected on κ, through a broad peak at T_g [149] and a flat temperature dependence in the solid phase. However, below T_f there is a sudden change in the temperature dependence of κ, and a subsequent appearance of a thermal hysteresis up to T_g. Note that IL **(6)** decreases its κ upon cooling, resulting in an inversion of the switching mechanism, which may be interesting to its application as thermal regulator.

This behavior suggests the formation of an ordered phase, either semicrystalline or liquid crystal, although it is not observable by X-ray diffraction. Thus to study the molecular arrangement at low temperatures, we follow the C-H stretching band for different temperatures (see Figure 6.10).

Ionic Liquid **(1)** shows a large change on the absorption upon crystallization, which reflects a large change in the dipole moment, due to the formation of new intermolecular bonds. However, for IL **(5)**, only a small change of the slope is observed at $\approx T_g$, discarding large structural changes.

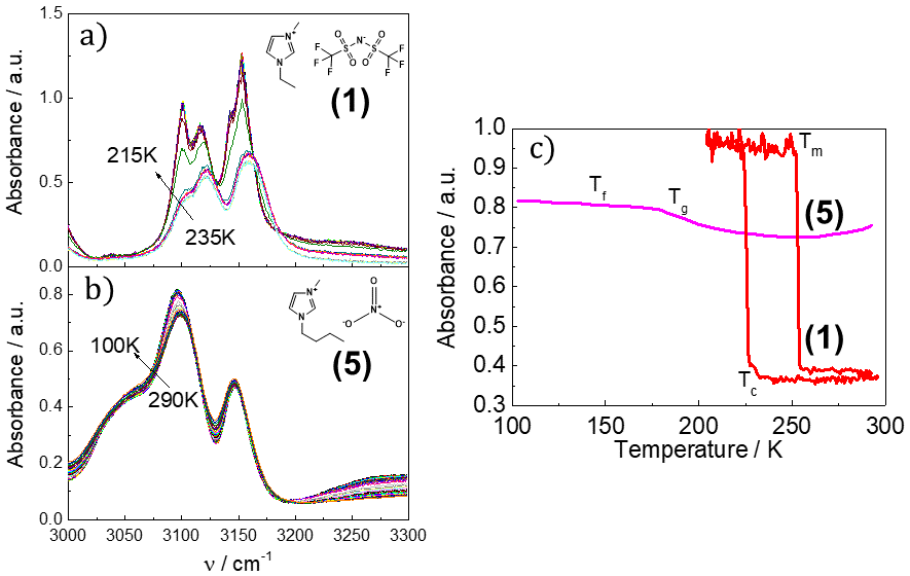

Figure 6.10: Temperature dependence of the C(2)-H IR stretching band for liquids **(1)** and **(5)**.

Taking together all these pieces of information, the most plausible hypothesis is the spontaneous formation of crystalline nuclei below T_f, whose volume fraction and size must be small enough to not being observable by X-ray scattering or give a large peak at the DSC. However, the formation of small crystals may generate stress fields and be the cause of the fractures observed in POM.

6.3 Effect of steric impediments

As mentioned before, a similar effect over the Coulomb potential is in principle expected from steric effects due to the presence of long alkyl chains attached to the imidazoliun ring. Actually, the introduction of large alkyl chains is known to hinder the formation of 3D crystals, leading to liquid crystalline meshophases [255, 256].

We analyzed the behavior of **(7)** 1-octyl-3-methylimidazolium hexafluorophosphate (MOIM-PF_6) and **(8)** 1-octyl-3-methylimidazolium bis(trifluoromethylsulfonyl)imide (MOIM-NTF_2), both with an 8-Carbon chain attached to one of the N of the imidazole ring, but moderate H-bond strength interaction (see Figure 6.11).

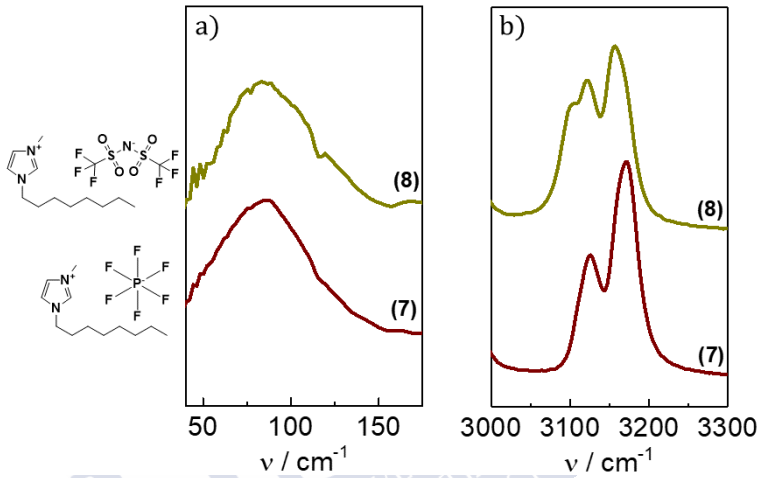

Figure 6.11: Far-FTIR (a) and mid-FTIR (b) spectra of the Im-ILs **(7)** and **(8)**. The far-IR band centered at ≈ 85 cm^{-1} is between ILs **(2)** and **(3)**.

Despite the weak H-bonds of these liquids, the steric hindrance introduced by the long alkyl chain results in a completely reversible liquid-to-glass transition, as it can be observed in DSC, electrical conductivity and cryo-IR experiments (see Figure 6.12). As in smaller ILs with stronger H-bonds, these experiments do not reveal any sign of the nucleation of small crystalline phases within the glass, at low temperatures.

Nevertheless, POM and thermal conductivity measurements show the same anomalies at low temperature reported for ILs **(4)**-**(6)**, that is, the fracture lines at T_f and the hysteresis in the thermal conductivity between T_f and T_g respectively (see Figure 6.13). Note, however, that the value of thermal conductivity at high temperature is highly dependent on the H-bond strength. For instance, the value of κ at room temperature

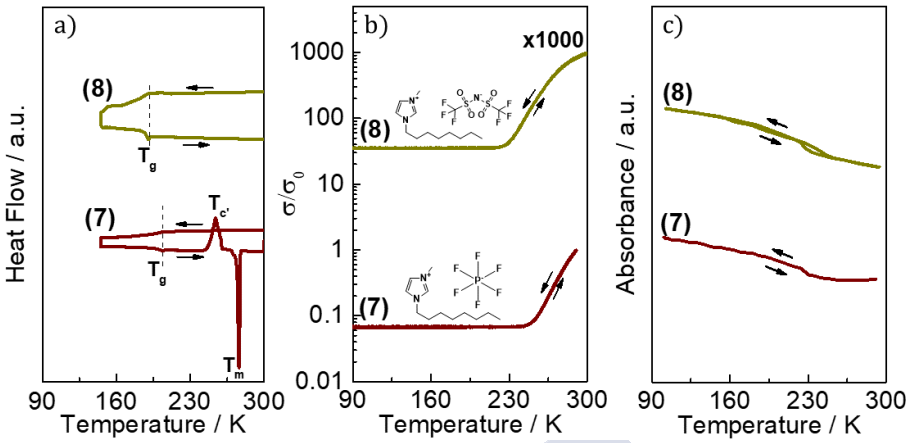

Figure 6.12: a) DSC thermogram, electrical conductivity (b) and mid-IR absorption (c) of ILs **(7)** and **(8)**. The experiments confirm the formation of a glassy state at low temperature, without additional transitions.

is $0.24\ \mathrm{W{\cdot}m^{-1}{\cdot}K^{-1}}$ for **(6)**, much larger than $\kappa \approx 0.14\ \mathrm{W{\cdot}m^{-1}{\cdot}K^{-1}}$ of ILs **(7)** and **(8)**.

These results confirm the equivalency between the perturbations to the Coulomb potential introduced by anion-cation H-bond interactions, and those induced by steric hindrance. If sufficiently relevant, these defects lead to the formation of a glass, which is unstable upon further cooling. This may be a general mechanism of a competition between anisotropic and isotropic force fields. The large difference between high and low κ states in these systems (up to 60%), produced between two solid phases, opens a new avenue in the design of thermal regulators, through a precise tuning of the energy landscape. This effect is perfectly reproducible, as we can perform several cycles around the hysteresis loop (see Figure 6.14).

To determine if the solid-to-solid transition is kinetically or thermodynamically driven, we compared the temperature dependence $\kappa(T)$ at different cooling rates (see Figure 6.15.a-b). The difference of κ between liquid and crystalline phases ($\Delta\kappa$) depends on the quality and extension of this phase. Thus, increasing the cooling rate impedes a

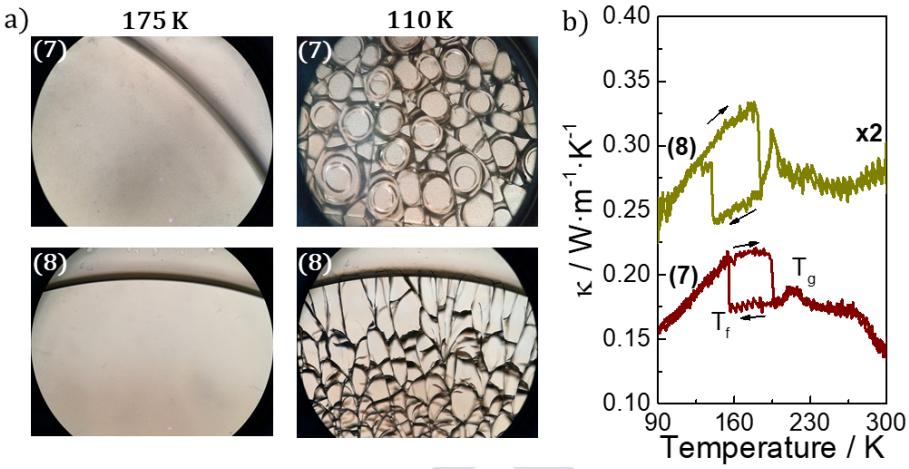

Figure 6.13: a) POM images before and after the formation of crystalline nuclei at T_f, leading to the fracture of the whole system. b) Dependence of κ with temperature for liquids **(7)** and **(8)**. Temperature ramps were fixed to 1 K/min. The curve for **(8)** has been multiplied by 2, for clarity.

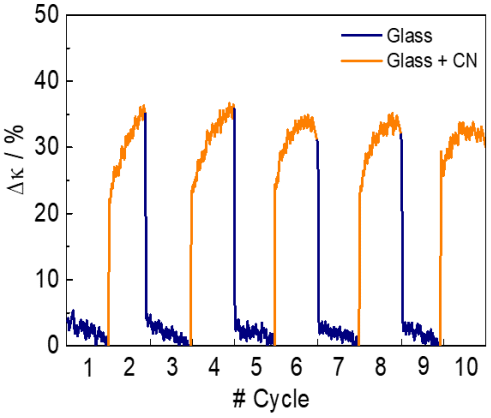

Figure 6.14: Reversible variation of the thermal conductivity after continuous cycling across T_f for liquid **(7)**. The cycles were carried out between 160 K and 190 K, with a temperature ramp of 1 K/min.

complete crystallization and, consequently, $\Delta\kappa$ decreases in **(2)**. However, the switching ratio at the solid-to-solid transition remains unaffected in **(7)**, in accordance with POM experiments (see videos in the Supplementary files in Ref. [62]). Thus, these results demonstrate that it is a thermodynamically driven process.

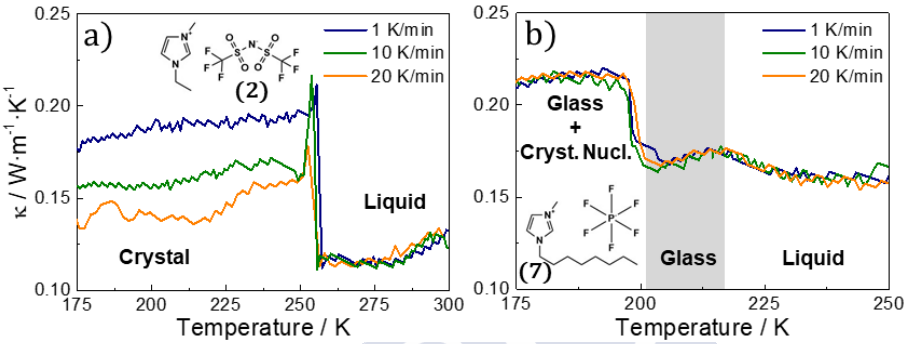

Figure 6.15: Temperature dependence of the thermal conductivity for a) EMIM-NTF_2 **(2)** and b) MOIM-PF_6 **(7)**. The measurements were performed during heating at 1 K/min, but after cooling the samples at different rates.

6.4 Effect of water

The hygroscopic character of ILs is a well known phenomena, which is associated to significant differences on their thermodynamic properties [257–263]. In previous sections, we have demonstrated that, introducing small perturbations to the Coulomb potential leads to large differences in phase diagram. Thus, it is expected that the presence of water, either by intentional addition or by unintentional, carefree use in humid atmosphere, could produce important differences in their low temperature crystallization [262].

To probe that, we performed DSC and thermal conductivity measurements for IL **(4)**, in the frontier between crystal and glass forming systems, as received, and after drying 18 hours at 100 °C under vacuum, at a pressure of 10^{-2} Torr. The amount of water was followed by

H-NMR, by measuring the liquid, which confirmed that the vacuum annealing reduces the water content ≈ 10 times, remaining stable during 1 day, at least (see Figure 6.16.a-b). Thus, we can ensure that the sample is stable during the measurements.

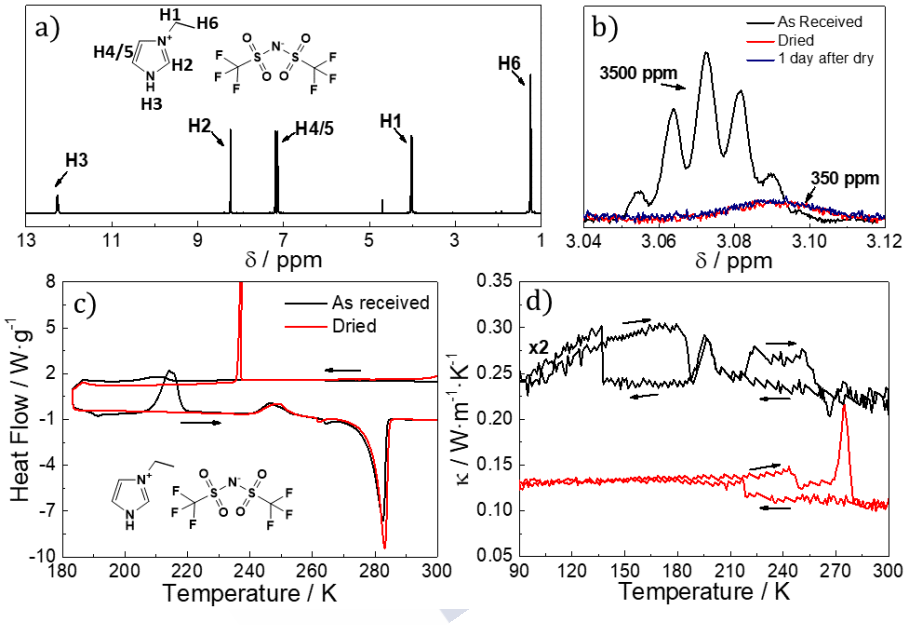

Figure 6.16: H-NMR of liquid **(4)** (a) and detail of the region around 3.07 ppm (b), showing the signal of water H-bonded to different the protons of the cation. DSC (c) and thermal conductivity (d) before and after drying.

As shown in Figure 6.16.c-d, the presence of water resembles the behavior of the ILs with strong H-bonds. The ILs as received show the formation of a glassy phase at low temperature, which is unstable upon further cooling. The crystalline nuclei formed at low temperature increase κ up to $\mathrm{T_g}$, where liquid values are recovered. These nuclei can grow on heating at ≈ 215 K, leading to an increase of κ and the subsequent thermal hysteresis. The dried liquid show κ and DSC consistent with conventional liquid-to-crystal transition, as discussed before.

These results demonstrate the relevance of water content to the liquid-to-solid phase transition. All the experiments reported previously in this chapter were performed in dried Im-ILs.

6.5 Light controlled heat transport regulation

As we have mentioned in the introduction of this chapter, azobenzene-based compounds are very promising materials to reach an effective control of κ, using light as an external-stimulus. The possibility of introducing different pending groups, the possibility of polymerizing them, and fast reversible light-induced structural changes, makes this family of molecular materials particularly suitable to control the heat transport by an external stimulus.

We synthesized 4,4'-Didecyloxy-3-methylazobenzene, following the procedure described in Ref. [248]. The transitions observed in DSC thermogram are in accordance with Norikane et al. [248] (see Figure 6.17.a). They identified a crystal-to-liquid crystal (nematic) phase transition at T(Cr-LC), which melts at T(LC-I). This process is completely reversible upon cooling, showing the expected thermal hysteresis.

The temperature dependence of κ (Figure 6.17.b) shows that the thermal conductivity is particularly low in the intermediate mesophase, between the crystal (low temperature) and the isotropic liquid (high temperature).

It is worth noting that the thermal conductivity of the liquid crystalline phase shows a large variation with temperature, probably related with the increasing mobility at higher temperature, as molecules can be reoriented, forming larger nematic domains and, consequently, enhancing the heat transport. This hypothesis also explains the higher κ of the LC upon cooling, as the higher mobility of the liquid phase permits a more favorable arrangement of the azobenzene molecules.

On the other hand, the lower κ of the liquid crystal (LC), in comparison with the isotropic liquid, suggests a possible increase of the molar volume [28], as κ decreases by increasing the intermolecular dis-

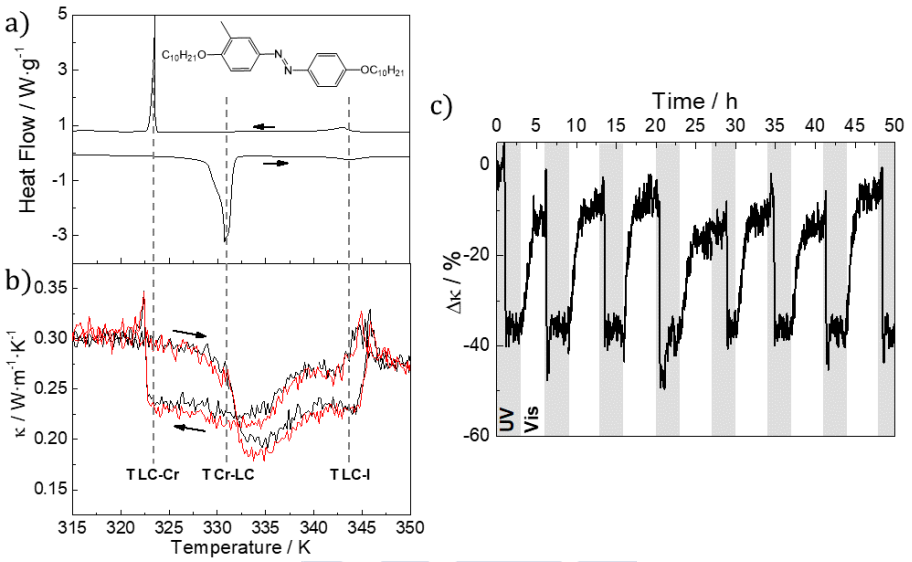

Figure 6.17: a) DSC thermograms of 4,4'-Didecyloxy-3-methylazobenzene. b) Dependence of κ with the temperature. We perform two cycles (black and red) to confirm the reproducibility of the results. c) Thermal conductivity variation under illumination at two wavelengths: UV (350 nm) and Vis (450 nm). The measurement was performed at 320 K. The irradiance is $\approx 10\ \mathrm{mW \cdot cm^{-2}}$ [264].

tance (see Introduction Chapter). The arrangement of large azobenzene molecules within a nematic matrix leads to an increase of the intermolecular distance and, consequently, the thermal conductivity. This situation does not occur in the liquid phase, where the molecules can be accommodated in random orientations, minimizing the distance between neighbors.

Finally, we measured κ at a constant temperature (320 K), after illuminating with UV (350 nm) and visible (450 nm) light. Irradiating this compound with UV light produces a trans-to-cis isomerization of the azobencene group, and leads to a liquefaction of the crystalline phase [248]. However, there is higher than expected $\Delta\kappa$, up to 40%, much larger than the 10% difference between the solid and liquid phases

induced thermally. The different geometry of cis and trans isomers must produce different interactions in the cis/trans liquid, which must be at the origin of this behavior.

These results demonstrate (again) the extremely high sensitivity of the thermal conductivity to changes on the molecular arrangement. The possibility to control the heat transport by an external stimulus and close to room temperature, and the large $\Delta\kappa$ of this system, are important advantages over the ILs showed previously.

6.6 Summary

In this chapter we have used thermal conductivity as a tool to characterize liquid-to-solid phase transitions in Ionic Liquids, engaged by the possibility of use these systems as thermal regulators. Our results demonstrate that the perturbation introduced by directional H-bonds into the isotropic Coulomb potential affects strongly the formation of crystalline, liquid-crystalline or glassy phases at low temperature, which can be summarized in the phase diagram showed in Figure 6.18.

Increasing the strength of H-bonds frustrates, progressively, the formation of crystalline solids (3D order), leading to the formation of liquid-crystalline phases (2D order) and, finally, the formation of a glass. This glassy phase is thermodynamically unstable upon further cooling, and the formation of small crystalline nuclei within the system results in an unexpected variation of the thermal conductivity. Importantly, this large thermal contrast remains up to the glass temperature, opening a large region of temperatures (up to 75 K) where the thermal conductivity can be reversibly switched between two solid states, with differences up to 35-40%.

Furthermore, this behavior can be reproduced by introducing other types of perturbations, like steric hindrance or the addition of water. Thus, these results suggest a new approach for the design of thermal regulators, through a careful control of the contribution of defects to the Coulomb potential of ionic liquids.

As a prospective work, we showed an example of an azobenzene based system, where the irradiation with UV light leads to a solid-to-liquid phase transition. This results in a large thermal conductivity contrast, with the important advantage that it is produced at constant temperature and through an external stimulus.

Finally, I would like to mention the possibility of mixing azobenzene-based compounds and ILs: the light-responsive molecule can be used to destabilize the mesophases of the IL, reaching large thermal contrasts. The wide variety and properties of both compounds open a new avenue for the design of effective thermal regulators, with unforeseen applications. We continue working in this direction, and we hope that our results stimulate further experimental and theoretical work.

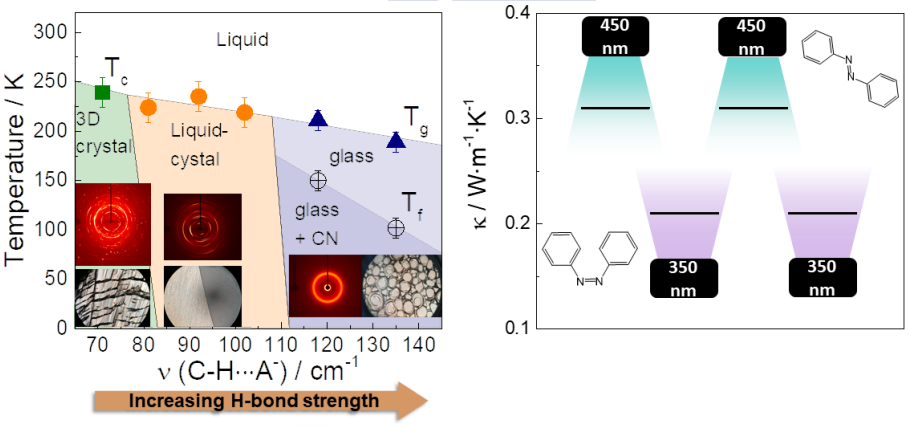

Figure 6.18: Graphical summary of the main results obtained in this chapter. Increasing H-bond strength in Im-ILs leads to a progressive loss of 3D crystalline order, resulting in a large thermal contrast. Similar thermal conductivity switching can be achieved using azobenzene-based systems, with the important advantage that they can be externally controlled, at a constant temperature.

USC
UNIVERSIDADE
DE SANTIAGO
DE COMPOSTELA

Concluding remarks and outlook

The main conclusion of this thesis is the possibility of using the thermal conductivity as a complementary tool for the analysis of the molecular arrangement in liquids. This opens a new strategy for the study of fluids, where the combination of strong interactions and large mobility makes difficult their understanding. It is worth noting that the analysis and results presented in this thesis clearly show the connection between the macroscopic heat transport and the microscopic environment.

Using this novel strategy, we have analyzed different liquid systems, leading to very interesting results. In the following, we highlight the most general conclusions of each chapter:

- We have demonstrated that the addition of small amounts of ethanol produces an enhancement of the energy transfer rate. The rearrangement of water molecules around the hydrophobic chain favors the formation of ice-like structures and, consequently, an increase of the thermal conductivity. This anomalous effect is only possible in alcohols, where the water-like OH group allows the accommodation of these molecules into the tetrahedral network of water. Finally, this effect is progressively destroyed by increasing the length of the hydrophobic chain.

- We have shown that dissolving non-polar molecules in water can lead to the formation of supramolecular structures, if the hydrophobic contribution is sufficiently strong. This effect was

demonstrated to be characteristic of the family of tetrabutylammonium salts, as well as other pnictogen cations with four butyl chains. The supramolecular structure formed in these systems is highly incompressible, and presents a high reduction of the thermal diffusivity. Furthermore, they are similar to the clathrate hydrates formed at low temperature, which suggest the possibility of using these liquids as sequestering agents in chemical reactions, with unforeseen applications in energy storage.

- We have demonstrated the high sensitivity of heat diffusion to different types of phase transitions. Measuring the thermal conductivity, we show the formation of different crystalline or liquid crystalline phases, in a series of imidazolium based ionic liquids. The formation of the different low temperature phases is determined by the strength of the H-bonds formed between the anion and the cation. This effect can be reproduced by introducing steric hindrance, increasing the length of the radical groups attached to the imidazolium ring.

- The large difference of the thermal conductivity across phase transitions in ILs is suitable for their use as thermal regulators. Importantly, we have shown the formation of crystalline structures within the glassy phase, which results in a 35% change of the thermal conductivity between two solid phases.

- Azobenzene based compounds are promising materials for an effective control of the thermal conductivity. The conformational change of these molecules leads to a solid-to-liquid phase transition upon illumination with a UV light. This produces an important 40% reduction of the thermal conductivity, controlled by an external stimulus.

Despite the relevance of the results presented in this thesis, the most important contribution is the possibility of using the heat transport as an alternative tool for the study of complex systems. This can shed light into the wide variety of interesting phenomenology present in liquids.

Moreover, the possibility of designing active thermal regulators by using light sensitive compounds are very promising. We will continue working further in this direction, and we hope that our discovers stimulate further experimental and theoretical research.

USC
UNIVERSIDADE
DE SANTIAGO
DE COMPOSTELA

Summary in Galician/ Resumo en Galego

Comprender a estrutura dinámica dos líquidos é fundamental, xa que supón a base da gran maioría das reaccións químicas, moitas delas fundamentais para a vida. Este feito atraeu a atención dos máis prestixiosos científicos da área, coma por exemplo Faraday, o premio Nobel L. Landau ou J. Ziman. Porén, a complexidade destes sistemas impediu o desenvolvemento dunha teoría que fose quen de explicar a fenomenoloxía observada experimentalmente.

Por unha parte, os líquidos contan con interaccións intermoleculares suficientemente fortes para que as súas moléculas poidan ser tratadas de xeito individual (coma nos gases). Por outra parte, as grandes flutuacións estruturais impiden que poidamos estudar unicamente unha cantidade pequena de moléculas e extrapolar os resultados a todo o sistema, coma nos sólidos.

Durante as últimas décadas, e especialmente durante os últimos anos, o desenvolvemento de técnicas experimentais de alta resolución e o incremento da potencia dos computadores permitiron o descubrimento de numerosas propiedades descoñecidas dos materiais, con importantes aplicacións en diferentes campos. Sen embargo, este importante avance non se viu reflexado de xeito tan directo nos líquidos, onde se produce un avance máis lento. O ordenamento das moléculas mantense, en xeral, durante períodos moi curtos de tempo (femtosegundos), e só pode ser estudado a partir de técnicas de alta resolución, ou a través

de complexas simulacións que requiren de elevados tempos computacionais.

O principal obxectivo desta tese é amosar que o estudo do transporte da calor en líquidos supón unha nova ferramenta para tratar de avanzar neste eido. Dentro da física do estado sólido, é moi coñecida a enorme sensibilidade da condutividade térmica a cambios no ordenamento molecular. Porén, esta estratexia nunca foi utilizada no estudo da estrutura dinámica dos líquidos. Este obxectivo vén motivado polo feito de que a calor se transporta a través do acoplamento vibracional das moléculas, cun tempo característico moi pequeno, tamén da orde de femtosegundos.

Analizando de xeito teórico o transporte da calor en líquidos vese que depende de tres variables: a enerxía das excitacións térmicas que transportan a calor (capacidade calorífica), a súa velocidade (velocidade do son) e o camiño libre medio. Estas dúas últimas poden ser expresadas en función da distancia intermolecular e da rixidez do sistema, obtendo que a condutividade térmica aumenta coa fortaleza das interaccións intermoleculares, sendo máis efectiva a distancias menores.

A pesar de que nos líquidos existe un mecanismo adicional de transferencia de calor, causada por colisións entre as moléculas, este é moito máis lento que a transmisión das vibracións. Por exemplo, o tempo que tarda unha molecular en moverse unha distancia intermolecular é dúas ordes de magnitude maior que o que tarda en transmitirse a vibración, polo que este mecanismo é despreciable.

É importante destacar a conexión que se establece entre unha propiedade macroscópica e a estrutura a nivel molecular, a través da medida da condutividade térmica. Esta conexión permite o deseño de sistemas con aplicacións en campos moi variados, como poden ser a biotecnoloxía ou o almacenamento de enerxía.

Nesta tese preséntanse algunhas posibles aplicacións desta estratexia, demostrando a gran sensibilidade da condutividade térmica a cambios no ordenamento local das moléculas. Exemplo disto é a demostración da formación de estruturas ordenadas na auga cando se disolven pequenas cantidades de alcois de pequeno tamaño, o que incrementa a velocidade de transferencia da enerxía.

Un incremento da hidrofobicidade do soluto conduce á formación de superestruturas, en disolucións de bromuro de tetrabutilamonio ou tetrabutilfosfonio. As estruturas formadas, que son moi similares aos clatratos formados a baixa temperatura, permiten encapsular pequenas moléculas non polares, o que pode ter importantes aplicacións no almacenamento de enerxía, ou como axentes secuestradores en reaccións químicas.

Por outra parte, a sensibilidade do transporte da calor a cambios na estrutura permite a detección de transicións de fase, así coma a formación de pequenas estruturas cristalinas que non poden ser detectadas por outras técnicas. O gran cambio da condutividade térmica que se produce nestas transicións permite a súa aplicación como reguladores térmicos, onde o transporte da calor pode ser controlado ao gusto. Estudando as transicións de fase en diferentes líquidos iónicos, obtivérsonse diferencias de ata o 60%. Ademais, demostrouse que o rango de funcionamento destes sistemas depende fortemente da fortaleza das pontes de hidróxeno formadas entre anión e catión.

Este control da condutividade térmica prodúcese de xeito pasivo, sendo causado por un cambio na temperatura. O seguinte reto é lograr un cambio similar mediante un estímulo externo, que pode ser un campo electromagnético ou a aplicación da luz. Esta segunda estratexia é a que se tratou de seguir nesta tese, empregando compostos baseados nos azobencenos, que son sensibles á luz en diferentes lonxitudes de onda. Con isto lograrouse obter unha baixada da condutividade térmica de ata o 40%.

Técnicas experimentais

Nesta tese, deseñouse e implementouse un novo sistema para a medida da condutividade térmica en líquidos, mediante unha variación do método 3ω, desenvolvido orixinariamente por D. Cahill para a medida de sólidos e películas delgadas. Este método emprega o autoquecemento producido cando aplicamos unha corrente AC a través dunha liña metálica, depositada sobre a superficie da mostra de interese. Este auto-

quecemento xera unha voltaxe a tres veces a frecuencia de entrada ($V_{3\omega}$), que depende da difusividade térmica do entorno, segundo se obtén da resolución da ecuación de calor.

A voltaxe 3ω depende de xeito lineal co logaritmo da frecuencia de entrada, cuxa pendente é inversamente proporcional á condutividade térmica do substrato. Cando depositamos unha gota dun líquido (ou outro sólido) enriba da resistencia, a calor propágase tanto a través do sólido coma do líquido. Empregando a mesma estratexia de medida resulta nunha condutividade térmica efectiva que é a suma de ambas. Polo tanto, a condutividade térmica do líquido pode ser calculada a partir da dependencia da $V_{3\omega}$ coa frecuencia, medindo previamente o valor do substrato empregado.

A pesar de que a medida do transporte da calor xoga un papel fundamental no desenvolvemento desta tese, foi necesario empregar diferentes técnicas experimentais e metodoloxías, co obxectivo de relacionar os cambios producidos a nivel molecular cos cambios observados na condutividade térmica.

En primeiro lugar, a determinación das diferentes transicións de fase, así coma a medida da capacidade calorífica dos diferentes líquidos, realizouse empregando a técnica da Calorimetría Diferencial de Barrido (DSC). Esta técnica mide a enerxía precisa para elevar a temperatura dun composto, é dicir, a súa capacidade calorífica. Cando o sistema pasa a través dunha transición de fase, isto reflíctese nun pico cuxa dirección depende de se o proceso é exotérmico ou endotérmico. Isto permite a detección das transicións de fase, así como a súa caracterización.

Porén, esta técnica non permite diferenciar, de xeito sinxelo, entre unha transición líquido-cristal ou líquido-cristal-líquido, xa que teñen enerxías asociadas similares. Esta diferenciación é fundamental no estudo da transición líquido-sólido nos líquidos iónicos, xa que é coñecido que moitos destes compostos poden formar mesofases. Con este propósito empregouse a Microscopía de Luz Polarizada (POM).

Se un feixe de luz incide sobre dous polarizadores cuxos eixos ópticos se atopan perpendiculares, a compoñente da luz que é capaz de pasar polo primeiro polarizador é detida polo segundo, o que provoca que a luz non sexa quen de atravesalos. Porén, se entre ambos polar-

izadores se introduce un medio anisótropo, a luz polarizada que sae do primeiro ve afectado o seu estado de polarización, polo que unha parte da mesma pode atravesar o segundo polarizador e, polo tanto, verse a través dun microscopio. Deste xeito pódese identificar a presenza dun material anisótropo, unha das propiedades máis características dos cristais líquidos.

Por outra parte, cando un feixe de luz atravesa un material é parcialmente absorbida. Da física cuántica sabemos que un sistema só absorbe radiación dunhas frecuencias características, que se relaciona cos diferentes modos vibracionais e rotacionais das súas moléculas. Estes modos poden caracterizarse a través da Espectroscopía Infravermella (IR). Mediante a técnica da transformada de Fourier (FTIR), pódense determinar as frecuencias de absorción características de cada sistema e, con isto, comprender a fortaleza e o tipo de interaccións, tanto inter coma intramoleculares.

Como se viu anteriormente, dous dos parámetros que afectan á propagación da calor son a velocidade do son e a distancia intermolecular, é dicir, a densidade. Por este motivo, ao longo desta tese realizáronse numerosas medidas de ambas magnitudes, permitindo deste xeito unha análise detallada da condutividade térmica.

Finalmente, tamén se realizaron medidas da viscosidade e de Resonancia Magnética Nuclear (RMN). Estas técnicas empregáronse para confirmar a formación de estruturas supramoleculares nas disolucións acuosas de bromuro de tetrabutilamonio, observando unha diminución na difusión do bromo maior do agardado.

Resultados e conclusións

Transporte térmico en mesturas de auga e alcohol

Esta parte do traballo centrouse en analizar o transporte térmico en mesturas de auga e alcohol, co principal obxectivo de comprobar se a condutividade térmica era sensible ou non a cambios no ordenamento molecular. É coñecido que disolver moléculas orgánicas, coas súas cadeas hidrofóbicas, ten un gran efecto na rede de pontes de hidróxeno

característica da auga. Isto tradúcese nun gran número de anomalías nas propiedades termodinámicas da auga, especialmente para concentracións moi pequenas.

Diferentes traballos previos suxeriron que estas anomalías son provocadas pola formación de estruturas ordenadas arredor das cadeas hidrofóbicas, no coñecido como "modelo de iceberg". Segundo este modelo, as propiedades da auga non se ven afectadas máis alá da primeira esfera de hidratación, o que entra en contradición cos resultados obtidos mediante experimentos de espectroscopía de alta resolución ou con cálculos de dinámica molecular.

Para tratar de resolver esta controversia, os alcois pequenos resultan particularmente axeitados, xa que contan cunha parte hidrofílica, que pode formar pontes de hidróxeno coa auga, e unha parte hidrofóbica, cuxo tamaño pode ser cambiado de xeito sistemático. Os resultados obtidos demostran que ambas partes xogan un papel na formación de estruturas ordenadas no rango de concentracións baixas.

Desenvolveuse un modelo moi simple para a condutividade térmica, que reproduce os datos experimentais para diferentes disolucións acuosas. Este modelo permitiunos identificar o rango de concentracións no que se forman estas estruturas ordenadas arredor da cadea hidrofóbica. Estas estruturas teñen un tempo de vida similar ao tempo de difusión térmica, producindo un inesperado incremento na condutividade térmica destes sistemas.

Por outra parte, realizouse unha comparación con outras moléculas orgánicas, empregando outros grupos hidrofóbicos. Os resultados obtidos apuntan cara un papel fundamental do grupo OH dos alcois. A súa semellanza cos grupos OH da auga permite que se acomode na estrutura tetraédrica da auga o que, unido a un reordenamento arredor da cadea hidrofóbica, produce un aumento na condutividade térmica.

Este feito pode ser comprendido dentro do modelo dos dous tipos de auga, onde se propón que a auga está formada por dúas estruturas: unha de baixa densidade e ordenada, similar ao xeo; e outra desordenada e de alta densidade. Ambos tipos conviven en equilibrio na auga pura, o que explica as diferentes anomalías observadas, como o máximo na densidade e na capacidade calorífica, ou o mínimo na compresibili-

dade. A incorporación de alcois de cadea pequena na estrutura da auga afecta a este equilibrio, desprazándoo cara maiores concentracións de auga estruturada e, polo tanto, aumentando a efectividade do transporte de enerxía.

Clatratos fundidos: unha nova familia de líquidos supramoleculares

Este capítulo céntrase na discusión do efecto de disolver moléculas con grandes cadeas hidrofóbicas, cuxa disposición sexa simétrica arredor do átomo central. Para isto estudouse a familia de moléculas baseadas nos grupos alquilamonio e alquilfosfonio.

É moi coñecido que, cando se mesturan coa auga, estes compostos forman sólidos cristalinos a baixas temperaturas ou altas presións, coñecidos como clatratados hidratados. Nestes sistemas, a auga ordénase arredor da molécula hidrofóbica, deixando ocos que poden albergar pequenas moléculas non polares. Este feito resulta de especial interese en aplicacións coma o almacenamento de hidróxeno ou a separación de gases. Ademais, a fusión destas estruturas atópase detrás das explosións de gas en Siberia, liberando unha importante cantidade de metano e outros gases, o que supón unha importante contribución ao cambio climático.

Tendo en conta os resultados obtidos no capítulo anterior, onde a presenza das cadeas hidrofóbicas coordinaba un elevado número de moléculas de auga, resulta interesante preguntarse acerca das propiedades fisicoquímicas destes clatratos, cando se atopan na fase líquida. Seguindo a mesma estratexia que no capítulo anterior, realizáronse medidas do transporte da calor, comparándoas coa compresibilidade adiabática e o espectro IR. Os resultados obtidos suxiren a formación de estruturas ordenadas arredor dos catións, coordinando un elevado número de moléculas de auga. Estas estruturas aseméllanse moito aos clatratos que se forman a baixa temperatura ou alta presión.

Para confirmar estes resultados, realizáronse medidas de RMN para caracterizar a difusividade do anión. Os resultados obtidos confirman a presenza destas estruturas na fase líquida, observándose un aumento

da difusividade que non pode ser explicado por un aumento da viscosidade. Este resultado é compatible coa inclusión do anión na estrutura formada, polo que apunta na mesma dirección que os resultados anteriores. Dado o tamaño destas estruturas, involucrando da orde de 36 moléculas de auga, acuñamos estes líquidos co nome de "*líquidos supramoleculares*". As propiedades destes sistemas permiten pensar en importantes aplicacións, coma o almacenamento de enerxía ou o seu uso como axentes secuestradores nas reaccións químicas.

Condutividade térmica a través de transicións de fase sólido-líquido

Como se mencionou na introdución deste resumo, un dos obxectivos desta tese é o deseño e análise de sistemas que permitan un control efectivo do trasporte da calor, os chamados reguladores térmicos. Estes dispositivos poden definirse como sistemas con dous estados térmicos, de alta e baixa condutividade térmica, que permiten saltar dun a outro estado segundo sexa preciso.

Este reto centrou os esforzos dos máis prestixiosos grupos de investigación nos últimos anos, para o que se seguiron diferentes estratexias. A gran maioría destes dispositivos aprovéitanse da diferenza de condutividade térmica que acontece cando o sistema pasa a través dunha transición de fase, que é inducida térmicamente. O maior reto neste eido consiste en aumentar a diferenza de condutividade entre ambos estados, onde destaca a inclusión de partículas de grafito ou nanotubos de carbono.

A este respecto, o uso de líquidos iónicos tamén resulta particularmente interesante, xa que mostran un amplo rango de temperaturas de cristalización/fusión, o que permite seleccionar o rango de temperaturas óptimo para cada aplicación en particular. Estas temperaturas veñen determinadas polas interaccións entre o anión e o catión, polo que o seu estudo resulta fundamental.

Neste capítulo analizamos en detalle os diferentes tipos de interacción presentes nos líquidos iónicos, demostrando que a perturbación introducida polos enlaces de hidróxeno no potencial de Coulomb de-

termina en gran medida o tipo de sólido formado a baixa temperatura. Aumentar a fortaleza destas pontes de hidróxeno frustra, de xeito progresivo, a formación de cristais ordenados nas tres dimensións, pasando polos cristais líquidos (orde 2D) ata chegar aos vidros.

Sorprendentemente, a formación de pequenos núcleos de cristalización na fase vítrea produce un gran aumento da condutividade térmica, o que permite unha variación da mesma entre dúas fases sólidas. Este comportamento pode ser reproducido introducindo outro tipo de perturbacións, como os impedimentos estéricos ou a adición de auga, o que suxire un mecanismo xeral.

A utilización das transicións de fase inducidas térmicamente conta coa desvantaxe de ser un control pasivo. Unha vez caracterizados estes sistemas, o seguinte paso é lograr o control activo da condutividade térmica. Para isto existen diferentes estratexias, entre as que destaca o uso de moléculas sensibles á luz. Con este obxectivo empregamos compostos baseados en azobencenos, onde logramos unha baixada na condutividade térmica do 40%, producida pola iluminación con luz ultravioleta.

Este resultado, unido á posibilidade de mesturar estas moléculas cos líquidos iónicos e aproveitar as vantaxes de ambos, abre unha nova posibilidade para o deseño de reguladores térmicos, que contan con importantes aplicacións en eidos como o almacenamento de enerxía ou os dispositivos fonónicos.

Conclusións xerais

A posibilidade de utilizar a condutividade térmica como unha nova técnica para o análise da estrutura dos líquidos é a principal conclusión desta tese. Isto abre unha nova estratexia para o estudo de líquidos, demostrando a forte conexión existente entre unha propiedade macroscópica de transporte e o entorno microscópico. Utilizando esta técnica novidosa, caracterizamos diferentes sistemas, cuxos principais resultados se destacan a continuación:

- Demostrouse que a adición de pequenas cantidades de etanol produce un aumento na velocidade de transferencia de enerxía. O reordenamento das moléculas arredor da cadea hidrofóbica favorece a formación de estruturas tetraédricas, similares ás do xeo, o que produce un aumento da condutividade térmica. Este efecto anómalo só é posible en alcois, onde a semellanza do seu grupo OH- coa auga permite que a molécula de alcol se incorpore á estrutura tetraédrica. Este efecto desaparece de xeito progresivo ao aumentar a lonxitude da cadea hidrofóbica.

- Amosouse que disolver moléculas non polares en auga pode conducir á formación de estruturas supramoleculares, no caso de que a interacción hidrofóbica sexa suficientemente forte. Este efecto é característico da familia das sales de tetrabutilamonio, así coma de outras sales similares. A estrutura formada é altamente incompresible, e presenta unha importante redución da difusividade térmica. Ademais, a súa semellanza coas estruturas formadas na fase sólida, os clatratos, permite o seu uso coma axentes secuestradores en reaccións químicas, con aplicacións inéditas no almacenamento da enerxía, por exemplo.

- Demostrouse a elevada sensibilidade da difusión da calor a diferentes tipos de transicións de fase. Medindo a condutividade térmica, puidemos determinar a formación de diferentes fases sólidas, nunha serie de líquidos iónicos. A fase formada a baixa temperatura vén determinada pola fortaleza das pontes de hidróxeno formadas entre o anión e o catión, efecto que pode ser reproducido introducindo calquera tipo de defecto ao potencial de Coulomb.

- A gran diferenza de condutividades que se produce ao pasar a través dunha transición de fase facilita o uso dos líquidos iónicos como reguladores térmicos. É importante destacar que a formación de pequenos núcleos de cristalización na fase vítrea resulta nun incremento do 35% da condutividade térmica, entre dúas fases sólidas.

- Os compostos baseados nos azobencenos resultan moi prometedores na busca de sistemas que permitan un control activo da condutividade térmica. O cambio conformacional que se produce nestas moléculas cando son iluminadas con luz ultravioleta conduce a unha transición de fase sólido-líquido, o que reduce un 40% a condutividade térmica, mediante un estímulo externo.

A pesar da relevancia dos resultados obtidos, a contribución máis importante desta tese é a comprobación de que a análise do transporte da calor resulta unha ferramenta alternativa para o estudo de sistemas complexos. Isto pode axudar a comprender de xeito máis profundo a gran variedade de fenómenos presentes nos líquidos, con aplicacións descoñecidas ata o momento.

Por outra parte, a posibilidade de controlar de xeito activo a condutividade térmica usando compostos sensibles á luz é realmente prometedora. Continuaremos traballando nesta dirección, e desexamos que os nosos descubrimentos estimulen novas investigacións, tanto dende un punto de vista teórico coma experimental.

USC
UNIVERSIDADE
DE SANTIAGO
DE COMPOSTELA

Bibliography

[1] M. Faraday. VI. experimental researches in electricity.-seventh series. *Philosophical Transactions of the Royal Society of London*, 124:77–122, 1834.

[2] L. D. Landau and E. M. Lifshitz. *Statistical Physics*. Pergamon Press: Oxford, 1969.

[3] J. M. Ziman. *Models of Disorder*. Cambridge University Press, 1979.

[4] D. Bolmatov, V. V. Brazhkin, and K. Trachenko. The phonon theory of liquid thermodynamics. *Scientific Reports*, 2:1–6, 2012.

[5] K. Trachenko. Heat capacity of liquids: An approach from the solid phase. *Physical Review B - Condensed Matter and Materials Physics*, 78(10):1–7, 2008.

[6] V. V. Brazhkin and K. Trachenko. Collective excitations and thermodynamics of disordered state: New insights into an old problem. *Journal of Physical Chemistry B*, 118(39):11417–11427, 2014.

[7] K. Trachenko and V. V. Brazhkin. Collective modes and thermodynamics of the liquid state. *Reports on Progress in Physics*, 79(1):16502, 2015.

[8] M. E. Ritchie. Reaction and diffusion thermodynamics explain optimal temperatures of biochemical reactions. *Scientific Reports*, 8(1):11105, 2018.

[9] J. A. Malen and V. Viswanathan. Regulating hot and cold. *Nature Energy*, 3(10):826–827, 2018.

[10] J. H. Cho, C. D. Richards, and R. F. Richards. A facility for characterizing the steady-state and dynamic thermal performance of microelectromechanical system thermal switches. *Review of Scientific Instruments*, 79(3), 2008.

[11] M. Gumus. Reducing cold-start emission from internal combustion engines by means of thermal energy storage system. *Applied Thermal Engineering*, 29(4):652–660, 2009.

[12] M. Dietrich, A. Euler, and G. Thummes. A compact thermal heat switch for cryogenic space applications operating near 100 K. *Cryogenics*, 59:70–75, 2014.

[13] G. Wehmeyer, T. Yabuki, C. Monachon, J. Wu, and C. Dames. Thermal diodes, regulators, and switches: Physical mechanisms and potential applications. *Applied Physics Reviews*, 4(4):793, 2017.

[14] R. Strang and J. Patterson. The role of thermal conduction in hyperthermia. *International Journal of Radiation Oncology*Biology*Physics*, 6(6):729–735, 1980.

[15] J. M. Ziman. *Electrons and Phonons. The Theory of Transport Phenomena in Solids*. Oxford University Press, 1960.

[16] P. W. Bridgman. The thermal conductivity of liquids under pressure. *Proceedings of the American Academy of Arts and Sciences*, 59(7):141–169, 1923.

[17] D. Bolmatov and K. Trachenko. Liquid heat capacity in the approach from the solid state: Anharmonic theory. *Physical Review B - Condensed Matter and Materials Physics*, 84(5):54106, 2011.

[18] Y. A. Çengel, J. M. Cimbala, and Turner R. H. *Fundamentals of Thermal-Fluid Sciences*. McGraw-Hill, 5th edition, 2005.

[19] F. Rivadulla. *Termodinámica estadística y fenómenos de transporte*. Universidad de Santiago de Compostela, 2017.

[20] T. Engel and P. Reid. *Química Física*. Pearson, 2006.

[21] F. W. Sears and G. L. Salinger. *Thermodynamics, Kinetic Theory, and Statistical Thermodynamics*. Addison-Wesley, 3rd edition, 1975.

[22] T. Iwashita, D. M. Nicholson, and T. Egami. Elementary excitations and crossover phenomenon in liquids. *Physical Review Letters*, 110(20), 2013.

[23] T. Iwashita and T. Egami. Local energy landscape in a simple liquid. *Physical Review E - Statistical, Nonlinear, and Soft Matter Physics*, 90(5):1–10, 2014.

[24] T. Egami and Y. Shinohara. Correlated atomic dynamics in liquid seen in real space and time. *Journal of Chemical Physics*, 153(18), 2020.

[25] M. Huber and A. Harvey. *Thermal Conductivity of Gases*. CRC-Press, Boca Raton, FL, 92nd edition, 2011.

[26] E. Langenberg, E. Ferreiro-Vila, V. Leborán, A. O. Fumega, V. Pardo, and F. Rivadulla. Analysis of the temperature dependence of the thermal conductivity of insulating single crystal oxides. *APL Materials*, 4(10), 2016.

[27] L. Qun-Fang, L. Rui-Sen, N. Dan-Yan, and H. Yu-Chun. Thermal conductivities of some organic solvents and their binary mixtures. *Journal of Chemical and Engineering Data*, 42(5):971–974, 1997.

[28] C. López-Bueno, D. Bugallo, V. Leborán, and F. Rivadulla. Sub-μL measurements of the thermal conductivity and heat capacity of liquids. *Phys. Chem. Chem. Phys.*, 20:7277–7281, 2018.

[29] V. Murashov and M. A. White. *Thermal Conductivity of Insulators and Glasses*, pages 93–104. Springer US, Boston, MA, 2004.

[30] J. Frenkel. *Kinetic Theory of Liquids*. Oxford University Press, 1947.

[31] O. L. Anderson. A simplified method for calculating the debye temperature from elastic constants. *J. Phys. Chem. Solids*, 24:909–917, 1963.

[32] S. Woutersen, U. Emmerichs, and H. J. Bakker. Femtosecond mid-IR pump-probe spectroscopy of liquid water: Evidence for a two-component structure. *Science*, 278(5338):658–660, 1997.

[33] S. Woutersen and H. J. Bakker. Resonant intermolecular transfer of vibrational energy in liquid water. *Nature*, 402(6761):507–509, 1999.

[34] S. Y. Willow, M. A. Salim, K. S. Kim, and S. Hirata. Ab initio molecular dynamics of liquid water using embedded-fragment second-order many-body perturbation theory towards its accurate property prediction. *Scientific Reports*, 5:14358, 2015.

[35] A. Benedetto and G. J. Kearley. Elastic scattering spectroscopy (ESS): An instrument-concept for dynamics of complex (Bio-) systems from elastic neutron scattering. *Scientific Reports*, 6, 2016.

[36] T. Iwashita, B. Wu, W. R. Chen, S. Tsutsui, A. Q. R. Baron, and T. Egami. Seeing real-space dynamics of liquid water through inelastic x-ray scattering. *Science Advances*, 3(12):1–7, 2017.

[37] D. G. Cahill. Thermal conductivity measurement from 30 to 750 K: the 3ω method. *Review of Scientific Instruments*, 61(2):802–808, 1990.

[38] S.M. Lee and D. G. Cahill. Heat transport in thin dielectric films. *Journal of Applied Physics*, 81(6):2590–2595, 1997.

[39] A. Rosencwaig, J. Opsal, W. L. Smith, and D. L. Willenborg. Detection of thermal waves through optical reflectance. *Applied Physics Letters*, 46(11):1013–1015, 1985.

[40] C. A. Paddock and G. L. Eesley. Transient thermoreflectance from thin metal films. *Journal of Applied Physics*, 60(1):285–290, 1986.

[41] K. C. Collins, A. A. Maznev, J. Cuffe, K. A. Nelson, and G. Chen. Examining thermal transport through a frequency-domain representation of time-domain thermoreflectance data. *Review of Scientific Instruments*, 85(12):124903, 2014.

[42] J. A. Malen, K. Baheti, T. Tong, Y. Zhao, J. A. Hudgings, and A. Majumdar. Optical Measurement of Thermal Conductivity Using Fiber Aligned Frequency Domain Thermoreflectance. *Journal of Heat Transfer*, 133(8):081601, 2011.

[43] J.J. Healy, J.J. de Groot, and J. Kestin. The theory of the transient hot-wire method for measuring thermal conductivity. *Physica B+C*, 82(2):392 – 408, 1976.

[44] P. Ferrando-Villalba. *Thermal characterization of Si-based nanostructures*, page 189. Universitat de Barcelona, 2016.

[45] H. S. Carslaw and J. C. Jaeger. *Conduction of Heat in Solids*. Oxford University Press, USA, 2nd edition, 1959.

[46] I. A. Stegun M. Abramowitz. *Handbook of Mathematical Functions: with Formulas, Graphs, and Mathematical Tables*. National Bureau of Standards, 1970.

[47] I. K. Moon, Y. H. Jeong, and S. I. Kwun. The 3ω technique for measuring dynamic specific heat and thermal conductivity of a liquid or solid. *Review of Scientific Instruments*, 67(1):29–35, 1996.

[48] S. Gauthier, A. Giani, and P. Combette. Gas thermal conductivity measurement using the three-omega method. *Sensors and Actuators A: Physical*, 195:50 – 55, 2013.

[49] F. Chen, J. Shulman, Y. Xue, C. W. Chu, and G. S. Nolas. Thermal conductivity measurement under hydrostatic pressure using the 3ω method. *Review of Scientific Instruments*, 75(11):4578–4584, 2004.

[50] K. I. Murata and H. Tanaka. Liquid-liquid transition without macroscopic phase separation in a water-glycerol mixture. *Nature Materials*, 11(5):436–443, 2012.

[51] A. Pettersson. Tribological characterization of environmentally adapted ester based fluids. *Tribology International*, 36(11):815 – 820, 2003. NORDTRIB symposium on Tribology 2002.

[52] http://www.dynalene.com.

[53] J.-P. E. Grolier, G. Roux-Desgranges, M. Berkane, E. Jiménez, and Emmerich Wilhelm. Heat capacities and densities of mixtures of very polar substances 2. mixtures containing N, N-dimethylformamide. *The Journal of Chemical Thermodynamics*, 25(1):41 – 50, 1993.

[54] G. García-Miaja, J. Troncoso, and L. Romaní. Excess enthalpy, density, and heat capacity for binary systems of alkylimidazolium-based ionic liquids+water. *The Journal of Chemical Thermodynamics*, 41(2):161 – 166, 2009.

[55] https://www.comsol.com/.

[56] R. Rusconi, W. C. Williams, J. Buongiorno, R. Piazza, and L. W. Hu. Numerical analysis of convective instabilities in a transient short-hot-wire setup for measurement of liquid thermal conductivity. *International Journal of Thermophysics*, 28(4):1131–1146, 2007.

[57] G. W. H. Höhne, W. F. Hemminger, and H.-J. Flammersheim. *Differential Scanning Calorimetry*. Springer, 2nd edition, 2003.

[58] S. J. Blundell and K. M. Blundell. *Concepts in Thermal Physics*. Oxford University Press, 2nd edition, 2010.

[59] D. A. Skoog, F. J. Holler, and S. R. Crouch. *Principles of Instrumental Analysis*. Cengage Learning, 7th edition, 2018.

[60] B. Outram. *Liquid Crystals*. IOP Publishing, 2018.

[61] E. Hecht. *Optics*. Addison Wesley, 4th edition, 2002.

[62] C. López-Bueno, M. Bittermann, B. Dacuña-Mariño, A. L. Llamas-Saiz, M. C. Giménez-López, S. Woutersen, and F. Rivadulla. Low temperature glass/crystal transition in ionic liquids determined by H-bond vs. coulombic strength. *Phys. Chem. Chem. Phys.*, 22:20524–20530, 2020.

[63] J. F. Kincaid and H. Eyring. Free volumes and free angle ratios of molecules in liquids. *The Journal of Chemical Physics*, 6(10):620–629, 1938.

[64] K. Nakamoto. *Infrared and Raman Spectra of Inorganic and Coordination Compounds*. John Wiley & Sons, 6th edition, 2009.

[65] J. A. Zeitler, P. F. Taday, D. A. Newnham, M. Pepper, K. C. Gordon, and T. Rades. Terahertz pulsed spectroscopy and imaging in the pharmaceutical setting - a review. *Journal of Pharmacy and Pharmacology*, 59(2):209–223, 2007.

[66] P. Atkins and J. de Paula. *Elements of Physical Chemistry*. Oxford University Press, 5th edition, 2009.

[67] J. B. Brubach, A. Mermet, A. Filabozzi, A. Gerschel, and P. Roy. Signatures of the hydrogen bonding in the infrared bands of water. *Journal of Chemical Physics*, 122(18):3249, 2005.

[68] A. B. McCoy. The role of electrical anharmonicity in the association band in the water spectrum. *Journal of Physical Chemistry B*, 118(28):8286–8294, 2014.

[69] P. K. Verma, A. Kundu, M. S. Puretz, C. Dhoonmoon, O. S Chegwidden, C. H. Londergan, and M. Cho. The Bend+Libration Combination Band Is an Intrinsic, Collective, and Strongly Solute-Dependent Reporter on the Hydrogen Bonding Network of Liquid Water. *Journal of Physical Chemistry B*, 122(9):2587–2599, 2018.

[70] S. A. Khan, S. B. Khan, L. U. Khan, A. Farooq, K. Akhtar, and A. M. Asiri. *Fourier Transform Infrared Spectroscopy: Fundamentals and Application in Functional Groups and Nanomaterials Characterization*, pages 317–344. Springer International Publishing, Cham, 2018.

[71] H. S. Carslaw. *Introduction to the theory of Fourier's series and integrals*. Dover Publications, Inc., 3rd edition, 1930.

[72] C. López-Bueno, M. Suárez-Rodríguez, A. Amigo, and F. Rivadulla. Hydrophobic solvation increases thermal conductivity of water. *Phys. Chem. Chem. Phys.*, 22:21094–21098, 2020.

[73] C. López-Bueno, C. Herreros-Lucas, M. Suárez-Rodríguez, M. Bittermann, A. Amigo, S. Woutersen, M. C. Giménez-López, and F. Rivadulla. A new type of supramolecular fluid based on H_2O-alkylammonium/phosphonium solutions. *Angewandte Chemie International Edition*, 60(14):7540–7546, 2021.

[74] T. J. Fortin, A. Laesecke, M. Freund, and S. Outcalt. Advanced calibration, adjustment, and operation of a density and sound speed analyzer. *Journal of Chemical Thermodynamics*, 57:276–285, 2013.

[75] R. F. Chang and M. R. Moldover. High-temperature high-pressure oscillating tube densimeter. *Review of Scientific Instruments*, 67(1):251–256, 1996.

[76] Anton Paar. How to measure viscosity. https://wiki.anton-paar.com/en/how-to-measure-viscosity/#c16696.

[77] Anton Paar. *Manual of SVM 3000 Stabinger Viscometer*. 2015.

[78] L. D. Landau and E. M. Lifshitz. *Fluid Mechanics*. Pergamon Press, 2nd edition, 1987.

[79] P. Gallo, K. Amann-Winkel, C. A. Angell, M. A. Anisimov, F. Caupin, C. Chakravarty, E. Lascaris, T. Loerting, A. Z. Panagiotopoulos, J. Russo, J. A. Sellberg, H. E. Stanley, H. Tanaka, C. Vega, L. Xu, and L. G. M. Pettersson. Water: A Tale of Two Liquids. *Chemical Reviews*, 116(13):7463–7500, 2016.

[80] W. Kunz, J. Henle, and B. W. Ninham. 'Zur Lehre von der Wirkung der Salze' (about the science of the effect of salts): Franz Hofmeister's historical papers. *Current Opinion in Colloid and Interface Science*, 9(1-2):19–37, 2004.

[81] F. Hofmeister. Zur Lehre von der Wirkung der Salze - Zweite Mittheilung. *Archiv für Experimentelle Pathologie und Pharmakologie*, 24(4-5):247–260, 1888.

[82] Y. Zhang and P. S. Cremer. Interactions between macromolecules and ions: the Hofmeister series. *Current Opinion in Chemical Biology*, 10(6):658–663, 2006.

[83] Q. Sun. The physical origin of hydrophobic effects. *Chemical Physics Letters*, 672:21–25, 2017.

[84] A. Asenbaum, C. Pruner, E. Wilhelm, M. Mijakovic, L. Zoranic, F. Sokolic, B. Kezic, and A. Perera. Structural changes in ethanol-water mixtures: Ultrasonics, Brillouin scattering and molecular dynamics studies. *Vibrational Spectroscopy*, 60:102–106, 2012.

[85] M. L. Tan, B. T. Miller, J. Te, J. R. Cendagorta, B. R. Brooks, and T. Ichiye. Hydrophobic hydration and the anomalous partial

molar volumes in ethanol-water mixtures. *Journal of Chemical Physics*, 142(6):1–6, 2015.

[86] M. Tros, L. Zheng, J. Hunger, M. Bonn, D. Bonn, G. J. Smits, and S. Woutersen. Picosecond orientational dynamics of water in living cells. *Nature Communications*, 8(1):904, 2017.

[87] P. Ball. Water as an active constituent in cell biology. *Chemical Reviews*, 108(1):74–108, 2008.

[88] H. S. Frank and M. W. Evans. Free Volume and Entropy in Condensed Systems III. Entropy in Binary Liquid Mixtures; Partial Molal Entropy in Dilute Solutions; Structure and Thermodynamics in Aqueous Electrolytes. *The Journal of Chemical Physics*, 13(11):507–532, 1945.

[89] S. Dixit, J. Crain, W. C.K. Poon, J. L. Finney, and A. K. Soper. Molecular segregation observed in a concentrated alcohol-water solution. *Nature*, 416(6883):829–832, 2002.

[90] N. Nishi, S. Takahashi, M. Matsumoto, A. Tanaka, K. Muraya, T. Takamuku, and T. Yamaguchi. Hydrogen-Bonded Cluster Formation and Hydrophobic Solute Association in Aqueous Solutions of Ethanol. *The Journal of Physical Chemistry*, 99(1):462–468, 1995.

[91] J. Fidler and P. M. Rodger. Solvation structure around aqueous alcohols. *Journal of Physical Chemistry B*, 103(36):7695–7703, 1999.

[92] H. J. Bakker and J. L. Skinner. Vibrational spectroscopy as a probe of structure and dynamics in liquid water. *Chemical Reviews*, 110(3):1498–1517, 2010.

[93] D. Laage, G. Stirnemann, F. Sterpone, R. Rey, and J. T. Hynes. Reorientation and Allied Dynamics in Water and Aqueous Solutions. *Annual Review of Physical Chemistry*, 62(1):395–416, 2011.

[94] K. J. Tielrooij, N. Garcia-Araez, M. Bonn, and H. J. Bakker. Cooperativity in ion hydration. *Science*, 328(5981):1006–1009, 2010.

[95] X. B. Wang, X. Yang, J. B. Nicholas, and L. S. Wang. Bulk-like features in the photoemission spectra of hydrated doubly charged anion clusters. *Science*, 294(5545):1322–1325, 2001.

[96] A. Wakisaka and K. Matsuura. Microheterogeneity of ethanol-water binary mixtures observed at the cluster level. *Journal of Molecular Liquids*, 129(1-2):25–32, 2006.

[97] N. Nishi, K. Koga, C. Ohshima, K. Yamamoto, U. Nagashima, and K. Nagami. Molecular Association in Ethanol-Water Mixtures Studied by Mass Spectrometric Analysis of Clusters Generated through Adiabatic Expansion of Liquid Jets. *Journal of the American Chemical Society*, 110(16):5246–5255, 1988.

[98] R. Li, C. D'Agostino, J. McGregor, M. D. Mantle, J. A. Zeitler, and L. F. Gladden. Mesoscopic structuring and dynamics of alcohol/water solutions probed by terahertz time-domain spectroscopy and pulsed field gradient nuclear magnetic resonance. *Journal of Physical Chemistry B*, 118(34):10156–10166, 2014.

[99] U. Heugen, G. Schwaab, E. Bründermann, M. Heyden, X. Yu, D. M. Leitner, and M. Havenith. Solute-induced retardation of water dynamics probed directly by terahertz spectroscopy. *Proceedings of the National Academy of Sciences of the United States of America*, 103(33):12301–12306, 2006.

[100] S. Funkner, G. Niehues, D. A. Schmidt, M. Heyden, G. Schwaab, K. M. Callahan, D. J. Tobias, and M. Havenith. Watching the low-frequency motions in aqueous salt solutions: The terahertz vibrational signatures of hydrated ions. *Journal of the American Chemical Society*, 134(2):1030–1035, 2012.

[101] G. Schwaab, F. Sebastiani, and M. Havenith. Ion Hydration and Ion Pairing as Probed by THz Spectroscopy. *Angewandte Chemie - International Edition*, 58(10):3000–3013, 2019.

[102] A. W. Omta, M. F. Kropman, S. Woutersen, and H. J. Bakker. Influence of ions on the hydrogen-bond structure in liquid water. *Journal of Chemical Physics*, 119(23):12457–12461, 2003.

[103] A. W. Omta, M. F. Kropman, S. Woutersen, and H. J. Bakker. Negligible effect of ions on the hydrogen-bond structure in liquid water. *Science*, 301(5631):347–349, 2003.

[104] J. Grdadolnik, F. Merzel, and F. Avbelj. Origin of hydrophobicity and enhanced water hydrogen bond strength near purely hydrophobic solutes. *Proceedings of the National Academy of Sciences*, 114(2):322–327, 2017.

[105] M. L. Tan, J. R. Cendagorta, and T. Ichiye. Effects of microcomplexity on hydrophobic hydration in amphiphiles. *Journal of the American Chemical Society*, 135(13):4918–4921, 2013.

[106] R. Ghosh and B. Bagchi. Temperature Dependence of Static and Dynamic Heterogeneities in a Water-Ethanol Binary Mixture and a Study of Enhanced, Short-Lived Fluctuations at Low Concentrations. *Journal of Physical Chemistry B*, 120(49):12568–12583, 2016.

[107] B. Auer, R. Kumar, J. R. Schmidt, and J. L. Skinner. Hydrogen bonding and Raman, IR, and 2D-IR spectroscopy of dilute HOD in liquid D_2O. *Proceedings of the National Academy of Sciences of the United States of America*, 104(36):14215–14220, 2007.

[108] O. Andersson and A. Inaba. Thermal conductivity of crystalline and amorphous ices and its implications on amorphization and glassy water. *Physical Chemistry Chemical Physics*, 7(7):1441–1449, 2005.

[109] O. Andersson. Thermal conductivity of normal and deuterated water, crystalline ice, and amorphous ices. *Journal of Chemical Physics*, 149(12):124506, 2018.

[110] A. Lervik, F. Bresme, S. Kjelstrup, D. Bedeaux, and J. M. Rubi. Heat transfer in protein-water interfaces. *Physical Chemistry Chemical Physics*, 12(7):1610–1617, 2010.

[111] P. Wang and A. Anderko. Modeling Thermal Conductivity of Concentrated and Mixed-Solvent Electrolyte Systems. *Industrial and Engineering Chemistry Research*, 47:5698–5709, 2008.

[112] R. Yano, Y. Fukuda, and T. Hashi. Thermal conductivity measurement of water-ethanol solutions by the laser-induced transient grating method. *Chemical Physics*, 124(2):315–319, 1988.

[113] L. A. Akhmedova-Azizova and I. M. Abdulagatov. Thermal conductivity of aqueous K_2CO_3 solutions at high temperatures. *Journal of Solution Chemistry*, 38(8):1015–1028, 2009.

[114] I. M. Abdulagatov and U. B. Magomedov. Thermal conductivity of aqueous KI and KBr Solutions at High Temperatures and High Pressures. *Journal of Solution Chemistry*, 30(3):223–235, 2001.

[115] Z. Losenicky. Thermal conductivity of binary liquid solutions. *Journal of Physical Chemistry*, 72(12):4308–4310, 1968.

[116] S. Burikov, S. Dolenko, T. Dolenko, S. Patsaeva, and V. Yuzhakov. Decomposition of water Raman stretching band with a combination of optimization methods. *Molecular Physics*, 108(6):739–747, 2010.

[117] I. Juurinen, K. Nakahara, N. Ando, T. Nishiumi, H. Seta, N. Yoshida, T. Morinaga, M. Itou, T. Ninomiya, Y. Sakurai, E. Salonen, K. Nordlund, K. Hämäläinen, and M. Hakala. Measurement of two solvation regimes in water-ethanol mixtures using x-ray Compton scattering. *Physical Review Letters*, 107(19):197401, 2011.

[118] R. M. DiGuilio and A. S. Teja. Thermal Conductivity of Aqueous salt Solutions at High Temperatures and High Concentrations. *Industrial and Engineering Chemistry Research*, 31:1081–1085, 1992.

[119] D. Bohne, S. Fischer, and E. Obermeier. Thermal Conductivity, Density, Viscosity, and Prandtl- Numbers of Ethylene Glycol-Water Mixtures. *Berichte der Bunsengesellschaft/Physical Chemistry Chemical Physics*, 88:739–742, 1984.

[120] X. Cui, H. Zhu, C. H. He, and K. J. Wu. Measurement of the Thermal Conductivity of 1-Butyl-3-methylimidazolium l - Tryptophan + Water + Ethanol Mixtures at T = (283.15 to 333.15) K. *Journal of Chemical and Engineering Data*, 64(4):1586–1593, 2019.

[121] J. G. Davis, K. P. Gierszal, P. Wang, and D. Ben-Amotz. Water structural transformation at molecular hydrophobic interfaces. *Nature*, 491(7425):582–585, 2012.

[122] Y. L. A. Rezus and H. J. Bakker. Observation of immobilized water molecules around hydrophobic groups. *Physical Review Letters*, 99(14), 2007.

[123] R. Halder and B. Jana. Unravelling the Composition-Dependent Anomalies of Pair Hydrophobicity in Water-Ethanol Binary Mixtures. *Journal of Physical Chemistry B*, 122(26):6801–6809, 2018.

[124] L. B. Skinner, C. J. Benmore, J. C. Neuefeind, and J. B. Parise. The structure of water around the compressibility minimum. *Journal of Chemical Physics*, 141(21):214507, 2014.

[125] C. Huang, K. T. Wikfeldt, T. Tokushima, D. Nordlund, Y. Harada, U. Bergmann, M. Niebuhr, T. M. Weiss, Y. Horikawa, M. Leetmaa, M. P. Ljungberg, O. Takahashi, A. Lenz, L. Ojamäe, A. P.

Lyubartsev, S. Shin, L. G.M. Pettersson, and A. Nilsson. The inhomogeneous structure of water at ambient conditions. *Proceedings of the National Academy of Sciences of the United States of America*, 106(36):15214–15218, 2009.

[126] D. Schlesinger, K. T. Wikfeldt, L. B. Skinner, C. J. Benmore, A. Nilsson, and L. G. M. Pettersson. The temperature dependence of intermediate range oxygen-oxygen correlations in liquid water. *Journal of Chemical Physics*, 145(8):084503, 2016.

[127] G. Onori. Adiabatic compressibility and structure of aqueous solutions of ethyl alcohol. *The Journal of Chemical Physics*, 89(7):4325–4332, 1988.

[128] H. D. Pandey and D. M. Leitner. Small saccharides as a blanket around proteins: A computational study. *The Journal of Physical Chemistry B*, 122(29):7277–7285, 2018.

[129] D. Corradini, Z. Su, H. E. Stanley, and P. Gallo. A molecular dynamics study of the equation of state and the structure of supercooled aqueous solutions of methanol. *Journal of Chemical Physics*, 137(18):184503, 2012.

[130] P. H. Poole, F. Sciortino, U. Essmann, and H. E. Stanley. Phase behaviour of metastable water. *Nature*, 360:324–328, 1992.

[131] O. Mishima, L. D. Calvert, and E. Whalley. An apparently first-order transition between two amorphous phases of ice induced by pressure. *Nature*, 314(6006):76–78, 1985.

[132] O. Mishima and H. E. Stanley. Decompression-induced melting of ice IV and the liquid-liquid transition in water. *Nature*, 392:164–168, 1998.

[133] D. G. Archer and R. W. Carter. Thermodynamic properties of the NaCl + H_2O system. 4. Heat capacities of H_2O and NaCl(aq) in cold-stable and supercooled states. *Journal of Physical Chemistry B*, 104(35):8563–8584, 2000.

[134] R. W. Carter and D. G. Archer. Heat capacity of $NaNO_3$(aq) in stable and supercooled states. Ion association in the supercooled solution. *Physical Chemistry Chemical Physics*, 2(22):5138–5145, 2000.

[135] K. Miyata, H. Kanno, T. Niino, and K. Tomizawa. Cationic and anionic effects on the homogeneous nucleation of ice in aqueous alkali halide solutions. *Chemical Physics Letters*, 354(1-2):51–55, 2002.

[136] K. Miyata and H. Kanno. Supercooling behavior of aqueous solutions of alcohols and saccharides. *Journal of Molecular Liquids*, 119(1-3):189–193, 2005.

[137] M. Oguni and C. A. Angell. Hydrophobic and hydrophilic solute effects on the homogeneous nucleation temperature of ice from aqueous solutions. *Journal of Physical Chemistry*, 87(11):1848–1851, 1983.

[138] K. Oka, T. Shibue, N. Sugimura, Y. Watabe, M. Tanaka, B. Winther-Jensen, and H. Nishide. Two States of Water Converge to One State below 215 K. *The Journal of Physical Chemistry Letters*, 12:5802–5806, 2021.

[139] J. R. Bruijn, T. H. Van Der Loop, and S. Woutersen. Changing Hydrogen-Bond Structure during an Aqueous Liquid-Liquid Transition Investigated with Time-Resolved and Two-Dimensional Vibrational Spectroscopy. *Journal of Physical Chemistry Letters*, 7(5):795–799, 2016.

[140] S. Woutersen, B. Ensing, M. Hilbers, Z. Zhao, and C. A. Angell. A liquid-liquid transition in supercooled aqueous solution related to the HDA-LDA transition. *Science*, 359(6380):1127–1131, 2018.

[141] P. Wernet, D. Nordlund, U. Bergmann, M. Cavalleri, N. Odelius, H. Ogasawara, L. Å Näslund, T. K. Hirsch, L. Ojamäe, P. Glatzel,

L. G.M. Pettersson, and A. Nilsson. The Structure of the First Coordination Shell in Liquid Water. *Science*, 304(5673):995–999, 2004.

[142] A. Nilsson, D. Nordlund, I. Waluyo, N. Huang, H. Ogasawara, S. Kaya, U. Bergmann, L. Å Näslund, H. Öström, Ph. Wernet, K. J. Andersson, T. Schiros, and L. G. M. Pettersson. X-ray absorption spectroscopy and X-ray Raman scattering of water and ice; an experimental view. *Journal of Electron Spectroscopy and Related Phenomena*, 177(2-3):99–129, 2010.

[143] T. Tokushima, Y. Harada, O. Takahashi, Y. Senba, H. Ohashi, L. G. M. Pettersson, A. Nilsson, and S. Shin. High resolution X-ray emission spectroscopy of liquid water: The observation of two structural motifs. *Chemical Physics Letters*, 460(4-6):387–400, 2008.

[144] F. Sciortino, A. Geiger, and H. E. Stanley. Effect of defects on molecular mobility in liquid water. *Nature*, 354:218–221, 1991.

[145] S. Saito, B. Bagchi, and I. Ohmine. Crucial role of fragmented and isolated defects in persistent relaxation of deeply supercooled water. *Journal of Chemical Physics*, 149(12):124504, 2018.

[146] K. Oka, T. Shibue, N. Sugimura, Y. Watabe, B. Winther-Jensen, and H. Nishide. Long-lived water clusters in hydrophobic solvents investigated by standard NMR techniques. *Scientific Reports*, 9(1), 2019.

[147] K. Oka, T. Shibue, N. Sugimura, Y. Watabe, B. Winther-Jensen, and H. Nishide. Supercooled Low-Entropy Water Clusters. *Journal of Physical Chemistry Letters*, 11(9):3667–3671, 2020.

[148] O. Andersson and U. Häussermann. A Second Glass Transition in Pressure Collapsed Type II Clathrate Hydrates. *Journal of Physical Chemistry B*, 122(15):4376–4384, 2018.

[149] A. I. Krivchikov and O. Andersson. Thermal Conductivity of Triphenyl Phosphite's Liquid, Glassy, and Glacial States. *Journal of Physical Chemistry B*, 120(10):2845–2853, 2016.

[150] W. N. Dos Santos, J. A. De Sousa, and R. Gregorio. Thermal conductivity behaviour of polymers around glass transition and crystalline melting temperatures. *Polymer Testing*, 32(5):987–994, 2013.

[151] O. Andersson and G. P. Johari. Thermal conductivity of Glycerol's liquid, glass, and crystal states, glass-liquid-glass transition, and crystallization at high pressures. *Journal of Chemical Physics*, 144(6):064504, 2016.

[152] E. D. Sloan. Fundamental principles and applications of natural gas hydrates. *Nature*, 426:353–359, 2003.

[153] D. L. Fowler, W. V. Loebenstein, D. B. Pall, and C. A. Kraus. Some Unusual Hydrates of Quaternary Ammonium Salts. *Journal of the American Chemical Society*, 62(5):1140–1142, 1940.

[154] G. A. Jeffrey and R. K. McMullan. The Clathrate Hydrates. In F. Albert Cotton, editor, *Progress in Inorganic Chemistry*, volume 8 of *Progress in Inorganic Chemistry*, pages 43–104. John Wiley & Sons, Inc., Hoboken, NJ, USA, 1967.

[155] H. P. Veluswamy, R. Kumar, and P. Linga. Hydrogen storage in clathrate hydrates: Current state of the art and future directions. *Applied Energy*, 122:112–132, 2014.

[156] L. J. Florusse, C. J. Peters, J. Schoonman, K. C. Hester, C. A. Koh, S. F. Dec, K. N. Marsh, and E. D. Sloan. Stable low-pressure hydrogen clusters stored in a binary clathrate hydrate. *Science*, 306(5695):469–471, 2004.

[157] X. S. Li, Z. M. Xia, Z. Y. Chen, K. F. Yan, G. Li, and H. J. Wu. Equilibrium hydrate formation conditions for the mixtures

of $CO_2 + H_2$+ tetrabutyl ammonium bromide. *Journal of Chemical and Engineering Data*, 55(6):2180–2184, 2010.

[158] W. Shimada, M. Shiro, H. Kondo, S. Takeya, H. Oyama, T. Ebinuma, and H. Marita. Tetra-n-butylammonium bromide-water (1/38). *Acta Crystallographica Section C: Crystal Structure Communications*, 61(2):1–3, 2005.

[159] P. S. R. Prasad and B. Sai Kiran. Clathrate Hydrates of Greenhouse Gases in the Presence of Natural Amino Acids: Storage, Transportation and Separation Applications. *Scientific Reports*, 8(1):8560, 2018.

[160] Y. Kamata, H. Oyama, W. Shimada, T. Ebinuma, S. Takeya, T. Uchida, J. Nagao, and H. Narita. Gas Separation Method Using Tetra-n-butyl Ammonium Bromide Semi-Clathrate Hydrate. *Japanese Journal of Applied Physics*, 43(1):362–365, 2004.

[161] Y. Kamata, Y. Yamakoshi, T. Ebinuma, H. Oyama, W. Shimada, and H. Narita. Hydrogen sulfide separation using tetra-n-butyl ammonium bromide semi-clathrate (TBAB) hydrate. *Energy and Fuels*, 19(4):1717–1722, 2005.

[162] P. S. R. Prasad, T. Sugahara, A. K. Sum, E. D. Sloan, and C. A. Koh. Hydrogen storage in double clathrates with tert-butylamine. *Journal of Physical Chemistry A*, 113(24):6540–6543, 2009.

[163] T. A. Strobel, C. A. Koh, and E. D. Sloan. Hydrogen storage properties of clathrate hydrate materials. *Fluid Phase Equilibria*, 261(1-2):382–389, 2007.

[164] I. Chatti, A. Delahaye, L. Fournaison, and J. P. Petitet. Benefits and drawbacks of clathrate hydrates: A review of their areas of interest. *Energy Conversion and Management*, 46(9-10):1333–1343, 2005.

[165] E. A. G. Schuur, A. D. McGuire, C. Schädel, G. Grosse, J. W. Harden, D. J. Hayes, G. Hugelius, C. D. Koven, P. Kuhry,

D. M. Lawrence, S. M. Natali, D. Olefeldt, V. E. Romanovsky, K. Schaefer, M. R. Turetsky, C. C. Treat, and J. E. Vonk. Climate change and the permafrost carbon feedback. *Nature*, 520(7546):171–179, 2015.

[166] T. V. Rodionova, V. Y. Komarov, G. V. Villevald, T. D. Karpova, N. V. Kuratieva, and A. Y. Manakov. Calorimetric and structural studies of tetrabutylammonium bromide ionic clathrate hydrates. *Journal of Physical Chemistry B*, 117(36):10677–10685, 2013.

[167] M. Arjmandi, A. Chapoy, and B. Tohidi. Equilibrium data of hydrogen, methane, nitrogen, carbon dioxide, and natural gas in semi-Clathrate hydrates of tetrabutyl ammonium bromide. *Journal of Chemical and Engineering Data*, 52(6):2153–2158, 2007.

[168] J. Deschamps and D. Dalmazzone. Dissociation enthalpies and phase equilibrium for TBAB semi-clathrate hydrates of N_2, CO_2, $N_2 + CO_2$ and $CH_4 + CO_2$. *Journal of Thermal Analysis and Calorimetry*, 98(1):113–118, 2009.

[169] D. Bhowmik, N. Malikova, G. Mériguet, O. Bernard, J. Teixeira, and P. Turq. Aqueous solutions of tetraalkylammonium halides: Ion hydration, dynamics and ion-ion interactions in light of steric effects. *Physical Chemistry Chemical Physics*, 16(26):13447–13457, 2014.

[170] F. H. Stillinger. Water Revisited. *Science*, 209(4455):451–457, 1980.

[171] A. V. Kustov. Thermodynamic properties of aqueous solutions of tetraalkylammonium salts: Dependence of the hydrophobic hydration effect on the cation size. *Russian Journal of Inorganic Chemistry*, 54(2):323–328, 2009.

[172] S. Bradl and E. W. Lang. Hydration water dynamics in undercooled aqueous solutions of hydrophobic ions. *Journal of Physical Chemistry*, 97(40):10463–10471, 1993.

[173] D. González-Salgado, K. Zemánková, E. G. Noya, and E. Lomba. Temperature of maximum density and excess thermodynamics of aqueous mixtures of methanol. *Journal of Chemical Physics*, 144(18):184505, 2016.

[174] H. N. Sarode, G. E. Lindberg, Y. Yang, L. E. Felberg, G. A. Voth, and A. M. Herring. Insights into the transport of aqueous quaternary ammonium cations: A combined experimental and computational study. *Journal of Physical Chemistry B*, 118(5):1363–1372, 2014.

[175] J. T. Slusher and P. T. Cummings. Molecular Simulation Study of Tetraalkylammonium Halides. 1. Solvation Structure and Hydrogen Bonding in Aqueous Solutions. *Journal of Physical Chemistry B*, 101:3818–3826, 1997.

[176] J. Z. Turner, A. K. Soper, and J. L. Finney. Ionic versus apolar behavior of the tetramethylammonium ion in water. *The Journal of Chemical Physics*, 102(13):5438–5443, 1995.

[177] L. García-Tarrés and E. Guàrdia. Hydration and dynamics of a tetramethylammonium ion in water: A computer simulation study. *Journal of Physical Chemistry B*, 102(38):7448–7454, 1998.

[178] D. Bhowmik, N. Malikova, J. Teixeira, G. Mériguet, O. Bernard, P. Turq, and W. Häussler. Study of tetrabutylammonium bromide in aqueous solution by neutron scattering. *European Physical Journal: Special Topics*, 213(1):303–312, 2012.

[179] E. J. Nilsson, V. Alfredsson, D. T. Bowron, and K. J. Edler. A neutron scattering and modelling study of aqueous solutions of tetramethylammonium and tetrapropylammonium bromide. *Physical Chemistry Chemical Physics*, 18(16):11193–11201, 2016.

[180] A. Novikow, M. Rodnikova, J. Barthel, and O. Sobolev. Quasielastic neutron scattering of aqueous tetrabutylammonium

chloride solutions. *Journal of Molecular Liquids*, 79(3):203–212, 1999.

[181] Y. Marcus. Tetraalkylammonium ions in aqueous and non-aqueous solutions. *Journal of Solution Chemistry*, 37(8):1071–1098, 2008.

[182] D. Bhowmik. Behavior of aqueous Tetrabutylammonium bromide - a combined approach of microscopic simulation and neutron scattering. *arXiv*, 1609.02929v1, 2016.

[183] R. Mcmullan and G. A. Jeffrey. Hydrates of the tetra n-butyl and tetra i-amyl quaternary ammonium salts. *The Journal of Chemical Physics*, 31(5):1231–1234, 1959.

[184] E. Amado and L. H. Blanco. Isopiestic determination of the osmotic and Activity coefficients of aqueous solutions of symmetrical and unsymmetrical quaternary ammonium bromides at T = (283.15 and 288.15) K. *Journal of Chemical and Engineering Data*, 54(9):2696–2700, 2009.

[185] G. Beurskens, G. A. Jeffrey, and R. K. McMullan. Polyhedral clathrate hydrates. VI. Lattice type and ion distribution in some new peralkyl ammonium, phosphonium, and sulfonium salt hydrates. *The Journal of Chemical Physics*, 39(12):3311–3315, 1963.

[186] M. J. V. Lourenço, F. J. V. Santos, M. L. V. Ramires, and C. A. N. de Castro. Isobaric specific heat capacity of water and aqueous cesium chloride solutions for temperatures between 298 K and 370 K at p = 0.1 MPa. *Journal of Chemical Thermodynamics*, 38(8):970–974, 2006.

[187] K. Oster, P. Goodrich, J. Jacquemin, C. Hardacre, A. P. C. Ribeiro, and A. Elsinawi. A new insight into pure and water-saturated quaternary phosphonium-based carboxylate ionic liquids: Density, heat capacity, ionic conductivity, thermogravi-

metric analysis, thermal conductivity and viscosity. *Journal of Chemical Thermodynamics*, 121:97–111, 2018.

[188] F. J. Millero, G. Perron, and J.E. Desnoyers. Heat Capacity of Seawater Solutions from 5^o to 35^o and 0.5 to 22% Chlorinity. *Journal of Geophysical Research*, 78(21):4–6, 1973.

[189] H. Piekarski and M. Tkaczyk. Heat capacity and phase behavior of C6E4+water solutions by DSC. *Journal of Thermal Analysis and Calorimetry*, 83(3):541–547, 2006.

[190] S. A Rice and M. G. Sceats. A random network for water. *J. Phys. Chem.*, 85:1108–1119, 1981.

[191] T. A. Ford and M. Falk. Hydrogen bonding in water and ice. *Canadian Journal of Chemistry*, 46(22):3579–3586, 1968.

[192] F. Li and J. L. Skinner. Infrared and Raman line shapes for ice Ih. I. Dilute HOD in H_2O and D_2O. *Journal of Chemical Physics*, 132(20):14502, 2010.

[193] T. G. Stoebe, T. O. Ogurtani, and R. A. Huggins. Motional Narrowing of Nuclear Magnetic-Resonance Lines in Manganese-Doped Lithium Fluoride. *Physical Review*, 134(4A), 1964.

[194] T. Kobori, S. Muromachi, T. Yamasaki, S. Takeya, Y. Yamamoto, S. Alavi, and R. Ohmura. Phase Behavior and Structural Characterization of Ionic Clathrate Hydrate Formed with Tetra-n-butylphosphonium Hydroxide: Discovery of Primitive Crystal Structure. *Crystal Growth and Design*, 15(8):3862–3867, 2015.

[195] M. Amid, S. P. G. Zaferani, and A. A. Amooey. A compare review about equilibrium conditions of semi-clathrate hydrate: experimental measurements visions and thermodynamic modeling aspects. *Journal of Inclusion Phenomena and Macrocyclic Chemistry*, 2021.

[196] S. Forster, G. Buckton, and A. E. Beezer. The importance of chain length on the wettability and solubility of organic homologs. *International Journal of Pharmaceutics*, 72(1):29–34, 1991.

[197] D. W. Ball, J. W. Hill, and R. J. Scott. *The Basics of General, Organic, and Biological Chemistry*. LibreTexts, 2020.

[198] S. M. Vilas-Boas, D. O. Abranches, E. A. Crespo, O. Ferreira, J. A. P. Coutinho, and S. P. Pinho. Experimental solubility and density studies on aqueous solutions of quaternary ammonium halides, and thermodynamic modelling for melting enthalpy estimations. *Journal of Molecular Liquids*, 300, 2020.

[199] Z. Li, D. L. Zhong, W. Y. Zheng, J. Yan, Y. Y. Lu, and D. T. Yi. Morphology and kinetic investigation of TBAB/TBPB semiclathrate hydrates formed with a $CO_2 + CH_4$ gas mixture. *Journal of Crystal Growth*, 511:79–88, 2019.

[200] J. Deschamps and D. Dalmazzone. Hydrogen storage in semiclathrate hydrates of tetrabutyl ammonium chloride and tetrabutyl phosphonium bromide. *Journal of Chemical and Engineering Data*, 55(9):3395–3399, 2010.

[201] H. Oyama, W. Shimada, T. Ebinuma, Y. Kamata, S. Takeya, T. Uchida, J. Nagao, and H. Narita. Phase diagram, latent heat, and specific heat of TBAB semiclathrate hydrate crystals. *Fluid Phase Equilibria*, 234(1-2):131–135, 2005.

[202] M. Hao, J. Li, S. Park, S. Moura, and C. Dames. Efficient thermal management of Li-ion batteries with a passive interfacial thermal regulator based on a shape memory alloy. *Nature Energy*, 3(10):899–906, 2018.

[203] L. Guo, X. Zhang, Y. Huang, R. Hu, and C. Liu. Thermal characterization of a new differential thermal expansion heat switch for space optical remote sensor. *Applied Thermal Engineering*, 113:1242–1249, 2017.

[204] J. A. Tomko, A. Pena-Francesch, H. Jung, M. Tyagi, B. D. Allen, M. C. Demirel, and P. E. Hopkins. Tunable thermal transport and reversible thermal conductivity switching in topologically networked bio-inspired materials. *Nature Nanotechnology*, 13(10):959–964, 2018.

[205] G. Cha, C. J. Kim, and Y. S. Ju. Thermal conductance switching based on the actuation of liquid droplets through the electrowetting on dielectric (EWOD) phenomenon. *Applied Thermal Engineering*, 98:189–195, 2016.

[206] E. Langenberg, D. Saha, M. E. Holtz, J. J. Wang, D. Bugallo, E. Ferreiro-Vila, H. Paik, I. Hanke, S. Ganschow, D. A. Muller, L. Q. Chen, G. Catalan, N. Domingo, J. Malen, D. G. Schlom, and F. Rivadulla. Ferroelectric Domain Walls in PbTiO3 Are Effective Regulators of Heat Flow at Room Temperature. *Nano Letters*, 19(11):7901–7907, 2019.

[207] G. Cha, Y. S. Ju, L. A. Ahuré, and N. M. Wereley. Experimental characterization of thermal conductance switching in magnetorheological fluids. *Journal of Applied Physics*, 107(9):9–505, 2010.

[208] J. Cho, M. D. Losego, H. G. Zhang, H. Kim, J. Zuo, I. Petrov, D. G. Cahill, and P. V. Braun. Electrochemically tunable thermal conductivity of lithium cobalt oxide. *Nature Communications*, 5, 2014.

[209] T. Yang, B. Kwon, P. B. Weisensee, J. G. Kang, X. Li, P. Braun, N. Miljkovic, and W. P. King. Millimeter-scale liquid metal droplet thermal switch. *Applied Physics Letters*, 112(6):63505, 2018.

[210] J. F. Ihlefeld, B. M. Foley, D. A. Scrymgeour, J. R. Michael, B. B. McKenzie, D. L. Medlin, M. Wallace, S. Trolier-Mckinstry, and P. E. Hopkins. Room-temperature voltage tunable phonon thermal conductivity via reconfigurable interfaces in ferroelectric thin films. *Nano Letters*, 15(3):1791–1795, 2015.

[211] Q. Zheng, G. Zhu, Z. Diao, D. Banerjee, and D. G. Cahill. High Contrast Thermal Conductivity Change in Ni–Mn–In Heusler Alloys near Room Temperature. *Advanced Engineering Materials*, 21(5), 2019.

[212] S. N. Schiffres, S. Harish, S. Maruyama, J. Shiomi, and J. A Malen. Tunable electrical and thermal transport in icelated multilayer graphene nanocomposites through freezing rate control. *ACS Nano*, 7(12):11183–11189, 2013.

[213] L. E. Ehrlich, J. S. G. Feig, S. N. Schiffres, J. A. Malen, and Y. Rabin. Large thermal conductivity differences between the crystalline and vitrified states of DMSO with applications to cryopreservation. *PLoS ONE*, 10(5), 2015.

[214] J. Shin, J. Sung, M. Kang, X. Xie, B. Lee, K. M. Lee, T. J. White, C. Leal, N. R. Sottos, P. V. Braun, and D. G. Cahill. Light-triggered thermal conductivity switching in azobenzene polymers. *Proceedings of the National Academy of Sciences of the United States of America*, 116(13):5973–5978, 2019.

[215] C. Li, Y. Ma, and Z. Tian. Thermal Switching of Thermoresponsive Polymer Aqueous Solutions. *ACS Macro Letters*, 7(1):53–58, 2018.

[216] M. Ryu, H. Takezoe, O. Haba, K. Yonetake, and J. Morikawa. Photo-controllable thermal diffusivity and thermal conductivity driven by the orientation change of nematic liquid crystal with azo-dendrimers. *Applied Physics Letters*, 107(22), 2015.

[217] R. Zheng, J. Gao, J. Wang, and G. Chen. Reversible temperature regulation of electrical and thermal conductivity using liquid-solid phase transitions. *Nature Communications*, 2(1), 2011.

[218] J. Vila, B. Fernández-Castro, E. Rilo, J. Carrete, M. Domínguez-Pérez, J. R. Rodríguez, M. García, L. M. Varela, and O. Cabeza. Liquid-solid-liquid phase transition hysteresis loops in the ionic

conductivity of ten imidazolium-based ionic liquids. *Fluid Phase Equilibria*, 320:1–10, 2012.

[219] K. Fumino, A. Wulf, and R. Ludwig. Strong, localized, and directional hydrogen bonds fluidize ionic liquids. *Angewandte Chemie - International Edition*, 47(45):8731–8734, 2008.

[220] K. Fumino, A. Wulf, and R. Ludwig. The cation-anion interaction in ionic liquids probed by far-infrared spectroscopy. *Angewandte Chemie - International Edition*, 47(20):3830–3834, 2008.

[221] K. Fumino, A. Wulf, and R. Ludwig. Hydrogen Bonding in Protic Ionic Liquids: Reminiscent of Water. *Angewandte Chemie International Edition*, 48(17):3184–3186, 2009.

[222] K. Fumino, A. Wulf, and R. Ludwig. The potential role of hydrogen bonding in aprotic and protic ionic liquids. *Physical Chemistry Chemical Physics*, 11(39):8790–8794, 2009.

[223] K. Fumino, K. Wittler, and R. Ludwig. The anion dependence of the interaction strength between ions in imidazolium-based ionic liquids probed by far-infrared spectroscopy. *Journal of Physical Chemistry B*, 116(31):9507–9511, 2012.

[224] K. Fumino, S. Reimann, and R. Ludwig. Probing molecular interaction in ionic liquids by low frequency spectroscopy: Coulomb energy, hydrogen bonding and dispersion forces. *Physical Chemistry Chemical Physics*, 16(40):21903–21929, 2014.

[225] K. Fumino, V. Fossog, P. Stange, D. Paschek, R. Hempelmann, and R. Ludwig. Controlling the subtle energy balance in protic ionic liquids: Dispersion forces compete with hydrogen bonds. *Angewandte Chemie - International Edition*, 54(9):2792–2795, 2015.

[226] A. Wulf, K. Fumino, and R. Ludwig. Spectroscopic evidence for an enhanced anion-cation interaction from hydrogen bonding in

pure imidazolium ionic liquids. *Angewandte Chemie - International Edition*, 49(2):449–453, 2010.

[227] K. Noack, P. S. Schulz, N. Paape, J. Kiefer, P. Wasserscheid, and A. Leipertz. The role of the C_2 position in interionic interactions of imidazolium based ionic liquids: A vibrational and NMR spectroscopic study. *Physical Chemistry Chemical Physics*, 12(42):14153–14161, 2010.

[228] A. Elbourne, K. Voïtchovsky, G. G. Warr, and R. Atkin. Ion structure controls ionic liquid near-surface and interfacial nanostructure. *Chemical Science*, 6(1):527–536, 2015.

[229] P. A. Hunt. Why does a reduction in hydrogen bonding lead to an increase in viscosity for the 1-Butyl-2,3-dimethylimidazolium-based ionic liquids? *Journal of Physical Chemistry B*, 111(18):4844–4853, 2007.

[230] H. Chen, X. Chen, J. Deng, and J. Zheng. Isotropic ordering of ions in ionic liquids on the sub-nanometer scale. *Chemical Science*, 9(6):1464–1472, 2018.

[231] N. J. Brooks, F. Castiglione, C. M. Doherty, A. Dolan, A. J. Hill, P. A. Hunt, R. P. Matthews, M. Mauri, A. Mele, R. Simonutti, I. J. Villar-Garcia, C. C. Weber, and T. Welton. Linking the structures, free volumes, and properties of ionic liquid mixtures. *Chemical Science*, 8(9):6359–6374, 2017.

[232] M. A. Gebbie, A. M. Smith, H. A. Dobbs, A. A. Lee, G. G. Warr, X. Banquy, M. Valtiner, M. W. Rutland, J. N. Israelachvili, S. Perkin, and R. Atkin. Long range electrostatic forces in ionic liquids. *Chemical Communications*, 53(7):1214–1224, 2017.

[233] T. Köddermann, C. Wertz, A. Heintz, and R. Ludwig. Ion-pair formation in the ionic liquid 1-ethyl-3-methylimidazolium bis(triflyl)imide as a function of temperature and concentration. *ChemPhysChem*, 7(9):1944–1949, 2006.

[234] S. Zahn, G. Bruns, J. Thar, and B. Kirchner. What keeps ionic liquids in flow? *Physical Chemistry Chemical Physics*, 10(46):6921–6924, 2008.

[235] W. C. Xu, S. Sun, and S. Wu. Photoinduced Reversible Solid-to-Liquid Transitions for Photoswitchable Materials. *Angewandte Chemie - International Edition*, 58(29):9712–9740, 2019.

[236] O. Tsutsumi, A. Kanazawa, T. Shiono, T. Ikeda, and L. S. Park. Photoinduced phase transition of nematic liquid crystals with donor- acceptor azobenzenes: Mechanism of the thermal recovery of the nematic phase. *Physical Chemistry Chemical Physics*, 1(18):4219–4224, 1999.

[237] J. Guan, M. Zhang, B. Li, H. Yang, and G. Wang. Photocontrolled phase transitions and reflection behaviors of smectic liquid crystals by a chiral azobenzene. *ChemPhysChem*, 13(17):3812–3818, 2012.

[238] R. H. Zha, G. Vantomme, J. A. Berrocal, R. Gosens, B. De Waal, S. Meskers, and E. W. Meijer. Photoswitchable nanomaterials based on hierarchically organized siloxane oligomers. *Advanced Functional Materials*, 28(1):1703952, 2018.

[239] C. Wang, K. Hashimoto, R. Tamate, H. Kokubo, K. Morishima, X. Li, M. Shibayama, F. Lu, T. Nakanishi, and M. Watanabe. Viscoelastic change of block copolymer ion gels in a photoswitchable azobenzene ionic liquid triggered by light. *Chemical Communications*, 55(12):1710–1713, 2019.

[240] Z. Li, X. Yuan, Y. Feng, Y. Chen, Y. Zhao, H. Wang, Q. Xu, and J. Wang. A reversible conductivity modulation of azobenzene-based ionic liquids in aqueous solutions using UV/vis light. *Physical Chemistry Chemical Physics*, 20(18):12808–12816, 2018.

[241] Y. Norikane, Y. Hirai, and M. Yoshida. Photoinduced isothermal phase transitions of liquid-crystalline macrocyclic azobenzenes. *Chemical Communications*, 47(6):1770–1772, 2011.

[242] W. Baek, J. M. Heo, S. Oh, S. H. Lee, J. Kim, J. F. Joung, S. Park, H. Chung, and J. M. Kim. Photoinduced reversible phase transition of azobenzene-containing polydiacetylene crystals. *Chemical Communications*, 52(97):14059–14062, 2016.

[243] C. Wang, K. Hashimoto, R. Tamate, H. Kokubo, and M. Watanabe. Controlled Sol–Gel Transitions of a Thermoresponsive Polymer in a Photoswitchable Azobenzene Ionic Liquid as a Molecular Trigger. *Angewandte Chemie - International Edition*, 57(1):227–230, 2018.

[244] H. Zhou, C. Xue, P. Weis, Y. Suzuki, S. Huang, K. Koynov, G. K. Auernhammer, R. Berger, H. J. Butt, and S. Wu. Photoswitching of glass transition temperatures of azobenzene-containing polymers induces reversible solid-to-liquid transitions. *Nature Chemistry*, 9(2):145–151, 2017.

[245] Y. Norikane, E. Uchida, S. Tanaka, K. Fujiwara, H. Nagai, and H. Akiyama. Photoinduced phase transitions in rod-shaped azobenzene with different alkyl chain length. *Journal of Photopolymer Science and Technology*, 29(1):145–148, 2016.

[246] J. Vapaavuori, A. Laventure, C. G. Bazuin, O. Lebel, and C. Pellerin. Submolecular Plasticization Induced by Photons in Azobenzene Materials. *Journal of the American Chemical Society*, 137(42):13510–13517, 2015.

[247] C. Wang, X. Ma, Y. Kitazawa, Y. Kobayashi, S. Zhang, H. Kokubo, and M. Watanabe. From Macromolecular to Small-Molecular Triggers: Facile Method toward Photoinduced LCST Phase Behavior of Thermoresponsive Polymers in Mixed Ionic Liquids Containing an Azobenzene Moiety. *Macromolecular Rapid Communications*, 37(23):1960–1965, 2016.

[248] Y. Norikane, E. Uchida, S. Tanaka, K. Fujiwara, E. Koyama, R. Azumi, H. Akiyama, H. Kihara, and M. Yoshida. Photoinduced crystal-to-liquid phase transitions of azobenzene derivatives and their application in photolithography processes through a solid-liquid patterning. *Organic Letters*, 16(19):5012–5015, 2014.

[249] A. Wulf, K. Fumino, D. Michalik, and R. Ludwig. IR and NMR properties of ionic liquids: Do they tell us the same thing? *ChemPhysChem*, 8(15):2265–2269, 2007.

[250] Koichi Fumino, Verlaine Fossog, Kai Wittler, Rolf Hempelmann, and Ralf Ludwig. Dissecting anion-cation interaction energies in protic ionic liquids. *Angewandte Chemie - International Edition*, 52(8):2368–2372, 2013.

[251] J. C. Lassègues, J. Grondin, D. Cavagnat, and P. Johansson. New interpretation of the CH stretching vibrations in imidazolium-based ionic liquids. *Journal of Physical Chemistry A*, 113(23):6419–6421, 2009.

[252] M. V. Pavan, A. Raja, and R. Barron. *Wide angle X-ray Diffraction Studies of Liquid Crystals*. LibreTexts, 2009.

[253] T. Niemann, D. Zaitsau, A. Strate, A. Villinger, and R. Ludwig. Cationic clustering influences the phase behaviour of ionic liquids. *Scientific Reports*, 8(1):14753, 2018.

[254] A. E. Khudozhitkov, J. Neumann, T. Niemann, D. Zaitsau, P. Stange, D. Paschek, A. G. Stepanov, D. I. Kolokolov, and R. Ludwig. Hydrogen Bonding Between Ions of Like Charge in Ionic Liquids Characterized by NMR Deuteron Quadrupole Coupling Constants—Comparison with Salt Bridges and Molecular Systems, 2019.

[255] K. Binnemans. Ionic Liquid Crystals. *Chemical Reviews*, 105(11):4148–4204, 2005.

[256] K. Goossens, K. Lava, C. W. Bielawski, and K. Binnemans. Ionic Liquid Crystals: Versatile Materials, 2016.

[257] S. G. Kazarian, B. J. Briscoe, and T. Welton. Combining ionic liquids and supercritical fluids: In situ ATR-IR study of CO_2 dissolved in two ionic liquids at high pressures. *Chemical Communications*, (20):2047–2048, 2000.

[258] K. A. Fletcher and S. Pandey. Effect of water on the solvatochromic probe behavior within room-temperature ionic liquid 1-butyl-3-methylimidazolium hexafluorophosphate. *Applied Spectroscopy*, 56(2):266–271, 2002.

[259] S. N. V. K. Aki, J. F. Brennecke, and A. Samanta. How polar are room-temperature ionic liquids? *Chemical Communications*, (5):413–414, 2001.

[260] T. Welton. Room-Temperature Ionic Liquids. Solvents for Synthesis and Catalysis. *Chemical Reviews*, 99(8):2071–2083, 1999.

[261] A. E. Visser, R. P. Swatloski, and R. D. Rogers. pH-dependent partitioning in room temperature ionic liquids: Provides a link to traditional solvent extraction behavior. *Green Chemistry*, 2(1):1–4, 2000.

[262] A. Mele, C. D. Tran, and S. H. De Paoli Lacerda. The structure of a room-temperature ionic liquid with and without trace amounts of water: The role of C-H· · ·O and C-H· · ·F interactions in 1-n-butyl-3-methylimidazolium tetrafluoroborate. *Angewandte Chemie - International Edition*, 42(36):4364–4366, 2003.

[263] Z. Liu, S. Z. El Abedin, and F. Endres. Raman and FTIR spectroscopic studies of 1-Ethyl-3-methylimidazolium trifluoromethylsulfonate, its mixtures with water and the solvation of Zinc ions. *ChemPhysChem*, 16(5):970–977, 2015.

[264] Asahi Spectra. *MAX-303 Xenon Light Source 300 W. Technical Information*.

List of publications

Sub-μL measurements of the thermal conductivity and heat capacity of liquids			
Authors	Carlos López-Bueno[1], David Bugallo[1], Víctor Leborán[1] y Francisco Rivadulla[1]		
Affiliations	[1] CIQUS. Universidade de Santiago de Compostela.		
Journal	Physical Chemistry Chemical Physics	Impact Factor: 3.676 (Q1)	
Publisher	The Royal Society of Chemistry's	ISSN: 1463-9076	
Citation	Phys. Chem. Chem. Phys., 2018, 20, 7277-7281	**Year**	2018
Chapter	The content of this article was partially reproduced in Chapter 2.		
Permissions	As an author of this article, no further permission by the RSC is required.		
Contribution	All the measurements, analysis and simulations. Writing the manuscript.		

Low tempreature glass/crystal transition in ionic liquids determined by H-bond vs. coulombic strength			
Authors	Carlos López-Bueno[1], Marius R. Bittermann[2], Bruno Dacuña-Mariño[3], Antonio Luis Llamas-Saiz[3], María del Carmen Giménez-López[1], Sander Woutersen[2] and Francisco Rivadulla[1]		
Affiliations	[1] CIQUS. Universidade de Santiago de Compostela. [2] Van't Hoff Institute for Molecular Sciences. University of Amsterdam [3] X-Ray Unit, RIAIDT. Universidade de Santiago de Compostela		
Journal	Physical Chemistry Chemical Physics	Impact Factor: 3.676 (Q1)	
Publisher	The Royal Society of Chemistry's	ISSN: 1463-9076	
Citation	Phys. Chem. Chem. Phys., 2020, 22, 20524-20530	**Year**	2020
Chapter	The content of this article was reproduced in Chapter 6.		
Permissions	As an author of this article, no further permission by the RSC is required.		
Contribution	All the measurements and analysis, except X-Ray diffraction and some DSC experiments. Writing the manuscript.		

Hydrophobic solvation increases thermal conductivity of water			
Authors	Carlos López-Bueno[1], Manuel Suárez-Rodríguez[1], Alfredo Amigo [2] and Francisco Rivadulla[1]		
Affiliations	[1] CIQUS. Universidade de Santiago de Compostela. [2] Departamento de Física Aplicada. Universidade de Santiago de Compostela.		
Journal	Physical Chemistry Chemical Physics (Hot Article)	Impact Factor: 3.676 (Q1)	
Publisher	The Royal Society of Chemistry's	ISSN: 1463-9076	
Citation	Phys. Chem. Chem. Phys., 2020, 22, 21094-21098	**Year**	2020
Chapter	The content of this article was reproduced in Chapter 4.		
Permissions	As an author of this article, no further permission by the RSC is required.		
Contribution	All the measurements and analysis, except κ of 1,2-propanol. Writing the manuscript.		

A New Type of Supramolecular Fluid Based on H_2O-Alkylammonium/Phosphonium Solutions			
Authors	Carlos López-Bueno[1], Carlos Herreros-Lucas[1], Manuel Suárez-Rodríguez[1], Marius R. Bittermann[2], Alfredo Amigo [3], Sander Woutersen[2], María del Carmen Giménez-López[1] and Francisco Rivadulla[1]		
Affiliations	[1] CIQUS. Universidade de Santiago de Compostela. [2] Van't Hoff Institute for Molecular Sciences. University of Amsterdam [3] Departamento de Física Aplicada. Universidade de Santiago de Compostela.		
Journal	Angewandte Chemie (Cover Picture)	Impact Factor: 15.336 (Q1, D1)	
Publisher	Wiley-VCH GmbH	ISSN: 1521-3773	
Citation	Angew. Chem. 2021, 133, 7618-7624	**Year**	2021
Chapter	The content of this article was reproduced in Chapter 5.		
Permissions	Reproduced with permission of Wiley-VCH GmbH (see Rights and Permissions chapter).		
Contribution	All the measurements and analysis, except NMR, κ and DSC of TtBPBr, some cryo-IR experiments and the electrochemical measurements. Writing the manuscript.		

Rights and permissions

This Agreement between CIQUS, Universidad de Santiago de Compostela -- Carlos López-Bueno ("You") and John Wiley and Sons ("John Wiley and Sons") consists of your license details and the terms and conditions provided by John Wiley and Sons and Copyright Clearance Center.

License Number	5072980070147
License date	May 20, 2021
Licensed Content Publisher	John Wiley and Sons
Licensed Content Publication	Angewandte Chemie International Edition
Licensed Content Title	Strong, Localized, and Directional Hydrogen Bonds Fluidize Ionic Liquids
Licensed Content Author	Koichi Fumino, Alexander Wulf, Ralf Ludwig
Licensed Content Date	Oct 21, 2008
Licensed Content Volume	47
Licensed Content Issue	45
Licensed Content Pages	4
Type of Use	Dissertation/Thesis
Requestor type	University/Academic
Format	Print and electronic
Portion	Figure/table
Number of figures/tables	2
Will you be translating?	No
Title	Study and Control of Thermal Transport in Complex Fluids
Institution name	Universidad de Santiago de Compostela
Expected presentation date	Nov 2021

This Agreement between CIQUS, Universidad de Santiago de Compostela -- Carlos López-Bueno ("You") and AIP Publishing ("AIP Publishing") consists of your license details and the terms and conditions provided by AIP Publishing and Copyright Clearance Center.

License Number	5042440253996
License date	Apr 05, 2021
Licensed Content Publisher	AIP Publishing
Licensed Content Publication	Journal of Chemical Physics
Licensed Content Title	Thermal conductivity of normal and deuterated water, crystalline ice, and amorphous ices
Licensed Content Author	Ove Andersson
Licensed Content Date	Sep 28, 2018
Licensed Content Volume	149
Licensed Content Issue	12
Type of Use	Thesis/Dissertation
Requestor type	University or Educational Institution
Format	Print and electronic
Portion	Figure/Table
Number of figures/tables	1
Title	Study and Control of Thermal Transport in Complex Fluids
Institution name	Universidad de Santiago de Compostela
Expected presentation date	Nov 2021
Portions	Data of Figure 4

This Agreement between CIQUS, Universidad de Santiago de Compostela -- Carlos López-Bueno ("You") and AIP Publishing ("AIP Publishing") consists of your license details and the terms and conditions provided by AIP Publishing and Copyright Clearance Center.

License Number	5042351098747
License date	Apr 05, 2021
Licensed Content Publisher	AIP Publishing
Licensed Content Publication	Journal of Chemical Physics
Licensed Content Title	Crucial role of fragmented and isolated defects in persistent relaxation of deeply supercooled water
Licensed Content Author	Shinji Saito, Biman Bagchi, Iwao Ohmine
Licensed Content Date	Sep 28, 2018
Licensed Content Volume	149
Licensed Content Issue	12
Type of Use	Thesis/Dissertation
Requestor type	University or Educational Institution
Format	Print and electronic
Portion	Figure/Table
Number of figures/tables	1
Title	Study and Control of Thermal Transport in Complex Fluids
Institution name	Universidad de Santiago de Compostela
Expected presentation date	Nov 2021
Portions	Some graphs of Figure S2

This Agreement between CIQUS, Universidad de Santiago de Compostela -- Carlos López-Bueno ("You") and Springer Nature ("Springer Nature") consists of your license details and the terms and conditions provided by Springer Nature and Copyright Clearance Center.

License Number	5034091227805
License date	Mar 22, 2021
Licensed Content Publisher	Springer Nature
Licensed Content Publication	Journal of Solution Chemistry
Licensed Content Title	Thermal Conductivity of Aqueous K2CO3 Solutions at High Temperatures
Licensed Content Author	Lala A. Akhmedova-Azizova et al
Licensed Content Date	Jun 12, 2009
Type of Use	Thesis/Dissertation
Requestor type	academic/university or research institute
Format	print and electronic
Portion	figures/tables/illustrations
Number of figures/tables/illustrations	1
Will you be translating?	no
Circulation/distribution	1 - 29
Author of this Springer Nature content	no
Title	Study and Control of Thermal Transport in Complex Fluids
Institution name	Universidad de Santiago de Compostela
Expected presentation date	Nov 2021
Portions	Figure 2

This Agreement between CIQUS, Universidad de Santiago de Compostela -- Carlos López-Bueno ("You") and Springer Nature ("Springer Nature") consists of your license details and the terms and conditions provided by Springer Nature and Copyright Clearance Center.

License Number	5034091145390
License date	Mar 22, 2021
Licensed Content Publisher	Springer Nature
Licensed Content Publication	Journal of Solution Chemistry
Licensed Content Title	Thermal Conductivity of Aqueous KI and KBr Solutions at High Temperatures and High Pressures
Licensed Content Author	Ilmutdin M. Abdulagatov et al
Licensed Content Date	Jan 1, 2001
Type of Use	Thesis/Dissertation
Requestor type	academic/university or research institute
Format	print and electronic
Portion	figures/tables/illustrations
Number of figures/tables/illustrations	1
Will you be translating?	no
Circulation/distribution	1 - 29
Author of this Springer Nature content	no
Title	Study and Control of Thermal Transport in Complex Fluids
Institution name	Universidad de Santiago de Compostela
Expected presentation date	Nov 2021
Portions	Figure 2

This Agreement between CIQUS, Universidad de Santiago de Compostela -- Carlos López-Bueno ("You") and AIP Publishing ("AIP Publishing") consists of your license details and the terms and conditions provided by AIP Publishing and Copyright Clearance Center.

License Number	5025860682290
License date	Mar 11, 2021
Licensed Content Publisher	AIP Publishing
Licensed Content Publication	Journal of Chemical Physics
Licensed Content Title	Hydrophobic hydration and the anomalous partial molar volumes in ethanol-water mixtures
Licensed Content Author	Ming-Liang Tan, Benjamin T. Miller, Jerez Te, et al
Licensed Content Date	Feb 14, 2015
Licensed Content Volume	142
Licensed Content Issue	6
Type of Use	Thesis/Dissertation
Requestor type	University or Educational Institution
Format	Print and electronic
Portion	Figure/Table
Number of figures/tables	1
Title	Study and Control of Thermal Transport in Complex Fluids
Institution name	Universidad de Santiago de Compostela
Expected presentation date	Nov 2021
Portions	Figure 3

This Agreement between CIQUS, Universidad de Santiago de Compostela -- Carlos López-Bueno ("You") and AIP Publishing ("AIP Publishing") consists of your license details and the terms and conditions provided by AIP Publishing and Copyright Clearance Center.

License Number	5005250210114
License date	Feb 10, 2021
Licensed Content Publisher	AIP Publishing
Licensed Content Publication	Journal of Chemical Physics
Licensed Content Title	Hydrophobic hydration and the anomalous partial molar volumes in ethanol-water mixtures
Licensed Content Author	Ming-Liang Tan, Benjamin T. Miller, Jerez Te, et al
Licensed Content Date	Feb 14, 2015
Licensed Content Volume	142
Licensed Content Issue	6
Type of Use	Thesis/Dissertation
Requestor type	University or Educational Institution
Format	Print and electronic
Portion	Figure/Table
Number of figures/tables	1
Title	Study and Control of Thermal Transport in Complex Fluids
Institution name	Universidad de Santiago de Compostela
Expected presentation date	Nov 2021
Portions	Figure 1

This Agreement between CIQUS, Universidad de Santiago de Compostela -- Carlos López-Bueno ("You") and Elsevier ("Elsevier") consists of your license details and the terms and conditions provided by Elsevier and Copyright Clearance Center.

License Number	4992941130804
License date	Jan 20, 2021
Licensed Content Publisher	Elsevier
Licensed Content Publication	The Journal of Chemical Thermodynamics
Licensed Content Title	Advanced calibration, adjustment, and operation of a density and sound speed analyzer
Licensed Content Author	Tara J. Fortin,Arno Laesecke,Malte Freund,Stephanie Outcalt
Licensed Content Date	Feb 1, 2013
Licensed Content Volume	57
Licensed Content Issue	n/a
Licensed Content Pages	10
Start Page	276
End Page	285
Type of Use	reuse in a thesis/dissertation
Portion	figures/tables/illustrations
Number of figures/tables/illustrations	1
Format	both print and electronic
Are you the author of this Elsevier article?	No
Will you be translating?	No
Title	Study and Control of Thermal Transport in Complex Fluids
Institution name	Universidad de Santiago de Compostela
Expected presentation date	Nov 2021
Portions	Figure 1